UNIVERSITAT DE VALÈNCIA

Departament de Física Atòmica, Molecular i Nuclear
Institut de Física Corpuscular
Doctorat en Física

Calibration and background model of the NEW detector at the LSC

PhD thesis

Author:
Miquel Nebot Guinot

Supervisors:
Prof. J.J. Gómez Cadenas
Dr. J. Martín-Albo Simón

2017

Work carried out at *Instituto de Física Corpuscular* (IFIC) and *Laboratorio Subterráneo de Canfranc* (LSC).

Vale más fracasar por intentar un triunfo,
que dejar de triunfar por temor a una fracaso.
A ti, por hacerme creer que es posible

"If I have seen further it is by standing on the shoulders of Giants."

Isaac Newton

Agraïments

Els gegants no hi són només a les fàbules també hi són a la vida real però, més que per l'alçada, la força o la por, és per l'amplada del passos que fan. Igual que Tombatossals, m'han precedit moltes persones que m'han obert el camí, "abriendo huella", deixant grans empremtes per a que jo poguera xafar un poc més segur.

Primer de tot agrair als meus directors **Juanjo** i **Justo** que, casualitats o no, van ser les primeres persones que vaig conèixer a l'hora de buscar un grup d'investigació i, a la fi, els meus directors. Les inquietuds d'ú no acaben si hi ha algú que encara en té més. A Juanjo li estaré sempre agraït per la possibilitat de fer-me partícip en una de les seues inquietuds, en aquest encabotament per desvetlar les coses que intriguen a la humanitat o almenys una de tantes. La seua creença, entusiasme i èpica és contagiosa. A Justo vull agrair-li la seua accessibilitat i paciència, seguir els seus raonaments no sempre era trivial. També la seua sinceritat a l'hora d'aconsellar amb un: "¿Tú qué quieres hacer?" o emprar la seua lupa i bolígraf roig corrector. La major part de les coses que he après ho he fet d'ell i espere, en algun moment, poder seguir fent-ho. Moltes gràcies per tot.

En segon lloc vull agrair l'ajuda de **Javi M.** i **Andrew**, especialment en els últims temps, per la seua comprensió, suport i discussions sobre l'anàlisi dels capítols centrals d'aquest treball.

La part més qualitativa d'aquest treball no haguera sigut possible sense l'objectiu del mateix "el detector NEW" i això li ho dec als enginyers/hardware. Un treball de dedicació a consciència, hores i precisió, per construir "una máquina de hacer tesis": **Marc**, **Curro**, **Francesc**, **Raúl**, **Jordi**, **Jose Vicente**, **James**... en especial, pel

tracte personal, a aquells que al meu inici em van tirar moltes mans quan es tractava de fer instal·lacions de hardware i electrònica: **Vicente**, **Sara**, **Javi**, **Alberto**, **Manolo** i, principalment, a **Igor**, que en els primers anys em va enganxar a l'experimentalisme.

La millor època, sens dubte, li la dec al pàdel team (**Luis**, **David** i **Toni**) i al beer extended team (**Miguel**, **Nacho**, Andrew i Justo) perquè les risses fan molt més fàcil el treball i dels qui he aprés molt.

També per les èpoques passades fora de l'IFIC vull enrecordar-me del meu company de shifts **Josh**, així com dels meus companys de neutrino schools **Ander** i **Gonzalo**. A més d'alguns ja mencionats, a l'hora de fer física sempre són d'agrair les opinions i el consells de **Michel**, **Paola**, **Pau**, **Anselmo**... i **Neus** no només de física. A la segona generació del 109 per compartir el soroll infernal sense tornar-nos bojos (**Josemaría**, **Japepe**, **Ryan**, **Alex** i **Carmen**). I com no a **Jose** per tots els papers, sense ell només hi seria el caos. Agrair també a totes les persones de NEXT que d'una manera o altra han contribuït a aquest projecte col·laboratiu.

Qui em diria quan un estiu vaig llegir amb admiració i bocabadat al diari alguna cosa d'un problema amb el model solar, unes partícules que allí es generaven i la implicació de la UV en un detector que pareixia de fantasia amb milers d'ulls mirant a l'aigua, que acabaria fent un estudi precisament d'aquelles partícules. En aquest camí també m'han acompanyat el meu "germà" experimental **Vicent** amb les penes i les "chapuces", així com els 3000s compartits amb **Carlos**.

Una personeta inquieta que intenta desxifrar què hi ha darrere del funcionament d'una ràdio o de la combustió d'un misto és un potencial científic que tractarà de revelar tot allò que no entén i, si no li ho poden explicar, buscarà explicació per si mateix. Sense uns pares que fomentaren aquells descobriments per mitjà d'experimentar, o almenys permetien que de tant en tant trencara alguna cosa encara que després hagueren d'arreglar-la, jo no estaria ací. Tampoc sense una germana que obrira camí a la ciència i en qui poguera veure'm reflectit quan em mirara a l'espill, que alçara un poc més la marca de mesurar l'alçada a la paret i, per tant, em fera esforçar-me per a arribar, com a mínim, al mateix lloc. D'altra banda el contrapés d'una responsabilitat, altra germana que també hem feia esforçar-me per tal de cultivar la paciència

i entendre que fins que no saps explicar les coses no les entens de veres. A vosaltres, gràcies!

Però, si hi ha una persona responsable d'aquesta fita, eixa és **Clara** com a "*doctoranda consorte*". Sense la "*constante*" pregunta de: "I per què no? Per què tú no?" o el seu recolzament, no hi estaria on estic, no haguera arribat on he arribat i, molt possiblement, hagués baixat els braços o pres una altra direcció en qualsevol dels encreuaments per on he passat.

"Perquè hi haurà un dia que no podrem més
i llavors ho podrem tot."

Vicent Andrés Estellés

"... sera infantil, pero
cuando realizamos sueños,
todos somos niños."

"La voz del hielo"
Simone Moro

Resumen

El Modelo Estándar de la física de partículas describe los constituyentes fundamentales de la materia y su comportamiento. Desarrollado en los años 70, ha servido para explicar el auge de los descubrimientos de nuevas partículas a principios del s. XX así como para predecir otras. Su validez ha sido probada y es aceptada por toda la comunidad científica. Sin embargo, el descubrimiento de la masa del neutrino evidencia que ésta no es la teoría última y por tanto que hay física mas allá del Modelo Estándar.

Al igual que ocurrió con el propio neutrino (la particula elemental más pequeña) en el momento de su propuesta para explicar la energía aparentemente no conservada en las desintegraciones beta (Pauli,1930) y su posterior descubrimiento (Cowan–Reines, 1956); el descubrimiento de la masa del neutrino también vino asociado a la desaparición, en este caso, de un tercio de los neutrino previstos. En la medida del flujo de neutrinos provenientes del Sol se observaba un déficit respecto a los cálculos teóricos y su posible explicación era que éstos pudieran oscilar, es decir cambiar de un estado a otro, siendo para ello necesario que los neutrinos fueran masivos. La oscillación de neutrinos ha sido probada por diferentes experimentos y diferentes canales. Actualmente el valor preciso de la masa de los neutrinos sigue sin conocerse puesto que de los experimentos de oscilaciones sólo pueden extraerse resultados de diferencias cuadráticas de las masas. No obstante se sabe que son muy ligeros ($\sim$50 meV el más ligero) comparados con las demás partículas elementales. Su elusividad y su ligereza, en otras palabras su comportamiento, esta siendo hoy en día uno de los campos mas estudiados de la física. Falta por entender cómo adquieren masa estas partículas y una de las hipótesis que da respuesta a la vez a su ligereza

es que fueran su propia antipartícula (fermiones de Majorana). Esto además, permitiría procesos en los que se viola la conservación del numero leptónico y así dar una explicación a la asimetría bariónica observada en el universo. Si el neutrino es su propia antipartícula podría haber inclinado la balanza en equilibrio materia–antimateria a favor de la primera durante los primeros instantes del universo. Así con su carácter de apariciones y desapariciones, al que parece estar ligado, el neutrino podría haber dado lugar al universo visible actual.

Diferentes lineas experimentales estudian hoy en día el neutrino y sus características, sin embargo la mejor linea para poder determinar si el neutrino es Majorana es a través de la desintegración doble beta sin neutrinos. La desintegración doble beta es un proceso nuclear de segundo orden de los denominados raros, que ocurre entre dos núcleos pares entre los cuales está energéticamente prohibida la desintegración beta. Este proceso implica un cambio en la carga Z de dos unidades. Podría ocurrir en dos formas: con la emisión de neutrinos ($\beta\beta 2\nu$) o sin ella ($\beta\beta 0\nu$). La desintegración doble beta sin neutrinos, es una transición radiactiva hipotética en la que dos neutrones se desintegran en dos protones mediante el intercambio de un neutrino, emitiendo dos electrones. Este proceso solo es posible si el neutrino es su propia antipartícula, es decir, una partícula de Majorana. Si se observara la desintegración doble beta sin neutrinos, además de confirmar la naturaleza Majorana de éstos, se podría derivar la masa efectiva del neutrino al medir la vida media de este proceso

$$(T_{1/2}^{\beta\beta 0\nu})^{-1} = G^{0\nu}|M_{0\nu}|^2(\frac{\langle m_{\beta\beta}\rangle}{m_e})^2 \tag{1}$$

y así también establecer su jerarquía absoluta. En esta equación, $G^{0\nu}$ es una integral de espacio de fases, $M_{0\nu}$ es el elemento de matriz nuclear del proceso, m_e es la masa del electrón y $m_{\beta\beta}$ es la llamada masa efectiva Majorana del neutrino. Así pues, el descubrimiento de este proceso permitiría explicar la pequeña masa de los neutrinos con respecto al resto de fermiones e implicaría la violación del número leptónico en dos unidades, lo que puede ser un ingrediente para la leptogénesis primordial, explicando la asimetría entre materia y antimateria en el Universo. La respuesta a estas incógnitas y sus implicaciones a través de la observación de un único proceso, hacen de la búsqueda de las

desintegraciones doble beta sin neutrinos un campo muy activo.

Solo se conocen unos pocos isótopos que pueden decaer mediante la transición $\beta\beta 2\nu$ permitida en el modelo estándar y por tanto candidatos para búsquedas del proceso $\beta\beta 0\nu$. Además de los diferentes isótopos, también existen diferentes técnicas experimentales para poder medir este proceso. Los detectores empleados para buscar la desintegración doble beta miden, en general, la energía cinética de los electrones emitidos en el proceso. La suma de estas energías sería, en una desintegración doble beta sin neutrinos, igual al valor $Q_{\beta\beta}$ del proceso. Un detector ideal podría medir estos eventos monocromáticos, pero en la práctica, la resolución energética finita de cualquier detector distribuiría la energía reconstruida en una gaussiana centrada en $Q_{\beta\beta}$. Cualquier otro proceso que deposite energía en esa región del espectro dentro del detector, incluido el propio proceso $\beta\beta 2\nu$, puede dificultar la medida y es catalogado como ruido de fondo. Por ello, una resolución energética capaz de discernir señal y ruido es un parámetro fundamental para todos los experimentos. Aun así, no es suficiente por sí sola y cualquier ayuda extra para reducir o identificar los ruidos de fondo son necesarias. La mayoría de experimentos utilizan esas identificaciones adicionales explotando sus técnicas de detección: doble detección, etiquetado, patrones 3D... Respecto a la reducción de los ruidos de fondo, todos los experimentos diseñan y eligen con cuidado los materiales para su detectores, puesto que la principal fuente de ruido proviene de la radiactividad natural de las impurezas presentes en todos los materiales (^{232}Th y ^{238}U principalmente). Una caracterización y selección de los posibles materiales es esencial. Además, los ruidos de fondo pueden ser generados por rayos cósmicos y por tanto su atenuación operando el detector en instalaciones subterráneas es también necesaria.

Cuando se pretende observar este proceso tan raro, la optimización de todos los parámetros es necesaria y puede dar lugar a diferentes aproximaciones. Su relación suele describirse como

$$T_{1/2} \propto a \cdot \epsilon \sqrt{\frac{M \cdot t}{\Delta E \cdot B}} \tag{2}$$

donde ϵ es la eficiencia de detección, el producto de la cantidad de isótopo $\beta\beta$ utilizado (M) por el tiempo de medida (t) es la exposición, ΔE es la resolución energética y B la tasa de ruido de fondo.

La optimización simultánea de todos estos parámetros no es, en general, posible; consecuentemente, se han propuesto técnicas experimentales muy variadas para buscar la desintegración. Actualmente las técnicas experimentales que lideran la búsqueda son: los detectores de germanio, los detectores de centelleo, los bolometros y las cámaras de proyección temporal (TPC). La generación actual (experimentos del orden de 100 kg de masa de isótopo emisor) no ha encontrado ninguna evidencia del proceso $\beta\beta0\nu$, llegando a establecer un límite inferior a la vida media del proceso de 10^{26} años, lo que implica una masa efectiva menor que 0.24 eV. Esto demuestra un gran reto experimental y la posible necesidad de saltar a escalas más grandes (del orden de la tonelada) para, al menos, barrer la banda de masas de la jerarquía inversa del neutrino.

Entre las propuestas actuales, aquellas basadas en una TPC gaseosa tienen la ventaja de obtener la reconstrucción espacial de la traza dejada por la partícula usando detectores de pixeles, como es el caso de NEXT. El experimento NEXT (Neutrino Experiment with a Xe TPC) tiene como objetivo la detección del modo $\beta\beta0\nu$ usando 100 kg del isotópo ^{136}Xe en una TPC gaseosa a alta presión (15 bar). El principio de NEXT está basado en dos planos de detección separados y optimizados: uno para medir la energía y otro para reconstruir la trayectoria. El gas xenón como emisor y como medio detector ofrece un diseño compacto a la vez que sus propiedades como detector de radiación, con dos señales primarias, permiten marcar el inicio del evento (centelleo) para su recostrucción espacial y medir su energía y trayectroria (ionización). Para amplificar la señal de ionización se utiliza la electroluminiscencia del xenón proporcionando una excelente resolución energética $< 0.5\%$ FWHM en $Q_{\beta\beta}$. La capacidad extra de reconstruir la traza topológica característica de un evento $\beta\beta$ permite eliminar la mayor parte del ruido de fondo del experimento. Con todo ello, la tasa de ruido esperada para NEXT–100 es 4×10^{-4} cuentas/ (keV ·kg ·año). Esto permitiría llegar a una sensibilidad de $\mathrm{T}^{\beta\beta0\nu}_{1/2}(^{136}\mathrm{Xe}) \simeq 6 \times 10^{25}$ años en tres años efectivos.

Las capacidades técnicas de buena resolución energética y topología de la propuesta tecnológica de NEXT fueron demostradas con los prototipos NEXT–DEMO y NEXT–DBDM. Ahora su escalabilidad y la revisión de las previsiones de ruido basadas en simulaciones es el

objetivo a demostrar con la puesta en marcha del detector radiopuro NEXT–NEW en el Laboratorio Subterráneo de Canfranc. Además este detector permitirá reconstruir trazas más largas y demostrar una buena resolución energética en un detector grande, así como posiblemente medir el modo de desintegración con neutrinos ($\beta\beta 2\nu$). El objetivo principal es identificar los ruidos de fondo tanto del laboratorio como de los materiales con los que se ha construido el detector.

El detector NEW es una cámara de proyección temporal a escala 1:2 del detector NEXT–100. Esta compuesto de una jaula eléctrica cilíndrica que proporciona un campo de deriva a los electrones ionizados al aplicarles un voltaje entre el ánodo y el cátodo. Unos milímetros antes del ánodo esta situado otro electrodo que forma una zona de electroluminiscencia al aplicarse un campo eléctrico mayor entre éste y el ánodo. Justo detrás del ánodo esta situado el plano de trazas, donde unos circuitos de Kapton mantienen 1800 fotomultiplicadores de silicio homogéneamente espaciados 1 cm que permiten la reconstucción de la trayectoria seguida por el electrón. En el lado opuesto de la cámara, el plano de energía compuesto por 12 tubos fotomultiplicadores miden la energía del evento. Estos tubos fotomultiplicadores registran también el inicio del evento permitiendo, al juntar la información de los dos planos, obtener una imagen tridimensional del evento. Los sensores se mantienen en su posición con dos placas de cobre que a su vez, junto con las barras de cobre que rodean la jaula eléctrica, constituyen la pantalla para disminuir el ruido de fondo dentro de la vasija de presión. Todo lo anterior esta colocado dentro de la vasija de presión que permite mantener los 10-15 bares de xenón. El gas se purifica mantiendose en circulación a través de un circuito de válvulas y filtros gracias a un compresor. Por último, una caja móvil de bloques de plomo cubre y apantalla el detector del ruido de fondo proveniente del laboratorio.

Uno de los objetivos del detector NEW y del trabajo presentado en esta tesis es la validación el modelo de radiación de fondo de NEXT. Los estudios realizados en esta tesis comprenden la caracterización de la escalabilidad de un prototipo pequeño (NEXT-DEMO) a un prototipo intermedio y limpio (NEXT-NEW) en términos de radiopureza. Los posibles ruidos de fondo que pueden comprometer la señal a observar en el detector son de tres tipos: cadenas radiactivas naturales en los materiales de construcción, radiactividad ambiental en el laboratorio

y rayos cósmicos (por los cuales es necesario operar en un laboratorio subterráneo). Para la construcción del detector se han tenido en cuenta las posibles impurezas contaminates de los materiales a utilizar. La labor de validación del diseño según los requisitos de radiopureza basado en la simulación de los posibles ruidos de fondo ha permitido identificar varios elementos críticos para los objetivos físicos de NEW (en algunos casos se ha cambiado el diseño y/o el proveedor), la caracterización del propio laboratorio respecto a los objetivos de NEXT y la estimación de su actividad y funcionamiento. Con el modelo desarrollado, una vez validado y actualizado, se puede pronosticar el comportamiento de NEXT-100. Estas simulaciones permiten utilizar los algoritmos de análisis desarrollados para la búsqueda de candidatos $\beta\beta$ y estimar la cotribución de los ruidos de fondo en NEW en un total de 4.5 mHz en la ventana de 0.7–2.7 MeV. También permite la estimación de una medida de la vida media del modo $\beta\beta 2\nu$ con 5σ en 90 días acumulados de datos de bajo background.

Por otra parte también se describe la puesta en marcha del detector en el Laboratorio Subterráneo de Canfranc y su calibración. Durante la fase de puesta en marcha y calibración del detector NEW, se ha llevado a cabo la calibración de los planos de sensores utilizando el método de respuesta a un fotoelectrón bajo la emisión de LED. Este método fue desarrolado en NEXT–DEMO y posteriormente adaptado para NEXT–NEW. La respuesta de los dos planos de sensores, PMTs y SiPMs, es correcta y permite la monitorización de su evolución. El estudio y desarrollo con simulaciones Monte Carlo del análisis para un método de calibración de las aberraciones geométricas y su efecto en la resolución energética, muestra que la utilización de una fuente de $^{83}\mathrm{Kr}^{\mathrm{m}}$ —dentro de los programas de calibraciones con fuentes radiactivas— proporciona un buen método para la medida de diferentes propiedades de la cámara y la utilización de las mismas para corregir deformaciones en los datos obtenidos. Este método es aplicado a los primeros datos del detector NEW obteniendo resultados prometedores de resolución energética $< 1\%$ extrapolada al $Q_{\beta\beta}$. Los datos también proporcionan algunas claves para la mejora del método así como de algunos aspectos del detector para su posterior funcionamiento de manera estable y continua.

"There are four questions:
What we know; what we
think we know; what we
think that we don't know;
and what we know that
we don't know."

JJ

Preface

Since the postulation of the neutrino by W. Pauli to explain the missing energy in the beta decays until the their discovery 26 years later by C.L. Cowan and F. Reines, that time would be plenty of questions and unknowns. In the same way as the period when the solar neutrino problem arise until the neutrino oscillation discovery, opening further unknowns. The massiveness of the neutrino showed physics beyond the Standard Model and the mechanism that can give mass to the neutrino could bring some answers to the universe existence but also open new questions. The tendency of the physics community to demonstrate that the neutrino could be a Majorana particle (it means its own antiparticle) is one of the leading open questions in particle physics. If so, the best way to demonstrate the Majorana nature of the neutrino is the neutrinoless double beta decay ($\beta\beta0\nu$). The $\beta\beta0\nu$ is a postulated nuclear transition in which two neutrons undergo β decay simultaneously without the emission of neutrinos.

NEXT (Neutrino Experiment with a Xenon TPC) Collaboration is a neutrinoless double-beta decay experiment that operate at the Canfranc Underground Laboratory (LSC). It is an electroluminescent high-pressure gaseous xenon time projection chamber based on separated-function capabilities for calorimetry and tracking. Energy resolution and background suppression are the two keys features of any $\beta\beta0\nu$ experiment. NEXT has both good energy resolution ($< 1\%$ FWHM) and an extra handle for background identification (track reconstruction). The goal of the collaboration is the operation of NEXT-100, a 100 kg of enriched ^{136}Xe isitope detector for $\beta\beta0\nu$ searches. Currently the Collaboration is operating a intermediate detector, NEXT-NEW, to validate the technology and the background predictions.

This thesis is focused on the NEW detector design and commissioning. Therefore, the key concepts of neutrino physics are described in Chapter 1 with some background of the historical achievements. Chapter 2 is devoted to the neutrinoless double beta decay process, its explanation and how can be observed. In this sense, the experimental access to the observable rate and its relation with the experimental parameters to take into account for designing a $\beta\beta0\nu$ experiment is discussed. Moreover, the current techniques for $\beta\beta0\nu$ searches are described.

Chapter 3 introduces the experimental concept of NEXT as well as the Collaboration project description of the different stages.

The main contributions of this thesis to the NEXT project, is related to the NEW detector; therefore a extended description of all the detector components is done in Chapter 4 in order to follow the contributions made.

In Chapter 5 this thesis describes the background model of NEXT which will be validated during the first phase of the experiment using the NEW detector. Detailed NEW detector simulation and quantification of the detector radiopurity by material screening campaign has been done. This helped to the design and building of the NEW detector. The model developed leads to the determination of the sensitivity to a measurement of $\beta\beta2\nu$ mode in NEW.

The other main contribution, discussed in Chapter 6, is the novel detector calibration technique using $^{83}\mathrm{Kr}^{\mathrm{m}}$ source during commissioning. The study of its feasibility with MC simulation as well as the first data results for this calibration technique are shown. Finally, Chapter 7 summarizes and concludes.

In addition, although could be not chronologically ordered, the contribution to the prototype NEXT-DEMO is also shown (Appendix 7) because of its latter application on the NEW calibration.

Contents

"The richness and the humor with which Nature has written her mystery, in an international language that can be read by curious people of all nations, is beautiful, awesome and humbling."

Brian Cox from John N. Bahcall lecture published 29 June 2000

Chapter 1

An introduction to neutrino physics

All known physical interactions can be described in terms of four fundamental forces: gravitational, electromagnetic, strong and weak. The Standard Model (SM) of particle physics deals with the last three, leaving aside gravity due to the lack of a quantum field theory describing it and its relative weakness compared to the other forces (10^{-29} the strength of the weak force, 10^{-36} the strength of the electromagnetic force and 10^{-38} the strength of the strong force).

The Standard Model was introduced by Glashow [1], Weinberg [2] and Salam [3] as a unification of the contribution of many others during the first decades of the second half of the 20th century with the advances in the theory running in parallel to the experimental discovery of many new particles and phenomena. The SM establishes the building blocks of matter: three families of quarks and leptons (both fermions, half-integer spin) with its corresponding antiparticles and their interaction mediators bosons (integer spin). Figure 1.1 shows a graphical representation of the SM.

Among quarks and leptons, neutrinos are, arguably, the most singular and, certainly, the most elusive. With a tiny mass, no electric charge and interacting only via the weak force, they were long believed to be undetectable in spite of being the second most abundant particle in the universe after photons. Their detection in the Cowan-Reines

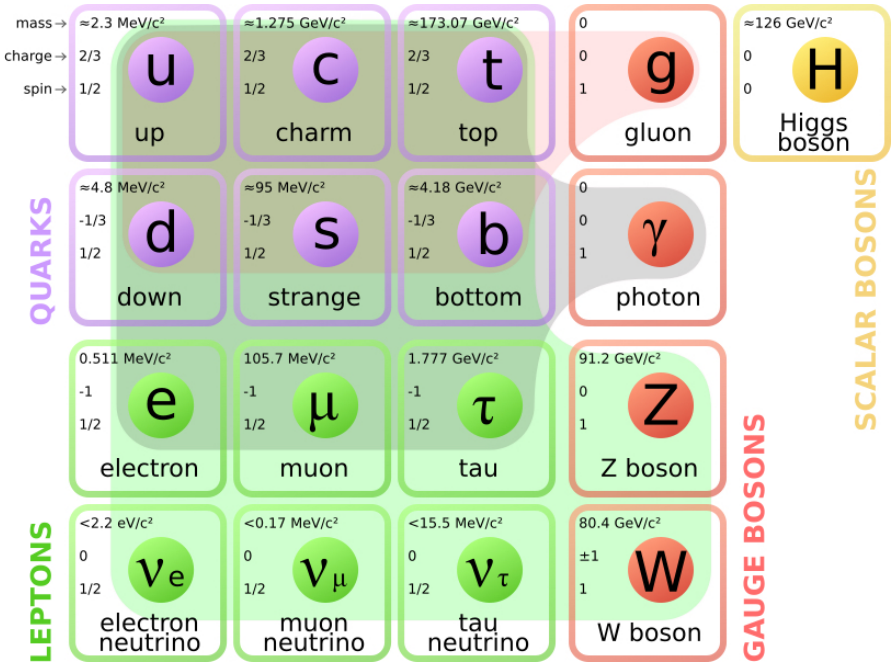

Figure 1.1: Schematic depiction of the Standard Model of elementary particles. It shows in the first three columns the generations of fermionic matter; in the fourth the gauge bosons, mediators of the strong, electromagnetic and weak interactions; and in the fifth column, the Higgs boson, manifestation of the scalar field responsible for the mass of the different particles [4].

experiment in 1956 [5], twenty five years after their postulation by Pauli in his famous letter to the *"Liebe Radioacktive Damen und Herren"* meeting in Tübingen (Germany) explaining the missing energy in the beta-decay [6], opened the doors to the study of these *special* particles. Since then it has shaken the paradigm of particle physics at least a couple of times and the story is not over.

1.1 A history of neutrino masses

One of those beautiful stories that led to fundamental discoveries in that fascinating puzzle that is Nature, with the involvement of some of the most clever minds over a century, was the so–called *"Solar neutrino problem"* [7]. In the mid-nineteenth century, issues such as the age of the Sun, how does it shine or for how long it will do it were crucial scientific questions since the Sun was believed to have a "fundamental role in all human life" by John Herschel [8]. Physicists began to study the energy source of the Sun convinced that gravitation was responsible. In Lord Kelvin's hypothesis the available energy in the Sun came from the gravitational energy of the meteors that, supposedly, had formed it [9]. He estimated a much lower life than Darwin did from geological and biological arguments turning the solar problem into inter-disciplinary science [10]. With the new discoveries of natural radioactivity in the early twentieth century by Henri Becquerel, Marie Curie and Ernest Rutherford, a new source of energy was revealed [11]. Kelvin and Darwin soon pointed to radioactivity as source of the sun–radiated energy.

However, astronomical observations showed absence of radioactive materials in the sun and mostly a gaseous hydrogen composition. The observation of other stars pointed to a radiation energy dependence on its interior temperature unlike radioactivity. Nevertheless they were already pointing in the right direction because with Einstein's theory of the equivalence of mass and energy [12], the fusion of hydrogen nuclei to form a helium nucleus with significantly less mass than the sum of the hydrogen masses, the release of huge amounts of energy was possible.

Gamow and Teller calculated the probability of nuclei to get close enough deriving the rate of nuclear fusion reactions at the high tem-

peratures of the interior of the stars [13]. Based on that, Hans Bethe published in 1938 "Energy production in stars"[14] analyzing different nuclear processes, selecting the *p-p chain* ($^1_1\mathrm{H} + ^1_1\mathrm{H} \longrightarrow ^2_1\mathrm{H} + \mathrm{e}^+ + \nu_\mathrm{e} +$ 0.42 MeV) for Sun–like or lighter stars and the *CNO cycle* (summarized in: $4\,^1_1\mathrm{H} + 2\mathrm{e}^- \longrightarrow ^4_2\mathrm{He} + 2\mathrm{e}^+ + 2\mathrm{e}^- + 2\nu_\mathrm{e} + 3\gamma + 24.7$ MeV $\longrightarrow ^4_2\mathrm{He} + 2\nu_\mathrm{e} + 3\gamma + 26.7$ MeV) for massive stars. These processes allowed him to calculate the temperature of the Sun and the relation between stellar mass and stellar luminosity in good agreement with observations. This triggered a lot of work on calculations of luminosities of Sun-like stars and their evolution on one hand, and on the other hand measurements of the nuclear fusion details of the two chains. A test of the nuclear burning hypothesis using photons was not possible since it would take a photon from the centre of the Sun almost 10 million years to reach the surface, therefore the only viable media with which to detect nuclear fusion in the Sun were neutrinos.

At that time, the existence of neutrinos had already been confirmed by Clyde Cowan and Fred Reines in 1956 in an experiment using the antineutrinos emitted by a nuclear reactor [5], almost thirty years after Pauli's proposal of neutrinos as a solution to the missing energy in radioactive beta decays [6]. That encouraged Raymond Davis and John Bahcall in 1964 to fill a 380 m^3 tank with cleaning fluid (perchloroethylene) at the Homestake gold mine [15] using the radiochemical detection method proposed by Pontecorvo (inverse beta-decay: $\nu_\mathrm{e} + ^{37}\mathrm{Cl} \longrightarrow ^{37}\mathrm{Ar} + \mathrm{e}^-$) [16]. With the predicted rate of solar neutrinos, only a few atoms of ^{37}Ar, produced by electron neutrino interactions, would be counted per week. Even though about 6.5×10^{10} solar neutrinos pass through a square centimeter per second on Earth, their small interaction cross section made them a truly technical challenge to detect. The visionary experiment succeeded but only a third of the expected neutrinos were detected. That deficit of neutrinos detected with respect to the expected number of neutrino computed with the standard solar model was called the *"Solar neutrino problem"*.

1.2 Neutrino oscillations and mixing

To understand the deficit of neutrinos coming from the Sun, several experiments tried to measure their production rate. Kamiokande changed

its original purpose, the detection of nucleon decay [17], increasing its sensitivity to solar neutrinos by detecting the Cherenkov radiation emitted by recoiling electrons from elastic neutrino scattering. They confirmed the disagreement observed by Davis [18] and the solar origin of the neutrinos by directionality measurements [19].

Later on, SGAE [20], GALLEX [21] (both radio-chemical experiments as Homestake) and Super-Kamiokande [22] results confirmed the solar neutrino energy spectrum as predicted and made measurements of the core temperature of the Sun consistent with hypotheses. However, they also supported the measured discrepancy between measured and predicted flux [23]. Someone once said: "Even when everything seems to behave in theory there is a tendency always in nature to dodge our understanding".

Pontecorvo in 1957–58 explored the possibility of particle mixing and oscillation in the lepton sector [24, 25], as the mixing and oscillation of kaons was already confirmed experimentally. That would allow $\nu \longleftrightarrow \bar{\nu}$ oscillations, meaning that neutrino and antineutrino are mixed particles.

In 1962 Maki, Nakagawa and Sakata [26] introduced neutrino mixing, defining a "true neutrino" as a combination of different neutrino types, now known as flavors, by that time, only ν_e and ν_μ. According to that, neutrinos produced, for instance in the Sun, are a mixture of individual states that have small masses that allow them to change from mostly one state to other while traveling, glimpsing a possible explanation to the experimentally missing neutrinos. The experiments were sensitive mostly to the ν_e state but if changed during the flight they could pass by without interacting.

By that time, massless neutrinos was the dominant idea but Wolfenstein and Smirnov showed (1978 [27] and 1985 [28] respectively) that if they have a small but non zero mass, their interaction with matter moving through the sun could increase the probability that they oscillate to another state thus explaining the missing electron neutrinos. The problem was solved when Super-Kamiokande observed the oscillation in neutrinos produced in the atmosphere by cosmic ray collisions in 1998 [29]. Later SNO confirmed this flavor change in solar neutrinos in 2001 [30] and KamLAND in reactor-produced antineutrinos in 2002-2007 [31]. The discovery of neutrino oscillations and the implication

of the mass of the neutrino are the first observation of physics beyond the SM.

The oscillation between neutrino flavors is due to the fact that neutrinos are a linear superposition of the three possible mass states. Neutrinos are produced via charged-current weak interactions in flavor eigenstates (ν_l) that are a linear combination of mass eigenstates (ν_i):

$$|\nu_l\rangle = \sum_i U_{li}^* |\nu_i\rangle \tag{1.1}$$

where $l = e, \mu, \tau$ and $i = 1, 2, 3$, showing that a specific mixture of mass eigenstates yields the neutrino flavor l. This expression can also be inverted to depict every mass eigenstate ν_i as an analogous linear combination of three flavors (as shown in Figure 1.2). The amount of flavor l in the mass eigenstate i will be given by $|U_{li}|^2$, where U_{li} is the li element of the Pontecorvo-Maki-Nakagawa-Sakata (PMNS) matrix [32]:

$$U_{PMNS} = \begin{pmatrix} 1 & 0 & 0 \\ 0 & c_{23} & s_{23} \\ 0 & -s_{23} & c_{23} \end{pmatrix} \begin{pmatrix} c_{13} & 0 & s_{13}\mathrm{e}^{\mathrm{i}\delta} \\ 0 & 1 & 0 \\ -s_{13}\mathrm{e}^{\mathrm{i}\delta} & 0 & c_{13} \end{pmatrix} \begin{pmatrix} c_{12} & s_{12} & 0 \\ -s_{12} & c_{12} & 0 \\ 0 & 0 & 1 \end{pmatrix} \begin{pmatrix} 1 & 0 & 0 \\ 0 & \mathrm{e}^{\mathrm{i}l_1} & 0 \\ 0 & 0 & \mathrm{e}^{\mathrm{i}l_2} \end{pmatrix} \tag{1.2}$$

where $c_{ij} = \cos\theta_{ij}$ and $s_{ij} = \sin\theta_{ij}$, with θ_{12}, θ_{13} and θ_{23} the three mixing angles. δ is the Dirac CP-violating phase, and the last matrix is the identity matrix if neutrinos are Dirac fermions or instead l_1 and l_2 are the Majorana phases that will be explained later (§ 1.3).

When a neutrino propagates (through vacuum or matter), the mass eigenstate is the one that propagates. This means it is created or emitted, via weak interaction, by a source along with a charged lepton $\overline{\ell_\alpha}$ of flavor α. After traveling a distance L, at the target, the neutrino interacts and these interactions create another charged lepton ℓ_β of flavor β. The probability for flavor transition will be given by

$$\begin{aligned} P(\nu_\alpha \to \nu_\beta) = |\langle \nu_\beta | \nu_\alpha(t) \rangle|^2 &= \left| \sum_i \sum_j U_{\alpha i}^* U_{\beta j} \langle \nu_j | \nu_i(t) \rangle \right|^2 \\ &\approx \sum_{i,j} U_{\alpha i}^* U_{\beta i} U_{\alpha j} U_{\beta j}^* \, \mathrm{e}^{-\mathrm{i}\Delta \mathrm{m}_{\mathrm{ij}}^2 \mathrm{L}/2\mathrm{E}} \end{aligned} \tag{1.3}$$

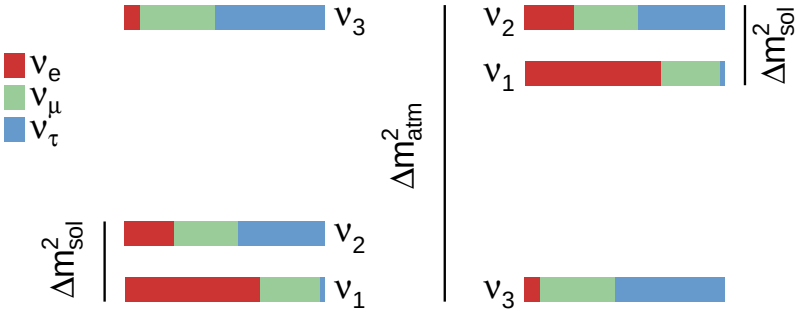

Figure 1.2: Possible neutrino spectra (left, Normal Ordering; right, Inverted Ordering) with the flavor content of the three neutrino mass eigenstates from data [34]. Neutrino masses increase from bottom to top. Note that for the atmospheric and accelerator based mass squared difference measurement, $\Delta m^2_{3\ell} \equiv \Delta m^2_{31} > 0$ for Normal Ordering (left) and $\Delta m^2_{3\ell} \equiv \Delta m^2_{32} < 0$ for Inverted Ordering (right).

with $\Delta m^2_{ij} = m^2_i - m^2_j$ [33]. The probability for flavor transition is hence a periodic function of the distance between the source and the detector.

An illustrative case of the formula is the case where only two flavors participate in the oscillation. The two-neutrino oscillation is a rather rigorous description of a vast number of experiments. When only two neutrinos are relevant,

$$\mathrm{P}(\nu_\alpha \longrightarrow \nu_\beta) = \sin^2 2\theta \sin^2 \left(\frac{\Delta m^2 \, L}{4E} \right). \tag{1.4}$$

Therefore, for the experimental design the $E/L \propto \Delta m^2$ is the key parameter as shown in Figure 1.3.

Our current knowledge of the oscillation parameters for a three neutrino mixing model, from global fits to all available oscillation data [34] is summarized in Table 1.1.

The mixing angles have been measured, showing large values (implying more mixing) in contrast to the quark mixing (CKM matrix).

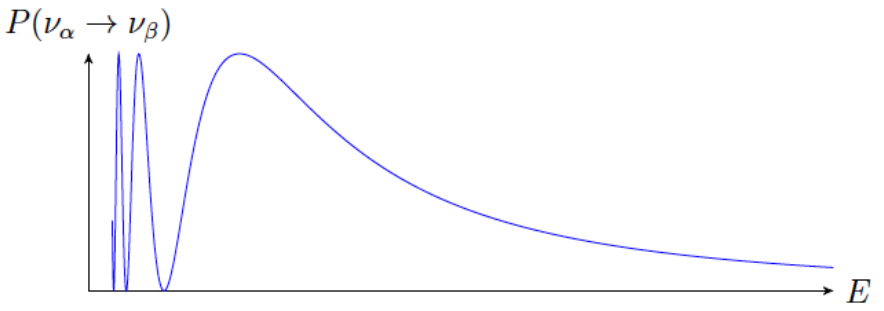

Figure 1.3: Oscillation probability for two neutrino flavors as a function of the neutrino energy with a fixed baseline L.

Those are: the *solar* mixing angle $\theta_{12} \simeq 34°$, the *atmospheric* mixing angle $\theta_{23} \simeq 42°$, and *reactor* mixing angle $\theta_{13} \simeq 8°$ named by their main measurement channel. The mixing matrix of three neutrinos also includes CP violating phases. The so-called Dirac phase, δ, induces CP violation in neutrino oscillations, that is, a difference between $P(\nu_\alpha \to \nu_\beta)$ and $P(\bar{\nu}_\alpha \to \bar{\nu}_\beta)$, for $\alpha \neq \beta$.

In addition to the Dirac phase, two Majorana phases (l_1, l_2) arise in the U_{PMNS} if neutrinos are Majorana particles (see § 1.3). As the transition or survival probabilities depend on the combination $U^*_{\alpha i}U_{\beta i}$, no trace of the Majorana phases could appear in oscillation phenomena, however they will have observable effects in those processes where the Majorana character of the neutrino is essential for the process to happen, like neutrino-less double beta decay [33] (see Chapter 2).

The oscillation experiments only provide access to the square mass differences ($\Delta m^2_{ij} = m^2_i - m^2_j$) of the three light ($m_i < 1$ eV) neutrino mass eigenstates, but not to the absolute mass. The difference between m_2 and m_1 has been measured by solar and reactor based experiments while Δm^2_{32} by atmospheric and accelerator based experiments.

In this convention there are two non-equivalent orderings for the neutrino masses: normal ordering (NO) with $m_1 < m_2 < m_3$, and inverted ordering (IO) with $m_3 < m_1 < m_2$. Furthermore the data shows a relatively large hierarchy between the mass splittings, $\Delta m^2_{21} \ll |\Delta m^2_{31}| \simeq |\Delta m^2_{32}|$ (see Figure 1.2).

	Normal Ordering		Inverted Ordering	
	best fit $\pm 1\sigma$	3σ range	best fit $\pm 1\sigma$	3σ range
$\theta_{12}(^\circ)$	$33.56^{+0.77}_{-0.75}$	$[31.38, 35.99]$	$33.56^{+0.77}_{-0.75}$	$[31.38, 35.99]$
$\theta_{23}(^\circ)$	$41.6^{+1.5}_{-1.2}$	$[38.4, 52.8]$	$50.0^{+1.1}_{-1.4}$	$[38.8, 53.1]$
$\theta_{13}(^\circ)$	$8.46^{+0.15}_{-0.15}$	$[7.99, 8.90]$	$8.49^{+0.15}_{-0.15}$	$[8.03, 8.93]$
$\delta_{\rm CP}(^\circ)$	261^{+51}_{-59}	$[0, 360]$	277^{+40}_{-46}	$[145, 391]$
Δm^2_{21} $(10^{-5}\ {\rm eV}^2)$	$7.50^{+0.19}_{-0.17}$	$[7.03, 8.09]$	$7.50^{+0.19}_{-0.17}$	$[7.03, 8.09]$
$\Delta m^2_{3\ell}$ $(10^{-3}\ {\rm eV}^2)$	$+2.524^{+0.039}_{-0.040}$	$[+2.407, +2.643]$	$-2.514^{+0.038}_{-0.041}$	$[-2.635, -2.399]$

Table 1.1: Three-flavor oscillation parameters from global fit to all oscillation data [34]. Note that $\Delta m^2_{3\ell} \equiv \Delta m^2_{31} > 0$ for NO and $\Delta m^2_{3\ell} \equiv \Delta m^2_{32} < 0$ for IO.

There are a number of other questions which are left unanswered by the SM that are nowadays the subject of intense research: dark matter and dark energy, baryon asymmetry, CP violation... However, for now, the only confirmed beyond-the-standard-model observation is that of neutrino mass. It is worth mentioning that, for instance, quite a few WIMP dark matter detectors and double beta decay detectors share technological approaches for rare event searches. Thus the interconnection between these fields addressing the smallest (neutrinos) and largest (cosmology) physical scales is also present in their experimental approaches.

1.3 Nature of neutrino masses

In the last two decades, oscillation experiments have pushed our understanding of neutrino physics, but there are still a number of issues that remain unknown, and perhaps the most important is the origin and nature of neutrino masses.

Neutrinos are the most elusive fermions in the SM, they do not carry electromagnetic or color charge and only interact via the massive weak gauge bossons. This was already foretold by W. Pauli in his ν_e existence postulation: *"I have done a terrible thing, I have postulated*

a particle that can not be detected" [35]. However, their existence was experimentally confirmed and their detection has established two milestone features of the SM: the three family structure and the left-handedness of the weak interaction [36]. Section § 1.3.1 of this chapter is devoted to discussing how neutrinos obtain mass and the main concepts on the nature of the weak interaction needed to understand it.

The family structure was measured with high precision in LEP, through the measurement of the Z resonance width, to be $N_\nu = 2.984 \pm 0.008$ [37] active, light neutrinos. Also, astrophysics and cosmology measurements indicate that the number of stable neutrinos is $N_{\mathit{eff}} = 3.046$ [37], although this is model dependent and could vary strongly depending on the datasets. If the SM were to have an extra family of heavier unobserved quarks and charged leptons, this family would also have standard neutrinos which would have been measured.

Figure 1.4 shows the three families of fermions as well as the large difference in mass scale (at least 6 orders of magnitude) between the upper limits on the neutrino masses and the measured masses of the other fermions. A theory that can provide a possible explanation for this difference will be discussed in § 1.3.1. The underlying nature of this apparently different origin could be new physics, but it seems necessary to study how it works from one of the things we know, its weak interaction.

1.3.1 Physics that gives rise to the neutrino mass

In the Standard Model, fermion masses result from the Yukawa interactions with the Higgs field following the Lagrangian [38]:

$$-\mathcal{L}_{\text{Yukawa}} = \sum_{\alpha,\beta=e,\mu,\tau} Y^l_{\alpha\beta} \overline{L_{\alpha L}} \Phi l_{\beta R} + \text{H.c.} \tag{1.5}$$

where

$$L_{lL} \equiv \begin{pmatrix} \nu_{lL} \\ l_L \end{pmatrix}, \qquad \Phi \equiv \begin{pmatrix} \Phi^{(+)} \\ \Phi^{(0)} \end{pmatrix} \tag{1.6}$$

are the leptonic weak-isospin doublet and Higgs doublet respectively; Y^l the Yukawa couplings and l_R the leptonic singlets ($l = e, \mu, \tau$).

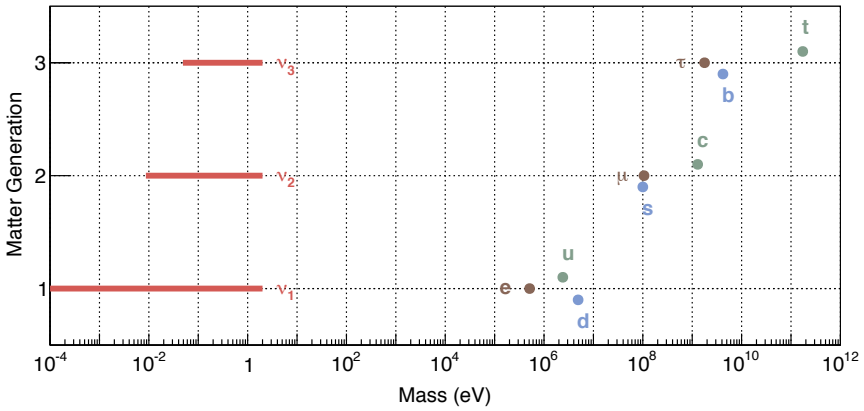

Figure 1.4: Mass scale of the standard model fermions assuming normal ordering [37].

Let us introduce here the concept of *chirality*: above, the subscripts L (for left-handed) and R (for right-handed) refer to the negative and positive chirality components of a fermion field Ψ that satisfy $\Psi = \Psi_L + \Psi_R = P_L\Psi + P_R\Psi$, where $P_L = (1-\gamma_5)/2$ and $P_R = (1+\gamma_5)/2$.

As we will see later, the ν_i mass eigenstates are a quantum superposition of chiral states.

On the other hand *helicity* is related to the orientation of a fermion's spin along the axis of its linear momentum. A fermion is said to be "left-handed" if its spin points anti-parallel to its direction of travel and "right-handed" if its spin points parallel to its direction of travel. It should not be confussed with the chirality, one possible key of differentiation is that helicity is a characteristic that can be measured (by looking at angular momentum) while chirality is not (right- or left-handed under transformation of Poincare group of the particle field). In the massless limit, helicity and chirality are equivalent.

In 1957 Chien-Shiung Wu and collaborators [39] determined the left-handedness of the weak interaction along with the demonstration of parity violation. That is to say, that in the SM only left-handed fermions and right-handed anti-fermions couple to the W boson. As an example, the W bosons will only talk to left-chiral electrons and

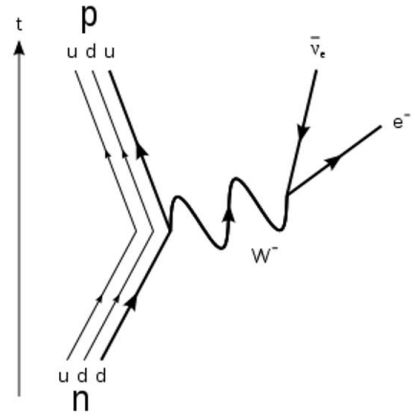

Figure 1.5: Feynman diagram of the beta decay. The weak force is responsible for neutrino interactions. For example, when a neutron converts into a proton the process is mediated by a change of its internal components (quarks), emitting a W boson that decays into an electron and an electron antineutrino.

right-chiral positrons and refuse to talk to left-chiral positrons and right-chiral electrons.

Focusing on our case of study, only left-handed neutrinos have been detected [40] and have been shown to be massive (§ 1.1). Before that time, the SM accommodated massless neutrinos because there was no evidence of either mass or right-handed fields, and the proposed mechanism to get mass was the Higgs left-right coupling. Now in order to add a mass to the neutrino, the SM has to be extended. The SM gauge invariance does not imply lepton number symmetry, thus total lepton number may or may not be a symmetry depending on the neutrino nature. Therefore, there could be two ways of obtaining the mass: *a la Dirac* or *a la Majorana*, after spontaneous symmetry breaking [38]. To introduce such a coupling in the SM for neutrinos, we need to identify the neutrino right-handed states, which in the SM are absent.

Dirac mass term

Dirac neutrino masses can be easily accommodated in the SM introducing the right-handed components ν_{lR} of the neutrino fields ($l = e, \mu, \tau$) [38]. These fields are called *sterile* [36] because they do not participate in weak, strong or electromagnetic interaction and only feel the gravitational interaction. The left-handed neutrino fields are instead *active*.

Then, after spontaneous symmetry breaking, from Equation 1.5 with the term of the Dirac neutrinos fields we obtain

$$-\mathcal{L}^{D}_{mass} = \sum_{i=1}^{3} \frac{y^{\nu}_{i} v}{\sqrt{2}} \overline{\nu_{iL}} \nu_{iR} + \text{H.c.} = \sum_{i=1}^{3} m_{Di} \overline{\nu_i} \nu_i \tag{1.7}$$

where $\nu_i \equiv \nu_{iL} + \nu_{iR}$ and the mass term $m_{iD} \equiv \frac{y^{\nu}_{i} v}{\sqrt{2}}$ (with $i = 1, 2, 3$). The neutrino masses obtained are proportional to the Higgs vacuum expectation value (VEV) v, like the masses of charged leptons and quarks. The Yukawa couplings y^{ν}_{i} must be of the order of 10^{-12} or smaller to account for the mass scale suggested by neutrino oscillations (§ 1.2), 6 orders of magnitude smaller than that of the lightest charged lepton (see Figure 1.4), making the explanation of the origin of neutrino

masses with a Dirac mass term alone unsatisfactory [36, 41]. Note that in this case lepton number is accidentally conserved.

Majorana mass term

The other way to obtain the mass is introducing a Majorana mass term to the SM. Ettore Majorana proposed in 1937 [42] that for neutral particles two of the four degrees of freedom in a massive spinor field can be removed imposing $\nu^c = \nu$, where c is the charge conjugation operation. Neutrinos are the only SM fermions compatible with charge conservation [36]. Therefore, the neutrino chiral fields satisfy that

$$\nu_R \to (\nu_L)^c = C\bar{\nu}_L^T \tag{1.8}$$

where C is the operator of charge conjugation in spinor space. Subsequently Equation 1.7 can be rewritten as

$$-\mathcal{L}_{mass}^{M,L} = \frac{1}{2} m_L \overline{(\nu_L)^c} \nu_L + \text{H.c.} \tag{1.9}$$

where m_L is a free parameter with dimensions of mass. This mass term is thus constructed from left-handed (negative-chirality) neutrino fields alone.

Note that from Equation 1.8, that converts particles into their own antiparticles, SM total lepton number conservation is violated ($|\Delta L| = 2$). The same condition also forbids such a mass term for all electrically charged fermions.

In addition, if right handed neutrino fields also exist and are independent, we can likewise from Equation 1.7, have

$$-\mathcal{L}_{mass}^{M,R} = \frac{1}{2} m_R \overline{(\nu_R)^c} \nu_R + \text{H.c.} \tag{1.10}$$

Here ν_R fields are SM weak-isospin singlets and so the free parameter m_R is not connected to a Higgs VEV and may be orders of magnitude larger than the electroweak scale.

In both (L, R) cases, after spontaneous symmetry breaking $m_\nu = \alpha_\nu v^2$, being proportional in this case to the square of Higgs VEV and $\alpha_\nu = y/\Lambda$ the coupling over a new physics scale (Λ), in principle unrelated to the electroweak scale [43]. If the scale Λ is much larger than

the electroweak scale v, a strong hierarchy between the neutrino and the charged lepton masses arises naturally in addition to the neutrino mass term. The fact that the neutrino mass is inversely proportional to an energy scale is referred as the *see-saw* mechanism [44, 45, 46, 47], providing an explanation to the smallness of the neutrino masses asuming lepton number violation by a right-handed Majorana mass term at large scale.

The *see-saw* mechanism is today the most popular BSM theory behind the mystery of tiny neutrino mass. According to this mechanism, the origin of neutrino mass is attributed to the existence of heavy right-handed neutrinos. The light neutrinos are the ones observed in current experiments while the heavy neutrinos are not accessible to current experiments (GUT scale) and could be responsible for the baryon asymmetry of the universe through the generation of a lepton asymmetry at very high energy scales since their decays can in principle be CP violating [33].

Furthermore, with the demonstration of the Majorana nature of the neutrino, primordial leptogenesis could be explained by neutrino genesis; the Standard Model allows little CP violation due to the only single phase for the Dirac fermion but with the three Majorana phases this can be large, explaining the CP asymmetry [43].

In the next section the experimental searches for measuring not only the neutrino mass but its Dirac or Majorana nature determination are described.

1.4 Measuring the mass of neutrinos

We have discussed in the previous sections the evidence that neutrinos have mass and the possible mechanisms that give them mass, but it is not known yet what is its absolute mass. The standard three light and active neutrino framework exposes the smallness of the neutrino masses and the peculiar pattern of the lepton mixing compared with the quark one. The most sensitive experimental channels to access the neutrino mass are: beta decay experiments, cosmology probes and neutrinoless double beta decay experiments.

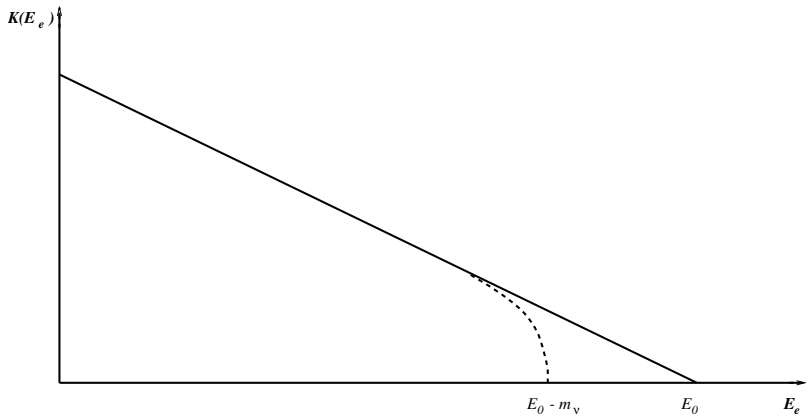

Figure 1.6: Effect of a neutrino mass in the end-point of the lepton energy spectrum in β decay [36].

1.4.1 Beta decay

If neutrinos are massive, the end point of the lepton energy spectrum in weak decays changes. Each specific beta decay (β-decay) transition is characterized by a fixed decay energy (Q-value). Because the energy of the recoil nucleus is virtually zero, this energy is shared between the beta particle and the "invisible" neutrino [48]. So the beta particle energy range from zero to the beta endpoint energy or Q-value (see Figure 1.6). The difference between the energy released by the β-decay and the Q-value gives the effective electron neutrino mass.

The mass flavor eigenstate of the electron neutrino is the sum of all the mass eigenstates with its corresponding PMNS matrix elements:

$$m_{\nu_e} = \mid U_{e1} \mid^2 m_1 + \mid U_{e2} \mid^2 m_2 + \mid U_{e3} \mid^2 m_3 \tag{1.11}$$

giving a model independent (no Dirac or Majorana phases involved) neutrino mass scale.

Table 1.2 present actual neutrino mass limits from beta decay experiments.

This already shows that neutrinos can be extremely light but massive. New generation experiments like KATRIN [52] will have sensitivity down to $\sim$ 200 meV, but cosmological constraints imply that this may be insufficient to make a positive measurement.

ν	$\beta - decay$	limit
ν_e	$H^3 \rightarrow {}^3He + e^- + \bar{\nu}_e$	$m_{\nu_e} < 2.1$eV [49]
ν_μ	$\pi^+ \rightarrow \mu^+ \nu_\mu$	$m_{\nu_\mu} < 170$keV [50]
ν_τ	$\tau \rightarrow 5\pi\nu_\tau$	$m_{\nu_\tau} < 18.2$MeV [51]

Table 1.2: Beta decay neutrino mass limits for each neutrino flavor and its measurement channel.

1.4.2 Cosmology

The neutrino is the second most abundant known particle in the universe after photons. The fact that neutrinos are massive has effected the development of the universe. Therefore, cosmological studies (distribution of galaxies and CMB) are sensitive to the sum of the neutrino masses

$$m_{\text{cosmo}} = \sum_i m_i \tag{1.12}$$

Most recent results by combination of PLANCK and WMAP data give $\sum\ m_i\ <\ 0.23$ eV (0.95% CL) [53] and no extra neutrino states.

1.4.3 Neutrinoless double beta decay

Neutrinoless double beta decay ($\beta\beta0\nu$) can help measuring the mass scale given that it can access the coherent sum of the mass eigenstates with respect to the PMNS mixing matrix

$$m_{\beta\beta} = \mid \sum m_i U_{ei}^2 \mid = \mid m_1 c_{13}^2 c_{12}^2 + m_2 c_{13}^2 s_{12}^2 e^{2i\alpha} + m_3 s_{13}^2 e^{2i\beta} \mid \tag{1.13}$$

with the caveat of the complex CP phases, giving a model dependent neutrino mass measurement. What is more important, it would reveal the Majorana neutrino nature. Chapter 2 is fully devoted to discussing $\beta\beta0\nu$ theory and experimental approaches.

Although the determination of the mass hierarchy can be done by oscillation experiments (matter effects on the 1-3 mixing by studying the atmospheric neutrino fluxes, precise measurements of Δm^2 with

reactor neutrinos or LBL neutrino experiments [54]) as well as β decay, cosmology or even precision neutrino mass spectroscopy [55] can access also the neutrino mass scale; neutrinoless double beta decay can, in addition, determine the neutrino nature.

"Each time new experiments are observed to agree with the predictions the theory survives, and our confidence in it is increased; but if ever a new observation is found to disagree, we have to abandon or modify the theory."

Stephen Hawking
"A Brief History of Time"

Chapter 2

Neutrinoless double beta decay

Historically beta decays provided the first experimental data of the weak interaction by the study of radioactivity (oddly enough, the same that we will try to avoid in our experiment). In this nuclear transition the weak interaction converts a nucleon (a neutron or a proton) into the other, emitting in the process an electron and a neutrino by the intermediate $W^{\mp}$ boson: $n \longrightarrow p\ e^{-}\ \overline{\nu}_e$, $p \longrightarrow n\ e^{+}\ \nu_e$. These are named β^{-} (can be seen in Figure 1.5) and β^{+} decay respectively. It is included in these nuclear processes (due to the same weak force nature) the atomic electron capture (EC) of a Z nucleus producing a Z-1 nucleus with the same A and a neutrino. In some even-even nuclei, only the second order weak transition of double beta decay is allowed, where the single beta decay is energetically forbidden or highly suppressed (see Figure 2.2) [56]. As we will see in § 2.2 neutrinoless double beta decay processes could provide significant information on the neutrino mass, the mass ordering and, more importantly, the neutrino mass nature. Hence, this nuclear process has a profound impact in neutrino physics.

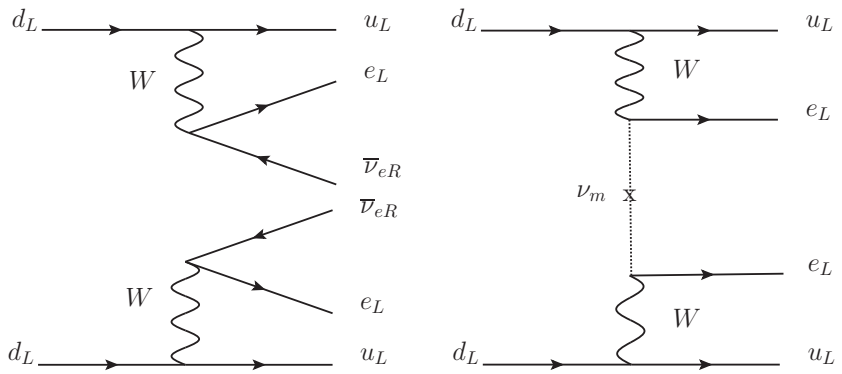

Figure 2.1: (left) Feynman diagram for the double beta decay with neutrinos ($\beta\beta 2\nu$) where the down quarks decay to up quarks, transforming the neutron into a proton, by the emission of an electron and an electronic antineutrino; (right) the neutrinoless double beta decay ($\beta\beta 0\nu$) where the same decay occurs with the virtual exchange of a light Majorana neutrino.

2.1 Double beta decay

In this very slow nuclear transition between two allowed states, the nucleus, unlike in single beta decay, can decay to Z+2 because it is energetically favorable. In the transition, the proton changes to a neutron emitting two electrons and two antineutrinos (Equation 2.1) being equivalent to two simultaneous β-decays. Only a few elements are able to undergo this rare process (35 isotopes) but only for twelve of them (listed in Table 2.1) it has been observed experimentally and its half-life measured to be around $10^{18} - 10^{21}$ yr.

Theoretically if the neutrino is a Majorana particle, that is, its own antiparticle, this process can occur via the exchange of a light Majorana neutrino without any neutrino in the final state (Equation 2.2). This is known as neutrino-less double beta decay ($\beta\beta 0\nu$). Evidence of this process would provide a test of the nature of the neutrino, establishing that massive neutrinos are Majorana particles. It will provide a hint of a new physics scale beyond the Standard Model and prove the violation

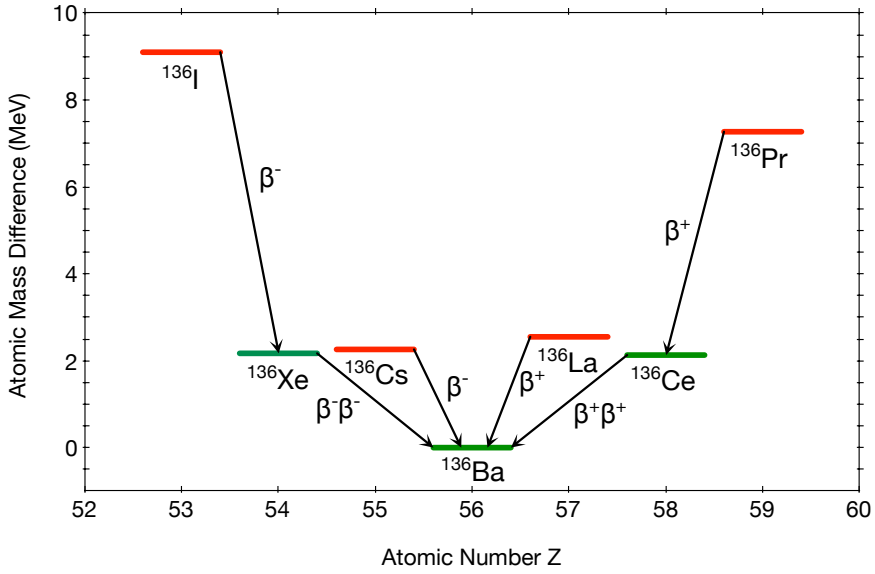

Figure 2.2: Beta (red) and double beta (green) decay energy level scheme for isotopes with A = 136 showing the allowed transitions [57].

of total lepton number, a possible key element to explain the observed asymmetry between matter and antimatter in the universe.

Also, other processes driven by the same underlying physics are: double beta decay with Majoron bosons emission (Equation 2.3, Equation 2.4), quadrupole beta decay or other lepton number violating processes such as double positron emission (Equation 2.5), positron emission plus electron capture (Equation 2.6) and double electron capture (Equation 2.7) [58, 59, 60]. None of those proceses has been observed yet [61, 62, 63, 64, 65]. Although all those processes imply the same physics, i.e. a Majorana mass term in the transition, the double beta decay process is, from the experimental point of view, favored due to the phase space available (*Black box theorem*, for further information see [57, 66]).

$$ {}^{A}_{Z}X \longrightarrow {}^{A}_{Z+2}X + 2e^{-} + 2\overline{\nu}_{e} \tag{2.1} $$

$$ {}^{A}_{Z}X \longrightarrow {}^{A}_{Z+2}X + 2e^{-} \tag{2.2} $$

$$ {}^{A}_{Z}X \longrightarrow {}^{A}_{Z+2}X + 2e^{-} + \chi^{0} \tag{2.3} $$

$$ {}^{A}_{Z}X \longrightarrow {}^{A}_{Z+2}X + 2e^{-} + 2\chi^{0} \tag{2.4} $$

$$ {}^{A}_{Z}X \longrightarrow {}^{A}_{Z-2}X + 2e^{+} \tag{2.5} $$

$$ {}^{A}_{Z}X + e^{-} \longrightarrow {}^{A}_{Z-2}X + 2e^{+} \tag{2.6} $$

$$ {}^{A}_{Z}X + 2e^{-} \longrightarrow {}^{A}_{Z-2}X^{*} \tag{2.7} $$

Isotope	Half-life (10^{21} yr)	Experiment
^{48}Ca	$0.064^{+0.007}_{-0.006}{}^{+0.012}_{-0.009}$	NEMO-3 [67]
^{76}Ge	1.926 ± 0.094	GERDA [37]
^{83}Kr^{m}	$9.2^{+5.5}_{-2.6} \pm 1.3$	BAKSAN [37]
^{82}Se	$0.096 \pm 0.003 \pm 0.010$	NEMO-3 [37]
^{96}Zr	$0.0235 \pm 0.0014 \pm 0.0016$	NEMO-3 [37]
^{100}Mo	0.00693 ± 0.00004	NEMO-3 [37]
^{116}Cd	$0.028 \pm 0.001 \pm 0.003$	NEMO-3 [37]
^{128}Te	7200 ± 400	geochemical [37]
^{130}Te	$0.82 \pm 0.02 \pm 0.06$	CUORE-0 [68]
^{136}Xe	$2.165 \pm 0.016 \pm 0.059$	EXO-200 [69]
^{150}Nd	$0.00911^{+0.00025}_{-0.00022} \pm 0.00063$	NEMO-3 [37]
^{238}U	2.0 ± 0.6	radiochemical [37]

Table 2.1: Half–life of the double beta decay ($\beta\beta2\nu$) allowed isotopes currently measured.

2.2 Neutrinoless double beta decay and Majorana neutrinos

If the neutrino is a Majorana fermion, neutrino and antineutrino would be two different chiral states of the same particle (ν left-handed and $\bar{\nu}$ right-handed) allowing the $\beta\beta0\nu$ process where the pair of virtual W bosons exchange a Majorana neutrino to produce the outgoing electrons (see Figure 2.1). That is to say, at one vertex an electronic neutrino predominantly composed by right-handed chirality state ($\overline{\nu}_e$) is emitted, and only its small left-handed chirality component is absorbed at the other vertex. Thus the interaction depends on the fraction of left-chirality state in the emitted ($\overline{\nu}_e$) and this is proportional to $(m_\nu/E)^2$ [70].

Therefore, the amplitude of the process, the $\beta\beta0\nu$ rate, is proportional to the *effective neutrino Majorana Mass* $m_{\beta\beta}$. The inverse lifetime for this process is given by

$$(T_{1/2}^{\beta\beta0\nu})^{-1} = G^{0\nu} \left|M^{0\nu}\right|^2 \left|\sum_i (U_{PMNS}^{ei})^2 m_i\right|^2 = G^{0\nu}|M_{0\nu}|^2 (\frac{\langle m_{\beta\beta}\rangle}{m_e})^2 \tag{2.8}$$

where $G^{0\nu}$ is a phase space factor, $M_{0\nu}$ is a nuclear matrix element and m_e is the electron mass. The $\langle m_{\beta\beta}\rangle$ is the effective Majorana neutrino mass of the exchanged neutrino. This effective mass is

$$\langle m_{\beta\beta}\rangle = |\sum_{i=1}^{3} U_{ei}^2 m_i| \tag{2.9}$$

where U_{ei} is the matrix mixing element that describes the mixture of neutrino mass state i in the electron neutrino eigenstate.

In spite of the large space factor (compared to the 2ν mode) the suppression due to the neutrino mass yields a lifetime of the order

$$T_{\beta\beta0\nu}^{-1} \sim \left(\frac{m_\nu}{E}\right)^2 10^9 \; T_{\beta\beta2\nu}^{-1}, \tag{2.10}$$

which could be observable for neutrino masses in the eV range. The $\beta\beta2\nu$ is also the SM background of this process, of the order of $T_{\beta\beta2\nu} > 10^{19}$ – 10^{21} years.

Experimental evidence of neutrinoless double beta decay would confirm that total lepton number is violated and the Majorana mass nature of the neutrino. In addition, the measurement of the $\beta\beta0\nu$-decay rate would provide information on the absolute scale of neutrino masses [57] revealing the mass ordering, as shown in Equation 2.8.
The Equation 2.8 also reveals the importance that a precise knowledge of the nuclear matrix elements has in the determination of the half-life. Phase space factors, which depend on the $\beta\beta$ transition energy and the nuclear charge, are calculated with enough accuracy. However, nuclear matrix elements are evaluated using nuclear models and there is some tension between them. Therefore, an absolute mass scale for the neutrino can be established (Equation 2.9) from a positive detection and measurement of the half-life although with an error originated in the nuclear matrix elements (Equation 2.8) [57]. Nevertheless, a negative result on the measurement (meaning no evidence of $\beta\beta0\nu$ event rate) would also provide an upper limit on the $m_{\beta\beta}$ and the lightest mass state (see Figure 2.5 with the actual constraints from null experimental searches) and at some point could uncover the hierarchy although there could be other contributions, i.e. a model dependent ordering determination unlike oscillations.

2.3 Neutrinoless double beta decay experiments

In a double beta decay process the released energy is distributed among the four emitted particles, the two electrons and the two antineutrinos, resulting in a continuous spectrum (Figure 2.3). In the case of $\beta\beta0\nu$, the kinetic energy is divided only between the two electrons, resulting in a mono-energetic line at the Q-value of the decay ($Q_{\beta\beta}$), defined as the mass difference between the parent and daughter nuclides: $Q_{\beta\beta} \equiv \mathrm{M(A, Z)} - \mathrm{M(A, Z + 2)}$. Most of the experimental techniques base their search on the measurement of the sum of the kinetic energies from the two released electrons, which gives rise to a single peak in the $\beta\beta0\nu$ case.

Double beta decay experiments are, in general, calorimeters searching for a small peak at $Q_{\beta\beta}$ in their energy spectrum. Considering

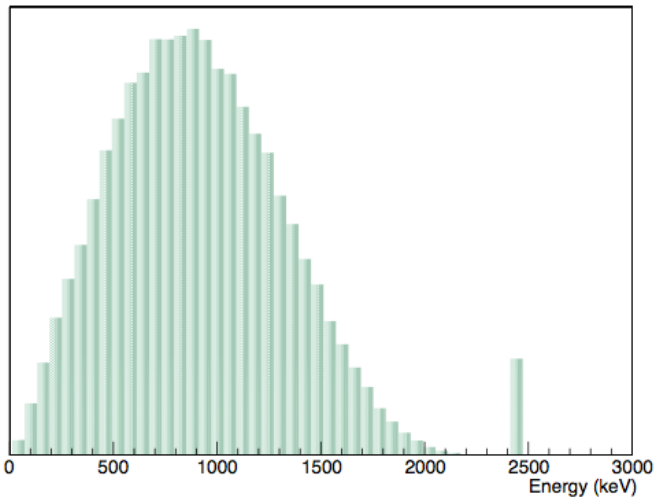

Figure 2.3: Sum of the kinetic energy distribution of the two emitted electrons in the double beta decay. The continuum spectra is from the ^{136}Xe double beta decay with neutrinos ($\beta\beta2\nu$) and the peak at the $Q_{\beta\beta}$, scaled to make it visible, from the neutrinoless mode ($\beta\beta0\nu$). Data from DECAY0 [71] and amplitude given in arbitrary units.

the finite energy resolution (ΔE) of any detector to measure the $\beta\beta0\nu$ peak, other processes occurring in the detector, such as the tail of the $\beta\beta2\nu$ mode, can fall in the region of energies around $Q_{\beta\beta}$ overwhelming the signal peak, that is becoming background. This makes the choice of energy measurement technique important for background rejection. In other words, the better the energy resolution the better the detector's sensitivity. Therefore, excellent energy resolution is crucial, because it increases the signal-to-noise ratio, but it is not enough by itself. In addition other extra handles such as identification of the decay daughter [72, 73, 74] or reconstruction of the signature pattern of the decay [75, 76, 77] could increase the signal-to-noise ratio.

Moreover, as in other rare event detectors, backgrounds of cosmogenic origin and natural radioactivity from materials are a problem, and thus underground operation and selection of radio pure materials to

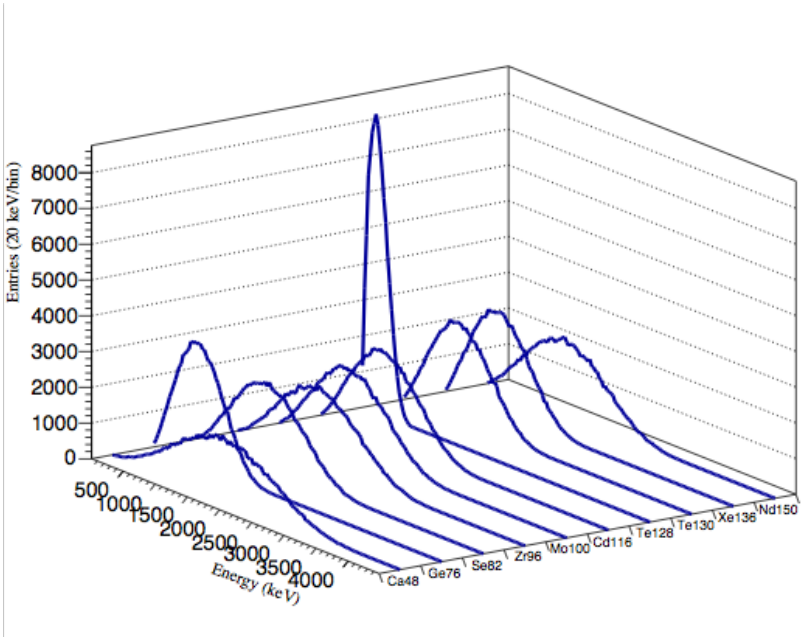

Figure 2.4: $\beta\beta2\nu$ spectra of different isotopes considered for $\beta\beta0\nu$ searches showing their Q-value. Same number of events and infinite resolution used for isotope comparison.

achieve the lowest background operation environment is essential [78].

Regarding the isotope selection for an experiment, those with higher Q-value would be preferred in order to avoid the low energy radioactive backgrounds (Figure 2.4) and benefit from larger phase-space factors ($G^{0\nu} \propto Q^5_{\beta\beta}$). It has to be taken into account the natural abundance of the $\beta\beta$ emitters and thus the cost of enrichment to increase the exposure. For this reason cost and scalability of detectors based on low abundance isotopes or expensive enrichment, could be an issue.

In the end the optimization of all the parameters should be the key. This relation can be summarized as follows :

$$T_{1/2} \propto a \cdot \epsilon \sqrt{\frac{M \cdot t}{\Delta E \cdot B}} \tag{2.11}$$

where ϵ is the detector efficiency, the product of the target mass (M) and data taking time (t) is taken as the exposure, ΔE is the energy

resolution and B the background rate. Phase space factors and nuclear matrix elements enter in the coefficient a [57].

2.4 Current generation experimental searches and near future techniques

In the following, we will briefly review the current status and near future prospects of the numerous projects searching for $\beta\beta0\nu$ decay grouped according to their detector technique. A summary of the best present results can be seen in Table 2.2 and current limits imposed on $m_{\beta\beta}$ in Figure 2.5. These results already demonstrate the need for larger-exposure upgrades, glimpsing the troubles for some techniques to scale up its searches. It seems that the move towards an unique experiment per technique or isotope due to exorbitant cost and budget constrains could be necessary. Therefore the isotope selection taking into account abundance, cost, enrichment, scalability, phase-space factor and Q value compared with backgrounds are, as said above, variables to evaluate reaching an equilibrium.

Independently of technique, until an unambiguous way of tagging the decay is developed, a common design criteria for all techniques is the usage of the most radiopure possible material as well as underground operation to avoid unnecessary backgrounds. One of the great things about most of the experiments described here is the idea of using the same material as source and detector medium so one can minimize the external components and avoid backgrounds introduced by adding different materials.

2.4.1 Bolometer detectors

When some crystals are cooled down to $\sim$ mK their heat capacity sinks and makes them sensitive to any interaction occurring inside producing a measurable temperature increase proportional to the energy deposited, fulfilling the general approach of all $\beta\beta0\nu$ detector, i.e. calorimetry. This technique is highly sensitive to small energy depositions, therefore makes it suitable also for other rare events searches such as dark matter.

Best present result for this technique applied to $\beta\beta$-decay searches are Cuoricino and CUORE-0 results [79, 68], the prototype and first phase of the CUORE experiment, respectively. The CUORE detector consists of 19 towers containing 52 TeO_2 crystals each, corresponding to a total mass of 204 kg of ^{130}Te, inside a cryostat able to cool down to $\sim$ 6mK [80]. It is surrounded by ancient lead and operated underground at Laboratori Nazionali del Gran Sasso (LNGS) in Italy, for background suppression. It aims to reach a sensitivity of $T^{0\nu}_{1/2}(^{130}\text{Te}) = 1.6 \times 10^{26}$ yr ($m_{\beta\beta} \sim 50$ meV) in 5 years of data taking with an expected background level of 0.01 counts/(keV·kg·y) in the signal region ($Q_{\beta\beta} = 2527.5$keV).

Using the same technique other experiments will search for $\beta\beta0\nu$ in other isotopes like ^{100}Mo or ^{82}Se. With the knowledge of current experiments in hand, they are focusing in extra handles for further background reduction. The AMoRE project deploys ^{100}Mo enriched $CaMoO_4$ crystals using as an extra handle the crystal scintillation light in addition to the phonon yield to discriminate alpha induced backgrounds [81], LUMINEU does the same with Li_2MoO_4 [82]. Also the LUCIFER/CUPID-0 demonstrator uses the β/γ vs α discrimination of light yield produced by a $Zn^{82}Se$ scintillating bolometer, aiming to reach a background level as low as 10^{-3} counts/(keV $\cdot$ kg $\cdot$ y) in the energy region of interest with the final CUPID detector [83, 84].

2.4.2 Scintillator detectors

Liquid scintillator detectors have been used for neutrino physics due to their well known performance and their prominent large mass. Some experiments have updated the detectors from oscillation experiments to $\beta\beta0\nu$ dedicated searches or as a multipurpose detector. Luminescent materials can absorb energy from the interacting particles, re-emitting light proportional to the deposited energy (scintillation).

KamLAND-Zen is reusing KamLAND detector at Kamioka (Japan). It deploys a 3.08-meter-diameter transparent nylon film balloon filled with 13 tons of ^{136}Xe-loaded liquid scintillator (Xe-LS), into an outer larger (13-meter-diameter) balloon filled with 1 kiloton of liquid scintillator. Surrounding the two concentric balloons, to detect scintillation

light, 1.325 17-inch and 554 20-inch photomultiplier tubes (PMTs) are mounted on a stainless-steel containment tank. This tank is surrounded by a 3.2-kton water-Cherenkov detector for cosmic-ray muon identification. It has been collecting data since 2011 reaching 1.4×10^{-4} counts/(keV $\cdot$ kg $\cdot$ y) and 9.9% FWHM energy resolution at ^{136}Xe $Q_{\beta\beta}$. The measurement of the $\beta\beta2\nu$ mode and the best limit imposed to the ^{136}Xe $\beta\beta0\nu$ mode by KamLAND-Zen are shown in Table 2.1 and Table 2.2 respectively [85, 86].

SNO+ was converted from SNO into a multipurpose detector including the $\beta\beta0\nu$ searches in ^{130}Te by replacing the heavy water by 780 tonnes of liquid scintillator and 9500 8-inch PMT readout. With a similar technique, the inner 12-meter-diameter acrylic vessel will be loaded with 0.5% Te (1333 kg of ^{130}Te). It aims to reach a sensitivity of $T^{0\nu}_{1/2}$ (^{130}Te) = 1.96 $\times$ 10^{26} yr in 5 years of data taking and an expected background level of 13.4 counts/year in ROI with 10.5% FWHM energy resolution [87].

Other scintillation detector seeking for $\beta\beta0\nu$ process in ^{48}Ca, but with solid state scintillator, is the CANDLES detector. It is currently operating 300 kg CaF_2 crystals ($\sim$ 0.4 kg of ^{48}Ca) immersed in liquid scintillator and surrounded by 62 photo-multiplier tubes (13-inch and 20-inch PMTs) mounted on 30 m^3 stainless steel water tank at the Kamioka underground observatory, Japan. Although ^{48}Ca has the highest $Q_{\beta\beta}$ value (4.3MeV) and the 7.0% resolution at $Q_{\beta\beta}$, the background is estimated to be 76 ± 9(stat.) events/year/96 crystals from MC simulation mainly due to (n, γ) backgrounds. Reducing this background it aims to increase its sensitivity up to $T^{0\nu}_{1/2} \sim 10^{23}$ yr after one year measurement [88].

2.4.3 Semiconductor detectors

GERDA searches for $\beta\beta0\nu$ in ^{76}Ge using high-purity germanium (HPGe) diodes detectors mounted in ultra-pure copper arrays and immersed in a cryogenic liquid argon bath at LNGS, Italy. It has been running from 2011 to 2013 (Phase-I) with 9 HPGe plus 5 BEGe (broad energy HPGe improved) giving 21.6 kg $\cdot$ yr total exposure and upgraded in 2015 (Phase-II) with 30 BEGe doubling the exposure. Phase-I achived

10^{-2} counts/(keV $\cdot$ kg $\cdot$ y) background events and a exposure-averaged energy resolution of 4.8 ± 0.2 keV (HPGe) and 3.2 ± 0.2 keV (BEGe) at $Q_{\beta\beta}$ (2039.00 keV). That is $0.1 - 0.2\%$ FWHM. No signal was observed and a lower limit for the half-life of neutrinoless double beta decay of ^{76}Ge, $T^{0\nu}_{1/2} > 2.1 \times 10^{25}$ yr (90 % C.L.) [89], was set. The background index goal for Phase-II is 10^{-3} counts/(keV $\cdot$ kg $\cdot$ y) aiming for a sensitivity increased by a factor of 10.

Using the same BEGe detectors technology, MAJORANA has focused on demonstrating the feasibility of a low background experiment for the tonne scale requirements operating the MAJORANA demonstrator at Sanford Underground Research Facility (SURF). This has been done through two separated ultra clean electroformed copper cryostat, produced and machined underground, housing 35 p-type point contact 88% enriched in ^{76}Ge at SURF (29.7 kg) and 15 kg ^{nat}Ge detectors. The whole assembly and operation has proceeded inside a clean room environment. With 3.03 kg $\cdot$ year exposure have set a limit of $T^{0\nu}_{1/2}$ (^{76}Ge) $> 3.7 \times 10^{24}$yr and reached 23^{+13}_{-10} cts/(ROI $\cdot$ t $\cdot$ y) in a 3.1 keV ROI [90, 78]. MAJORANA follow a more classical operation approach shielding the cryostat with copper and lead bricks. GERDA instead, uses instrumented liquid argon bath as a active veto system. Being the highest energy resolution technique, MAJORANA plans to collaborate with GERDA towards a next generation ^{76}Ge experiment [91].

For future searches, Cadmium Zinc Telluride (CdZnTe) semiconductor detectors operated at room temperature are used by COBRA. CdZnTe itself contains nine double beta decay candidates isotopes therefore the detector acts as its own source mass. The main isotopes in the search are ^{116}Cd , ^{106}Cd and ^{130}Te due to their high $Q_{\beta\beta}$-value. A demonstrator made of 64 detectors (216 kg/d exposure) run from 2011 to 2013 at LNGS (Italy) testing the performance and the background reduction. The construction of a first module made of nine detectors with a volume six times the demonstrator each, started in 2016. With the goal of 3.5% FWHM energy resolution, 10^{-3}counts/(keV $\cdot$ kg $\cdot$ y) to reach the desired half-life sensitivity of 2×10^{26}years for the neutrinoless double beta decay of ^{116}Cd [92, 93, 94].

2.4.4 Calorimeter plus tracker detector

As the general goal of all the other techniques, these calorimeters measure the energy deposited by the candidate event (as the previous) to ensure it is a $\beta\beta0\nu$ event. But unlike the other experimental approaches, NEMO exploits the separation of target ($\beta\beta$ emitter isotope) and the detector medium. It also give the versatility of changing the emitter keeping the same detector performance giving the possibility to measure different solid isotopes. To measure the event energy it uses plastic scintillator coupled to PMTs modules obtaining 14% FWHM energy resolution in NEMO-3 [76]. As an extra handle to suppress backgrounds, it uses Geiger-mode multi-wire drift-chamber cells for tracking under a magnetic field, allowing the particle identification. The source foil is set at the centre and the tracker (inner) and calorimeter (outer) are layered at both sides of the source, performing a module. The collaboration have run NEMO-3 demonstrator from 2003 to 2011 at Laboratoire Souterrain de Modane (LSM) measuring several isotopes (see Table 2.2) in a cylindrical shape detector configuration. Currently the first of 20 square shaped modules (6.2 m long, 4.1 m high and 2.1 m wide each module) of Super-NEMO is under construction with the ^{82}Se being the first source foil. The expected performance is $T^{0\nu}_{1/2}$ (^{82}Se) $\sim 10^{26}$ yr for 500 kg $\cdot$ yr exposure, with 4% FWHM energy resolution at 3 MeV and 5×10^{-5} counts/(keV $\cdot$ kg $\cdot$ y) arround $Q_{\beta\beta}$ [95].

2.4.5 Time projection chambers

The Time projection chamber (TPC) technology offers the possibility of measuring the scintillation and the ionization of particle interactions. Being the source and detector the same media gives compactness, scalability and could also give good energy resolution depending on the readout technique. In this sense, xenon as the only noble gas detection medium that has a $\beta\beta$-decaying isotope, ^{136}Xe, with a natural abundance of 9% that can be enriched by centrifugation at a reasonable cost, is a perfect candidate. In addition, xenon does not have any other long-lived radioactive isotopes, and being a noble gas, it can be easily purified. Its $Q_{\beta\beta}$-value is high enough (2458 keV) to be used in a $\beta\beta0\nu$ experiment. Both liquid state, using cryogenics, and gas state are used experimentally.

In the first case, 200 kg of liquid xenon (80.6% enriched in ^{136}Xe) is used by EXO in its cylindrical TPC (EXO-200) at the Waste Isolation Pilot Plant (WIPP), in New Mexico, USA. The symmetric chamber is divided in two regions by a central cathode, at both ends crossed wire planes collect the ionization charge and avalanche photo diodes (APDs) measure the scintillation light. The TPC is housed inside a copper vessel immersed in a cryostat ($\sim$ 167 K) and covered by 25 cm lead walls. EXO-200 has been running since 2011 and published the first experimental measurement of the ^{136}Xe $\beta\beta2\nu$ [96]. It also set a limit on the $\beta\beta0\nu$ of 1.1×10^{25} yr with 100 kg $\cdot$ yr of ^{136}Xe exposure, reaching 1.53% σ/E energy resolution at $Q_{\beta\beta}$ (that is 3% FWHM) and $1.7 \pm 0.2 \times 10^{-3}$ counts/(keV $\cdot$ kg $\cdot$ y) in the $\beta\beta0\nu \pm 2\sigma$ ROI [97].
It has also set the first limits in ^{134}Xe searches to $T^{2\nu}_{1/2} > 8.7 \times 10^{20}$ yr and $T^{0\nu}_{1/2} > 1.1 \times 10^{23}$ yr at 90% confidence leve [98]. The Collaboration has been working since the beginning in the laser tagging of the ^{136}Xe decay daughter technique, as a extra feature to unambiguously identify the $\beta\beta0\nu$ decay. Currently is leading its efforts to the multi-tone scale planing the design of nEXO to search for $\beta\beta0\nu$ beyond the inverted neutrino hierachy.

A high-pressure xenon gas (HPXe) TPC can provide both good energy resolution and event topological information for $\beta\beta0\nu$ searches. Double beta decay events have a distinctive topological signature in HPXe that can be used to reject backgrounds: a ionization track, of about 30 cm long at 10 bar, tortuous due to the multiple scattering, an with larger deposition *blobs* in both ends (see Figure 3.1). The Gotthard experiment [75], consisting in a small xenon TPC (5 kg) operated at 5 bars, proved the utility of this signature, achieving a background rate of about 0.01 counts/keV/kg/year. However, the detector suffered of a modest energy resolution, 6.6% FWHM at $Q_{\beta\beta}$, probably due to the the use of conventional avalanche amplification in a wire plane, and to the addition of methane (4%) to the xenon (in order to increase the drift velocity and to suppress diffusion), that quenched the primary signals. Measurements in other small HPXe systems [99, 100] have shown that optimal energy resolution, <0.5% FWHM at $Q_{\beta\beta}$, is possible using electroluminescence (EL) for the amplification of the signals:

the charges from primary ionization are accelerated by a moderate electric field (3-4 kV/cm/bar), producing a proportional emission of UV light with sub-poissonian fluctuations. This performance seems independent of the gas pressure below 50 bar [101]. NEXT follows up with this work taking advantage of these features.

In the following chapters, the performance of the NEXT technique as a suitable candidate showing the energy resolution, low background from radiopure material selection and topological extra features are shown (Chapter 3), as well as detection efficiency and exposure needed for $\beta\beta0\nu$ searches.

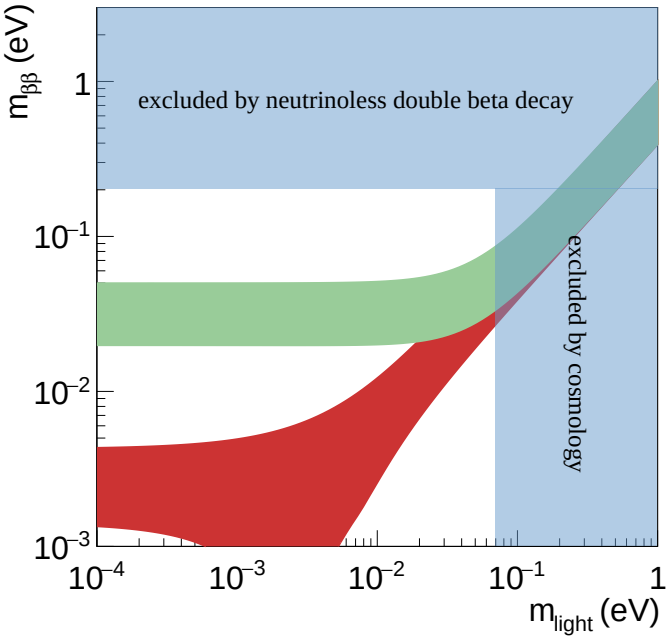

Figure 2.5: Effective neutrino Majorana mass, $m_{\beta\beta}$, as function of the lightest neutrino mass, m_{light} [57]. The green band corresponds to the inverted ordering ($m_{light} \equiv m_3$), whereas the red band corresponds to the normal ordering ($m_{light} \equiv m_1$), see Figure 1.2. The upper bound on the lightest neutrino mass comes from cosmological constrains and the bound on the effective Majorana mass from neutrinoless double beta decay constrains.

Isotope	$Q_{\beta\beta}$ (keV)	$T_{1/2}$ (y)	$\langle m_\nu \rangle$ (eV)	Experiment
^{48}Ca	4267.98	$> 5.8 \cdot 10^{22}$	$< 3.1 - 15.4$	CANDLES
^{76}Ge	2039.00	$> \mathbf{3.5 \cdot 10^{25}}$	$< \mathbf{0.18 - 0.48}$	GERDA-I
		$(> 5.2 \cdot 10^{25})$	$(< 0.15 - 0.39)$	+GERDA-II
^{82}Se	2997.9	$> 3.6 \cdot 10^{23}$	$< 1 - 2.4$	NEMO-3
^{96}Zr	3355.85	$> 9.2 \cdot 10^{21}$	$< 3.6 - 10.4$	NEMO-3
^{100}Mo	3034.40	$> 1.1 \cdot 10^{24}$	$< 0.33 - 0.62$	NEMO-3
^{116}Cd	2813.50	$> 1.9 \cdot 10^{23}$	$< 1 - 1.8$	AURORA
^{128}Te	866.6	$> 1.5 \cdot 10^{24}$	$2.3 - 4.6$	Geochem. exp.
^{130}Te	2527.52	$> 4 \cdot 10^{24}$	$< 0.26 - 0.97$	CUORICINO + CUORE0
^{136}Xe	2457.83	$> \mathbf{0.5 \cdot 10^{26}}$	$< \mathbf{0.09 - 0.24}$	KamLAND-Zen
		$(> 1.07 \cdot 10^{26})$	$(< 0.06 - 0.16)$	
^{150}Nd	3371.38	$> 2 \cdot 10^{22}$	$< 1.6 - 5.3$	NEMO-3

Table 2.2: Best present results on $0\nu\beta\beta$ decay from [102](limits at 90% C.L.).

"Let the future tell the truth and evaluate each one according to his work and accomplishments. The present is theirs; the future, for which I really worked, is mine."

Nikola Tesla

Chapter 3

High pressure xenon gas detectors for $\beta\beta0\nu$ searches

Designing a detector capable of identifying efficiently and unambiguously a signal as rare as neutrinoless double beta decay is a major experimental challenge. Consequently, many different techniques have been proposed, each one with its advantages and its drawbacks. This chapter is devoted to describe the technique selected by the NEXT project into detail. The general concept and how the detector works is discussed (§ 3.2), as well as the main features to be the best detection technique candidate for $\beta\beta0\nu$ searches. In the last part, the implementation of the different stages with its main goals is briefly described (§ 3.3).

3.1 The NEXT detector concept

The NEXT Collaboration proposed [103] a high pressure xenon gas electroluminescent time projection chamber (HPXe-EL TPC) detector with separated optimized functions (SOFT).

The source mass of the NEXT experiment is gas xenon enriched in the ^{136}Xe isotope. Xenon is a suitable detection medium that provides both scintillation and ionization signals. In its gaseous phase, xenon can provide high energy resolution, better than 0.5% at 2500 keV [104]. Two naturally-occurring isotopes of xenon can decay $\beta\beta$, ^{134}Xe ($Q_{\beta\beta} = 825$

keV) and ^{136}Xe ($Q_{\beta\beta} = 2458$ keV). The latter, having a higher Q-value, is preferred for neutrinoless double beta decay searches because the decay rate is proportional to $Q^5_{\beta\beta}$ and the radioactive backgrounds are less abundant at higher energies. The two-neutrino decay mode of ^{136}Xe is slow, $\sim 2.3 \times 10^{21}$ years [96, 85], and hence the experimental requirement for good energy resolution is less stringent than for other $\beta\beta$ sources. Also, xenon, unlike other $\beta\beta$ sources, has no long-lived radioactive isotopes that could become a background.

From Equation 2.11 it can be seen that the combination of energy resolution and background control is of the uppermost importance, to resolve the $\beta\beta0\nu$ events from the continuous $\beta\beta2\nu$ spectrum and from the radioactive backgrounds that can mimic the signal. In addition, the detection efficiency and the total mass that a technique can deploy need to be taken into account in the design of an experiment. Three main features have been optimized in NEXT with this purpose:

1. *Excellent energy resolution.* The low Fano factor of the gaseous phase results in an intrinsic resolution as good as 0.3% FWHM at 2.5 MeV [104]. The NEXT collaboration has measured the resolution attainable with HPXe prototypes using electroluminescence (EL) amplification. First measurements, using small prototypes [105, 106], yielded an extrapolated value of 0.4% FWHM at $Q_{\beta\beta}$. EL amplification provides linear gain with sub-Poissonian variance [107], allowing the exploitation of the small Fano factor of gaseous xenon. The calorimetry readout plane is fully devoted to exploit the energy resolution achievable using photomultiplier tubes for a precise energy measurement.

2. *Availability of a topological signature.* A HPXe detector offers the possibility to determine the complete topology of each event in 3-D. Background rejection factors of up to a factor 100 are possible exploiting the topology [108]. The $\beta\beta0\nu$ events leave a distinctive topological signature in gaseous xenon: an ionization track, about 30 cm long at 10 bar, tortuous due to multiple scattering, and with larger energy depositions at both ends (see Figure 3.1).
   The NEXT Collaboration has demonstrated the topology recon-

struction ability with prototypes [77]. The EL light generated at the anode is recorded in the photosensor plane right behind it and used for tracking. This separate readout is optimized for exploiting the track reconstruction with an optimal pitch of silicon photomultipliers to get the desirable spatial resolution. Requiring signal events to be strictly contained in the active volume of the chamber eliminates essentially all charged backgrounds entering the detector. Confined tracks generated by neutral particles, like high-energy gammas can be suppressed by pattern recognition.

3. *Scalability.* To fully explore the inverted-hierarchy region, tonnes of $\beta\beta$ source mass will be needed. Therefore, the scalability to large masses of the different experimental techniques (including both their technical feasibility and cost) has to be taken into account. The ^{136}Xe isotope constitutes 8.86% of all natural xenon, but the enrichment process is relatively simple and affordable compared to that for other $\beta\beta$ isotopes, thus making ^{136}Xe the most obvious candidate for a future multi-tonne experiment. In the NEXT concept, xenon is both source and detector providing higher efficiency than separated-source approach detectors. The NEXT concept design favors the scalability to large masses: doubling the dimensions of the detector (i.e. radius and length multiplied by two) increases the source (the volume) by a factor of 8, while the backgrounds, which typically scale with the detector surface, only increase by a factor of 4. The focus of this work, the NEW detector, is also demonstration of the scalability of some technical parts from NEXT–DEMO, mainly the electroluminescent generation.

As we have seen, some of the parameters (the energy resolution, for instance) depend on the experimental technique and cannot be improved at will. However, others are also determined by factors unrelated to the detection technique, therefore common to all experiments and then not specifically optimized in the NEXT concept. This is the case of the background rate, that may depend on the availability of radiopure materials or the depth of the underground laboratory, leaving more room for improvement. This goal has been addressed for first time in NEXT with the construction of the NEW detector by a through

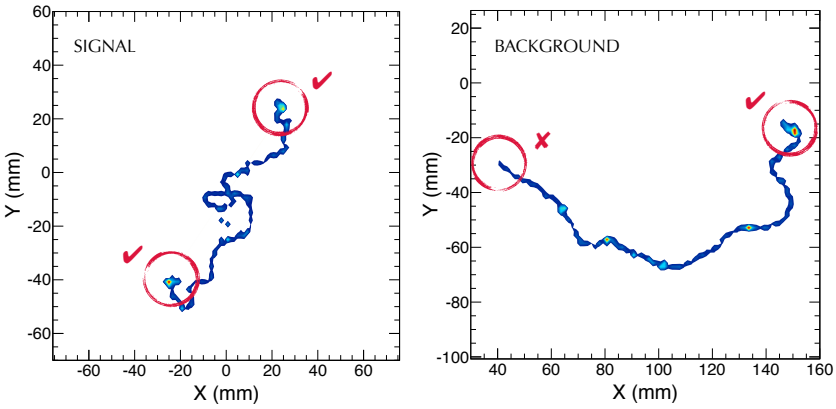

Figure 3.1: Monte Carlo simulation of signal ($\beta\beta0\nu$ decay of ^{136}Xe) and background (single electron of energy equal to the Q value of ^{136}Xe) events in gaseous xenon at 15 bar. The color scale codes the energy loss via ionization per path length. The ionization tracks left by signal events feature large energy deposits (or *blobs*) at both ends. Figure from [110].

campaign of material screening [109], the assessment of the background model with the NEW prototype (Chapter 5) and the underground operation at LSC. The predicted background rejection together with the selection efficiency for the signal estimate a background rate of about 5×10^{-4} counts/(keV·kg·y) for NEXT-100. With this background rate, the NEXT-100 detector will reach a sensitivity (at 90% CL) to the $\beta\beta0\nu$ decay half-life of 2.8×10^{25} years for an exposure of 100 kg $\cdot$ year, or 6.0×10^{25} years after running for 3 effective years. This corresponds to an upper limit on the Majorana neutrino mass of 80–160 meV [110].

3.2 The NEXT detection process

The basic principle of any particle detector is the transformation of the energy deposited in the detector mass by radiation into a measurable signal more adequate for human perception or electronic processing. Double beta decay experiments focus on the measurement of the energy released by the decay. A particle interacting in a detector (in the case

under study, the electrons released in the decay) transfers energy to the detector medium which can be released in different ways (depending on the medium) but preferably proportional to that energy. In the case of time projection chambers, either liquid or gas, the interacting particles can transfer their energy via *excitacion* or *ionization*. These processes release the energy emitting scintillation light by de-excitation (the former) or possible recombination (the latter) with characteristics time and energy [111].

The excitation energy in HPXe is manifested in the prompt emission of VUV ($\sim$ 178 nm) scintillation light, which we call primary scintillation (S1). This light is measured with the calorimetry readout plane providing the start-of-event time (t_0).

If the energy of the particle is high enough it can ionize the xenon atoms producing a set of free electrons and positive ions along its interaction path, called ionization track. The electron-ion pairs left behind by the interacting particle are, in our case, prevented from recombination by an electric field (0.3–0.5 kV/cm). This electric field makes the ionization electrons drift toward the TPC anode, where a second signal is produced.

To achieve optimal energy resolution, the ionization signal is amplified in NEXT using the electroluminescence (EL) of xenon. In contrast to gas avalanche multiplication detectors, the electroluminescence is a linear amplification process since the number of produced photons per electron is practically linear with the applied electric field in the range between 1 and 6 kV/cm/bar [112]. The implementation of EL in a TPC is done including an additional electric field region right after the drift volume. When the ionization electrons have drifted towards the anode, they enter in the EL region, defined by two highly-transparent conductive planes (Gate - Anode), with a more intense electric field (between 1 and 6 kV/cm/bar), there even more VUV photons are generated isotropically by electroluminescence. This amplified scintillation is called secondary scintillation (S2) and allows better measurement of the energy deposited by the event as well as the geometrical distribution (x,y) of the ionized electrons in the interaction path.

Therefore, both scintillation and ionization produce optical signals that are detected by a sparse array of photomultipliers (PMTs at the *energy plane*) located behind the cathode. The detection of the former

(S1) provides t_0, while the detection of the latter provides the energy via EL (S2). To be able to register the scintillation signal, the photo collection has to be optimized given the low intensity of the S1, the production of the S2 in the opposite side of the chamber and moreover, due to the low quantum detection efficiency to VUV light of the sensors. This is increased using a wave-length shifter (WLS) on top of the sensors that converts signal to adjust the response. This WLS is also used on the detector walls to increase the light collection via reflections (see Appendix 7).

The EL light (S2) is also detected a few millimeters away from production at the anode plane, by an array of multi-pixel photon counters (MPPCs at the *tracking plane*). Thanks to the high granularity of the array, a set of points can be connected giving two-dimensional reconstruction of the ionization tracks. The MPPC sensor response has also to be optimized using a WLS to make them sensitive to VUV. To ensure the electroluminescence is produced, not only the drift voltage to get the ionization electrons to the EL region has to be optimized, but also that the recombination do not occur (due to impurities in the media) continuously cleaning the gas.

In summary, the longitudinal coordinate is obtained from the arrival time of the signal to the tracking plane. Hence the TPC, with the combination of both readouts gives a full three-dimensional measurement of the trajectory and the energy deposition pattern of a charged particle (time projection chambers principle [113]). The description of the whole process is graphically explained in Figure 3.2 separated in two steps the scintillation (S1) and the electroluminiscence (S2).

3.3 The NEXT project

The goal of the NEXT project is the construction, commissioning and operation of the NEXT–100 detector, a 100 kg xenon gas TPC built with radiopure materials that will start taking low background data at the Laboratorio Subterráneo de Canfranc in the next few years. The experiment is organized as a collaboration involving about 60 physicists and engineers from different research institutes and universities in Spain, Portugal, USA, Colombia and Russia. The first phase of the

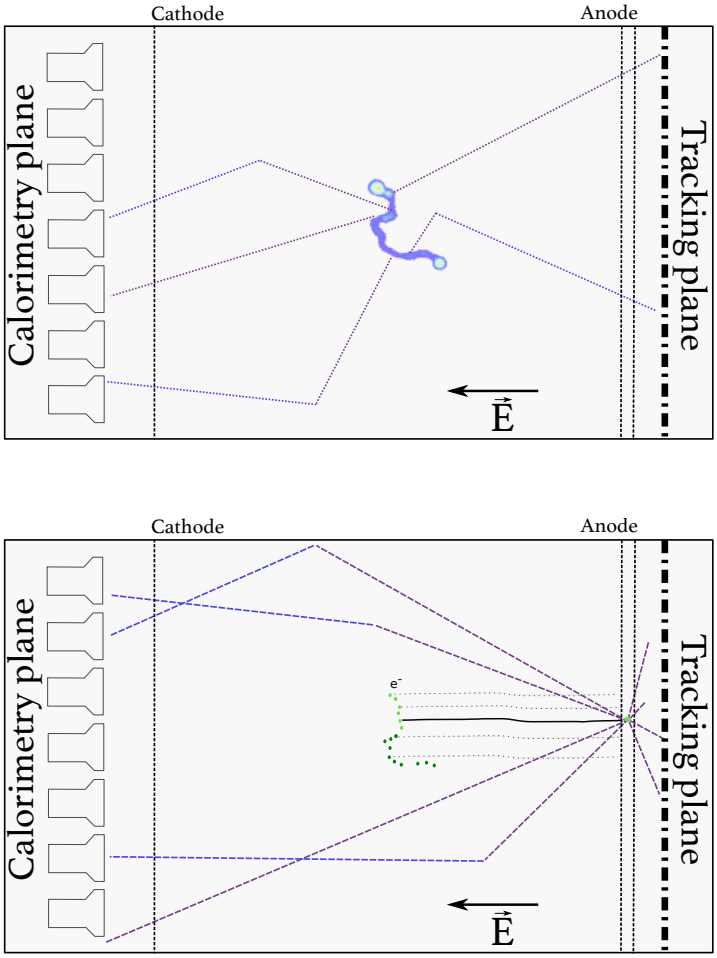

Figure 3.2: (Top panel) A ^{136}Xe nucleus decays emitting the two electrons and both excite the Xe producing primary scintillation light (S1) emission in VUV ($\sim$ 178 nm). The S1 signal is detected by the PMTs giving the start of event time. (Bottom panel) The two electrons create ionization charge in Xe ($\sim$ 25 eV to create one electron-ion pair [108]). The created electrons drift towards the anode with velocity $\sim$ 1 mm/μs in a $\sim$ 0.5 kV/cm electric filed. Secondary ionization light (S2) is produced between the gate and anode via the process of EL. The light produced is detected by SiPMs behind the anode used to reconstruct the event topology and in the PMTs behind the cathode used for the energy measurement.

project (2009–2014) was largely devoted to R&D with two medium-size prototypes, NEXT–DEMO and NEXT–DBDM, built with the dual aim of demonstrating the detector concept and gaining technical expertise to facilitate the design, construction and operation of a larger system. In a second phase (2014–2018), the Collaboration is operating underground the NEXT–NEW detector, a technology demonstrator that implements in a smaller scale (1:2) the design chosen for NEXT–100 using the same radio-pure materials and photosensors. The third phase of the project, NEXT–100, is planned to start in 2018.

3.3.1 Phase I : R&D

Some parts of the concept proposed in the *Letter of Intent* [103] were already studied (EL [105]), but most of the work was planned and simulated so a demonstrator of the technology was needed. This was done in different prototypes, focused on complementary objectives and the published results lead to a Technical Design Report (TDR [114]).

The first phase with the various R&D prototypes, is described here to understand the key question on probing the technology of any experiments.

The NEXT-DBDM (DoubleBeta DarkMatter) detector was an electroluminescent TPC operated at LBNL (USA), equipped with a compact array of 19 Hamamatsu R7378A PMTs 1-inch size, sensitive to VUV light and operable at pressures up to 17 bar. The fiducial volume, a hexagonal prism, was 8 cm long with 17 cm diameter. The detector vessel, a 10 L stainless-steel container, could hold about 1 kg of xenon gas at 15 bar. The main goal of this prototype was to perform detailed energy resolution studies (see Figure 3.3), showing an extrapolated 0.5% FWHM energy resolution at $Q_{\beta\beta}$ assuming to follow $1/\sqrt{\mathrm{E}}$ dependence [106].

The NEXT-DEMO detector, operated at IFIC, was equipped with an energy plane made of 19 Hamamatsu R7378A and a tracking plane made of ~ 300 1-mm^2, Hamamatsu MPPCs. The stainless-steel pressure vessel, 60 cm long and 30 cm diameter, could withstand 15 bar. The main goal of the prototype was the demonstration of the detector concept to be used in NEXT-100. More specifically: to demonstrate track

reconstruction and the performance of MPPCs (see Figure 3.3) [115, 77]; to study the energy resolution at this scale [116]; to test long drift lengths and high voltages (up to 50 kV in the cathode and 25 kV in the anode) [117]; to understand gas recirculation in a large volume, including operation stability and robustness against leaks [117]; to understand the transmittance of the light tube, with and without wavelength shifter (see Figure 5) [116].

The contribution to the last is also described in this thesis, although being a development done in the earliest PhD stage it was separated from the main dissertation (the NEW detector stage) and described in the appendix (Appendix 7) to not interrupt the unifying thread.

3.3.2 Phase II : underground operation of NEW

The NEW (NEXT-WHITE)[1] detector is a step forward in the validation of the roadmap to build the NEXT-100 detector. It is a 1:2 scaled-down version of NEXT-100 detector, using already the facilities, platform, gas system and external shielding to be used for NEXT-100. It implements about 10 kg of xenon mass at 15 bar and readout planes of $\sim 20\%$ the size of the final ones using the same sensors planned for NEXT-100. The construction and commissioning also exercise the assembly procedure, safety and emergency standards, as well as several new technical solutions not tested in the smaller R&D devices such as cylindrical field cage with a quartz anode plate defining the time projection chamber (TPC), pressure isolated PMT's, MPPC boards, readout electronics, cryorecovery system and slow controls.
In addition to these technological goals, NEW has several physics objectives:

- Refinement of detector calibration techniques for NEXT-100.
- The DEMO and DBDM prototypes were too small to contain tracks of the energies of interest for $\beta\beta0\nu$ searches in ^{136}Xe. Therefore, NEW data will be extremely useful for the optimization of the reconstruction and pattern-recognition algorithms at those

[1] Named after our late collaborator Prof. James T. White.

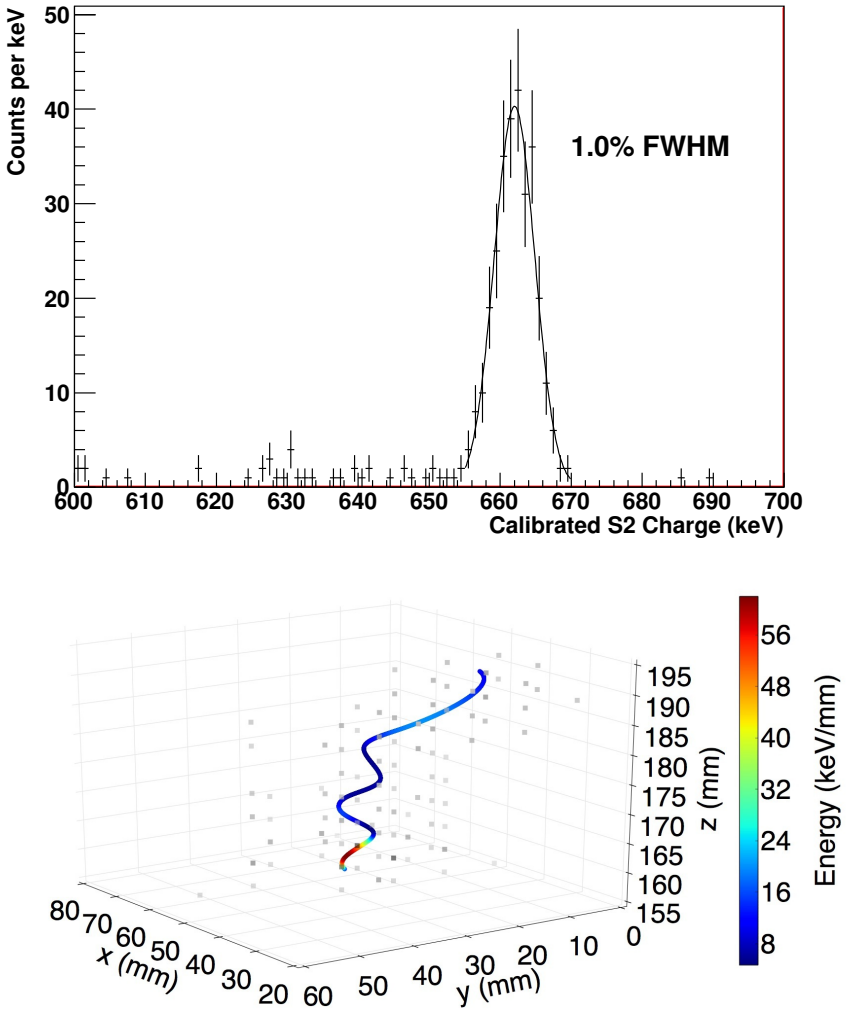

Figure 3.3: Best results achieved with the prototypes: energy resolution at 662 keV from ^{137}Cs in DBDM detector (top) [106], ^{137}Cs generated electron track in DEMO (bottom) [116].

energies. In particular, NEW will allow the accurate characterization of the 2-electron tracks, which is the trademark of the NEXT technology.

- The background rate predicted for the NEXT-100 is estimated using detector simulations and the data from material screening. NEW deploys the same materials chosen for NEXT-100, thus allowing a stringent test of the background model. Understanding the effects of the four types of backgrounds genesis is of uppermost importance.

- Depending on the actual background level and the length of the data-taking period with enriched xenon, it may be possible to measure the half-life of the two-neutrino decay mode of ^{136}Xe.

Three of these four objectives: calibration (§ 6.1, § 6.2), background model (Chapter 5) and half-life measurement of the $\beta\beta2\nu$, are discussed in this thesis. The reconstruction and pattern recognition —the fourth one— can be found in [77, 118, 119].

3.3.3 Phase III : search for $\beta\beta0\nu$ with NEXT-100

The search for the $\beta\beta0\nu$ decay of ^{136}Xe will be done with the use of a 100-kg xenon gas TPC with electroluminescent amplification and optical readouts.

A schematic description of the NEXT-100 detector design can be seen in Figure 3.4. The active volume of the detector is a cylinder of approximately 1.15 m^3 that can hold about 100 kg of xenon gas at 15 bar. It is surrounded by a series of copper rings for electric-field shaping that are fixed to the inner surface of an open-ended high-density polyethylene (HDPE) cylindric shell, 2.5 cm thick, 148 cm long and 107.5 cm in diameter, that provides structural stiffness and electric insulation. The rings are covered by polytetrafluoroethylene (PTFE) tiles coated with tetraphenyl-butadiene (TPB) to shift the xenon VUV light to the blue region (around 440 nm) so as to improve the light collection efficiency. One of the ends of the HDPE cylinder is closed by a fused-silica window 1 cm thick. This window functions as the TPC anode thanks to a transparent, conductive, wavelength-shifting coating of indium tin oxide (ITO) and TPB. The two other

electrodes of the TPC, EL gate and cathode, are positioned 0.5 cm and 106.5 cm away from the anode, respectively. They are built with highly transparent stainless steel wire mesh stretched over circular frames. The electrodes will be set at voltages such that a moderate electric field of 0.3–0.5 kV cm^{-1} bar^{-1} is established in the drift region between cathode and gate, and another field of higher intensity, 2–3 kV cm^{-1} bar^{-1}, is created in the EL gap, between gate and anode, for the amplification of the ionization signal. The high voltage is supplied to the electrodes via radiopure, custom-made feed-throughs [114].

The energy plane of NEXT-100 will be composed of 60 Hamamatsu R11410-10 photomultiplier tubes located behind the cathode of the TPC and covering approximately 30% of its area. This coverage is a compromise between the need to collect as much light as possible for a robust measurement of the energy and t_0, and the need to minimize the number of sensors to reduce cost, technical complexity and radioactivity. The R11410-10 is a 3-in PMT specially developed for low-background operation [120]. It is equipped with a synthetic silica window and a photocathode made of low temperature bialkali with quantum efficiency above 30% for the emission wavelengths of xenon and TPB [120]. Pressure-resistance tests run by the manufacturer showed that the R11410-10 cannot withstand pressures above 6 atmospheres [120]. Therefore, in NEXT-100 they will be sealed into individual pressure-resistant, vacuum-tight copper enclosures closed with sapphire windows 5 mm thick. The PMTs are optically coupled to the windows using an optical gel with a refractive index intermediate between those of fused silica and sapphire. The external face of the enclosure windows is coated with TPB. The enclosures are all connected via vacuum-tight tubing conduits to a central manifold and maintained at vacuum. The PMT cables route through the conduits and the central manifold to a feedthrough in the pressure vessel nozzle.

The tracking function in NEXT-100 will be provided by an array of 7168 SiPMs regularly positioned at a pitch of 1 cm and located behind the fused-silica window that closes the EL gap. The SiPMs, manufactured by SensL, have an active area of 1 mm^2, sensitive cells of 50 μm size and high photon detection efficiency in the blue region (about 40% at 440 nm). They are very cost-effective and their radioactivity is very low, given their composition and small mass. The SiPMs will be

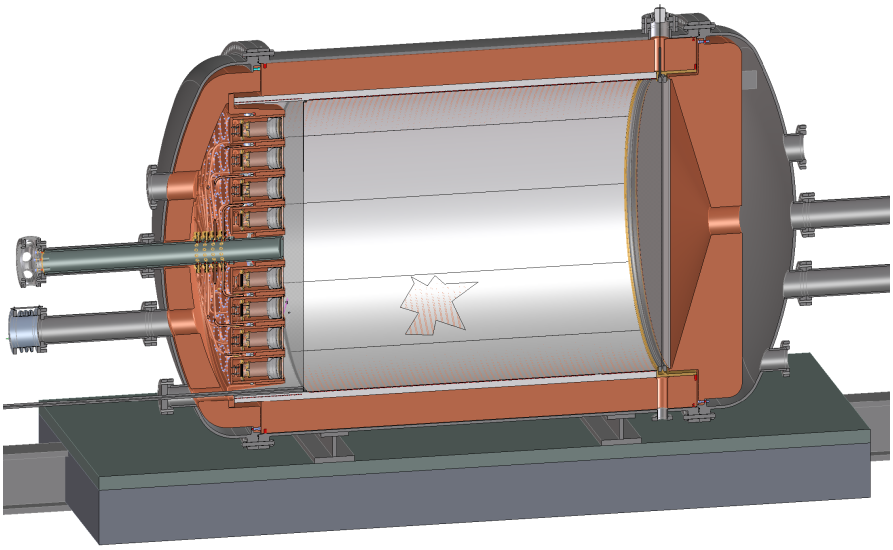

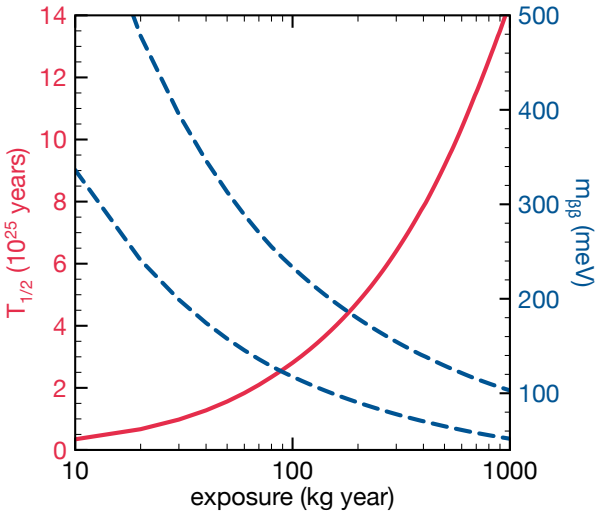

Figure 3.4: Cross section of the NEXT-100 design scheme showing the vessel, the copper shielding, the field cage and both readout planes (top panel) [114]. Projected sensitivity to the $\beta\beta0\nu$ half-life (red curve) and to the Majorana mass (dashed blue lines for the highest and lowest nuclear matrix elements) for the NEXT-100 detector (bottom panel) [110].

mounted on flexible circuit boards made of Kapton and copper, each one with 64 sensors arranged as an 8×8 matrix. The boards have long tails that carry the signals through zigzagging slits —so as to avoid a straight path for external gammas— made in the copper plates that shield the active volume. The tails are connected to flat shielded cables that extract the signals from the vessel via large custom-made feed-throughs [114].

The sensor planes and the electric-field cage are contained within a stainless-steel pressure vessel that consists of a cylindrical central shell of 160 cm length, 136 cm inner diameter and 1 cm wall thickness, and two identical torispherical heads of 35 cm height, 136 cm inner diameter and 1 cm wall thickness. It has been fabricated with stainless steel Type 316Ti (acquired from Nironit) due to its low levels of natural radioactive contaminants. Designed almost entirely by the Collaboration following the ASME pressure vessel code, the vessel has been built by a specialized company based in Madrid. The field cage is surrounded by a set of 12-cm thick copper bars parallel to the TPC symmetry axis, and both sensor planes are mounted to copper plates of 12 cm thickness attached to internal flanges of the vessel heads. The active volume of the detector is, therefore, shielded from external radiation by at least 12 cm of copper in all directions. The vessel sits on top of an anti-seismic pedestal and inside of a 20-cm thick lead shield made of staggered lead bricks held by a stainless-steel frame.

The goal of the NEXT-100 stage is to perform the first real search for the $\beta\beta0\nu$ in ^{136}Xe with the HPXe-EL TPC technology, reaching the claimed low background rate of 4×10^{-4} counts/(keV $\cdot$ kg $\cdot$ y) in the ROI and at least set a limit to the half-life in three years run (see Figure 3.4) [110]. Furthermore, we want to demonstrate the scalability of the technology to large masses.

3.3.4 Phase IV : future tonne scale plans

As the current experimental searches indicate that the current mass deployed (O 100 kg) are finishing without evidence of $\beta\beta0\nu$events, a scale up to fully cover the inverted hierarchy mass scale seems to be needed. In addition some neutrino oscillation studies favor the normal

hierarchy [121] implying a multi-tonne scale mass experiment to reach sensitivities down to few eV.

The NEXT concept could be extrapolated to this scale without any obvious drawback using the same scheme. The collaboration is also studying possible arrangements of the detector to further improve the features of the detector including its background rate reduction from the sensors. This could be done with a reasonable cost for the scope, constructing a symmetric TPC able to drift the charges through the chamber towards two instrumented endcaps with mixed functions (energy measurement and tracking).

"The road to the City of Emeralds
is paved with yellow brick," said
the Witch, "so you cannot miss it."

L. Frank Baum
"The Wonderful Wizard of Oz"

Chapter 4

The NEW detector

As has been discussed in the previous chapter, the current phase of the NEXT project consists in the implementation of the detector concept demonstrated in early prototypes in a somewhat larger scale and in the more challenging conditions of low-background, underground operation. The NEW detector uses the same installations that will be used for NEXT–100 and all detector components have been screened for radiopurity and were cleaned and assembled under clean room conditions. In this way NEW will act as a dress rehearsal for the main experiment. The NEW detector has three main goals:

1. **Technology**: it will validate the technological solutions adopted for NEXT-100, described in detail in this chapter.

2. **Radiopurity**: NEW implies a step forward in the implementation of a radiopure detector. The NEXT background model is currently based on a sophisticated Monte Carlo simulation of all expected background sources in each element of the detector. NEW will allow the validation of this background model (Chapter 5) with data, since the detector will be radiopure and will use the same solutions chosen for NEXT-100. Furthermore, it will allow the identification and correction of any possible backgrounds, which can only be identified with operating experience.

3. **Physics**: It will demonstrate reconstruction, energy resolution and single/double electron discrimination at $Q_{\beta\beta}$ energies, as well

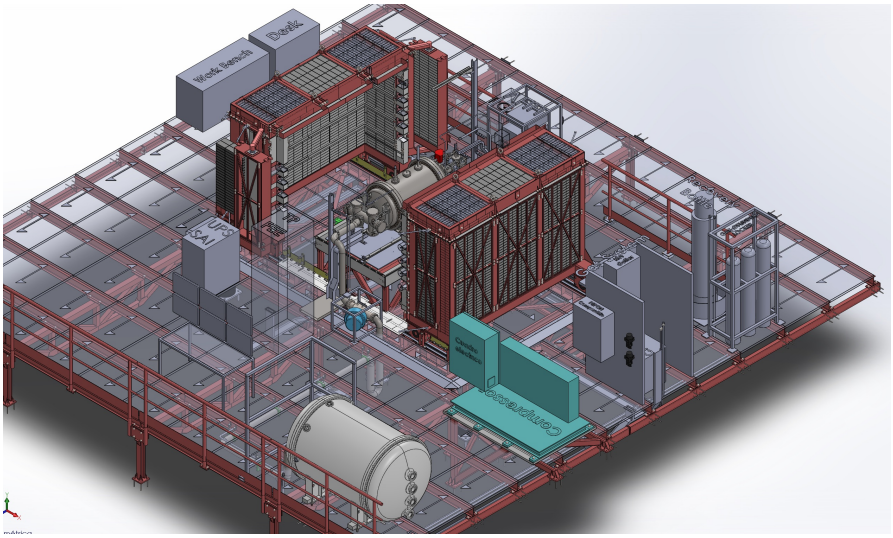

Figure 4.1: Schematic of the NEW detector and its ancillary systems at the work platform in Hall A of the LSC.

as making a first measurement of the half-life of $\beta\beta2\nu$. Some of the physics goals are discussed in Chapter 6, while other operational objectives not treated in this work are:

- Calibration of the detector with high energy sources, allowing a precise study of the evolution of the resolution with the energy, and eventually demonstrating a resolution as close to 0.5% FWHM at $Q_{\beta\beta}$ as possible.
- Measurement of the resolution near $Q_{\beta\beta}$ (with a thorium source, that provides 2.6 MeV gammas).
- Reconstruction of the spectrum of $\beta\beta2\nu$. Those events are topologically identical to signal events ($\beta\beta0\nu$) and can be used to demonstrate with data the power of the topological signature unique to NEXT.

This chapter is devoted to a detailed description of all the subsystems organization for the commissioning of NEW, from the innermost components to the external ones.

4.1 The electroluminescent TPC

One of the key technological challenges to be solved with NEW is the large EL electric field cage, because of its scale up in size. The NEXT-DEMO field cage had a diameter of 24 cm (although the 10 cm side teflon panels made an hexagon that set a 16 cm inscribed diameter light tube) and a length of 40 cm, while the field cage of NEXT-100 will have a diameter of 1 meter and a length of 1.2 meter. Building an intermediate field cage (1:2) makes easier the extrapolation to the final apparatus, testing some changes in the approach.

The main body of the field cage is a high-density polyethylene (HDPE) cylindrical shell of 49 cm external diameter that provides electric insulation from the vessel, at the same time as it provides structural support to other components of the field cage. Three regions are defined inside the field cage body: the buffer region, the drift region and the EL region.
The HDPE in the buffer region (11.2 cm length, defined from the PMTs to the cathode) is an inwardly grooved surface of 45.5 cm internal diameter (eighteen 3 mm-spaced 6.5 mm-high edges). This shape downgrades uniformly the high voltage of the cathode to zero, protecting the PMTs.
Inside the cylinder, between the buffer and the drift region, a bigger groove is machined to host the cathode. There is a hole at the top of this groove to allow passage of the high voltage feedthrough.
In the drift region (51.1 cm length, defined between the cathode and the gate) the HDPE is lined with ultra pure [109] copper strips which are connected with low background 10 GOhm resistors (Figure 4.2) to degrade the high voltage. This setup enables an homogeneous and uniform moderate electric field (300–600 V/cm) inside the active volume of the NEW detector. Two wire meshes, cathode and gate, define the active volume of NEW.
At the end of the HDPE barrel the external diameter is downsized to fit in the frame that hold the gate, which over cover the field cage body.

The cathode consist in a 12 mm stainless-steel ring frame (22.6 cm external diameter and 15.8 mm length) stretch vertically aligned 150 μm diameter stainless-steel wire, becoming the cathode of the TPC. The wires are spaced 1 cm pitch, thus provide a 98.5% open area mesh.

At the top of the ring, the cathode high voltage feedthrough (HVFT) point contact the mesh keeping it at the set cathode voltage (up to 50 kV).

The EL region is defined by the stainless steel mesh of the gate (similar design to the cathode) and the anode. The NEW EL region was designed so that the gate could hold up to 20 kV. In order to avoid issues related to having two large meshes close to each other with a large potential difference between them the NEW anode had to use a very different design to that used in the prototypes. Therefore, the anode is a fused-silica (52 cm diameter) rigid plate, coated with ITO to make its surface resistive and grounded (connected to the vessel). The anode is also coated with the wave length shifter (WLS) tetraphenyl butadiene (TPB) to convert the VUV light to blue light, matching the SiPM optimum response as well as increasing the transparency of the plate (VUV photons are filtered by fused-silica).
The gate and the anode plate are supported by a HDPE frame with eight gaps that provide insulation and allows the gas flow. It is kept in place by spring pressure on the tracking plane.

Up to 50 kV have to be brought into the vessel to charge the cathode and gate. Achieving this in a stable and pressure tight way was one of the main design challenges for the experiment. The high voltage feedthroughs are made out of a conductive rod and a custom made HDPE insulator manufactured by external companies according to NEXT specifications. The two pieces were then combined using cryofitting in house. The design can be seen in figure Figure 4.3.

A PTFE cylinder lines the inside of the drift region field cage body to increase reflectivity creating the the light tube. Light collection efficiency is further improved by coating the inner edge with TPB (see more in Appendix 7).

4.2 The calorimetry readout

It has been demonstrated that excellent energy resolution can be achieved using electroluminescent TPCs with PMT read-out [117, 106]. In order to measure the scalable background for NEXT-100, NEW had to be built with the same components. The selection of 3-inch R11410-10 Hamamatsu PMTs [122, 120] on account of its radiopurity

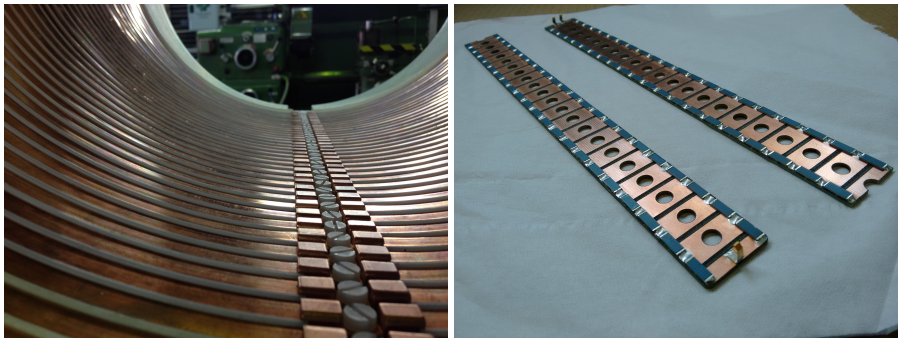

Figure 4.2: Copper rings (left) and resistor chain (right) of the field cage.

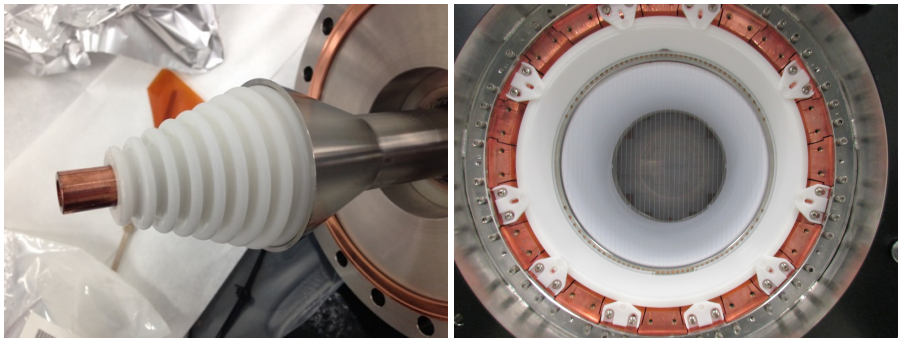

Figure 4.3: Close view of the high voltage feedthrough (left) and the field cage assembled (rigth).

was done already for NEXT-100.

As the PMTs do not withstand pressure it is not possible to operate inside the gas volume. Therefore two separated volumes have to be created with the ability of letting the PMTs see the active volume. The vacuum volume is created between the vessel endcap and the copper shielding carrier plate. The PMTs are optically linked to the active volume via sapphire windows which were brazed to copper surrounds which are sealed to the copper plate using helicoflex gaskets.The sapphire windows are coated with TPB to match to the maximum quantum efficiency of the PMT as well to dodge the poor transparency of sapphire to VUV light. PMTs are coupled with optical gel (NyoGel OCK-451), to match refraction indexes, to the sapphire window and held in place by a plastic brace and spring. This is replicated for 12 PMTs at the energy plane arranged in two rings, 3 PMTs in a central ring and 9 PMTs in the outer ring, leading to a 35% photocathode coverage.

The PMT plane is placed $\sim$ 12 cm behind the cathode mesh giving enough space to downgrade the electric field, ensuring the buffer region to be below the EL threshold and protecting the PMT themselves from the high voltage.

The electronic bases (Kapton®circuit board) are pinned behind the PMT with heat dissipators connected to the copper shield. Shielded twisted pair cable soldered to the base drive out the signal and powers high voltage to the PMTs through the endcap using 2 pins custom made HV feedthroughs.

4.3 The tracking readout

In order to take advantage of event topology to discriminate signal and background events an array of sensors with sufficiently high granularity must be available.

The the NEXT prototypes, especially DEMO [123, 124], demonstrated the reliability of multi pixel photon counters (MPPCs) to achieve track reconstruction. In particular, silicon photomultipliers (SiPMs) were used due to several factors: high photon detection efficiency to the TPB re-emission wavelength ($\sim$ 430 nm), low dark count rate and, especially due to the amount of sensor necessary, their radiopu-

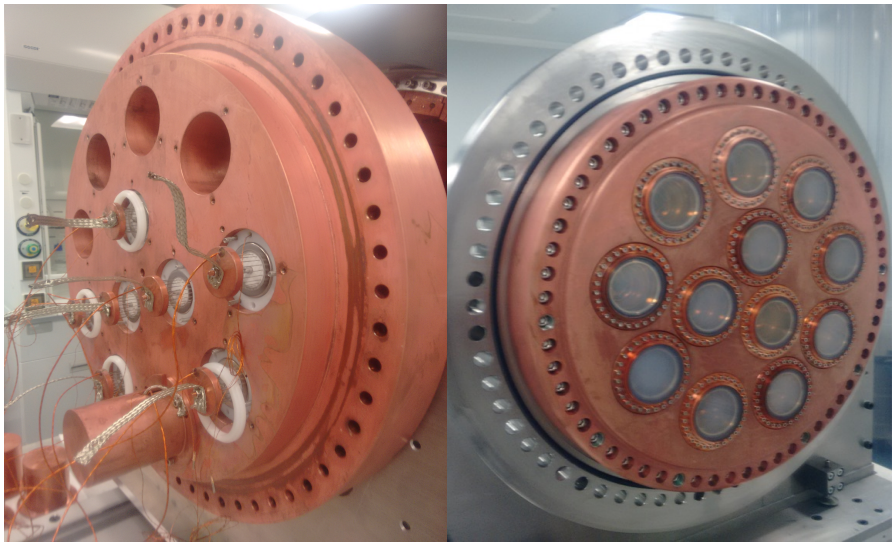

Figure 4.4: (Left) Electronic bases connected to the PMTs and heat dissipators connected to the copper shielding plate. (Right) Energy plane of NEW made of 12 PMTs behind sapphire windows attached to the copper shielding plate.

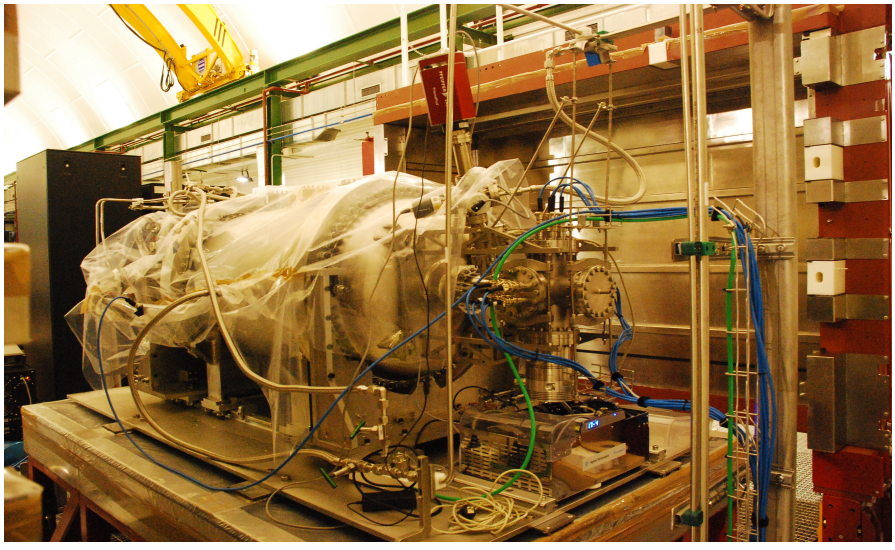

Figure 4.5: NEW detector assembled showing at the forefront the energy plane feedthrough and the turbo–molecular vacuum pump.

rity [114]. The latter was the driver to change from the Hamamatsu S10362-11-050P [122] SiPMs used in DEMO to the SensL MicroFC-10035-SMT-GP (1×1 mm^2) [125] SiPMs used in NEW. This result in a significant reduction of the background noise contribution of a crucial device in NEXT, otherwise not affordable for the NEXT goals (see Chapter 5).

The density of the SiPM array is also a compromise between the minimum distance effectively useful and the maximum pitch to still have connectivity between reconstructed points. Regarding the former, the transverse charge diffusion in pure xenon at electric field strengths around 0.5 kV/cm is about 1 mm/$\sqrt{\text{cm}}$, therefore it is not worthwhile to use a pitch smaller than 1 cm [114]. On the other hand, larger pitch is also preferable for radioactive budget and cost issues but for the NEW size, 1 cm pitch is affordable.

The SiPMs have to be hold and connected to the electronics circuitry and individual biasing for each sensor is not practical due to the amount of channels and cabling space. For this reason 64 SiPMs are mounted in groups on dice boards (DB) sharing the same bias voltage. Due to the Geiger mode operation of the SiPMs a small variation in the bias voltage induces a large variation in the gain. Therefore, the grouping of SiPMs to reduce the dispersion inside the same DB arranges them in similar gain DBs after the automatized characterization of individual SiPMs [126]. The calibration of the sensor is done once all the SiPMs are placed at its final position in the detectors.

The main upgrade that has been implemented from the prototype phase in NEW is the Kapton® dice boards (KDB). Now the substrate on which the SiPMs are soldered is made of three Kapton® isolating foils with two copper printed traces in between (broadside coupled traces design for differential signal output). The traces are 100 μm width with 0.5 mm pitch, which is a compromise solution for crosstalk, size and trace resistance. This makes a planar flexible circuit with some advantages [127, 128]:

- It allows the soldering of the SiPMs on the pads in an oven without peeling off the printed circuits, making automation of the soldering of the 1792 SiPMs of NEW possible, which will be even more relevant for the up to 7200 channels necessary for

NEXT-100. The DICE boards also incorporate a blue LED and temperature sensor (Figure 4.6).

- It reduces significantly the amount of adhesive used to fabricate the circuit, consequently its background contribution.
- The printed flexible circuit can be bent so the long KDB tail ($\sim$ 40 cm) can displace the SiPM connectors behind the copper plate to shield its radioactive contribution (Figure 4.8 left).
- This design has also eliminated capacitors and resistors in the board with a gated-integrator approach, reducing their contribution to the background budget.

To increase the light collected by the PMTs, a reflective teflon mask is fitted on top of the KDB reflecting the photons that do not get to the SiPMs without blocking those that do arrive (see Figure 4.7). The masks, as well as the KDBs, overcover the fiducial region to limit dead regions. All the KDBs are screwed to a copper supporting frame (can be seen in Figure 4.7), spring-loaded to align with the light tube, directly behind the quartz plate, minimizing distance between the sensors and the production region of the light. The copper frame is held by the 12 cm copper plate on the tracking plane side which is in turn held by four sliding bolts to the vessel endcap.

Once the KDB built-in tail passes the signal through the copper shielding plate, the connections are hidden (Figure 4.8, left), therefore commercial connectors (FX11LA-Hirose) and flat flexible cables (FFC) can be used with the only concern on how to drive the signal (bias voltage) out (in). High-density custom made, FR4-multilayer-PCB, feedthroughs have been produced and tested showing good results, avoiding the usage of ceramic feedthroughs. A total of five feedthroughs are used to connect the KDB to the external cables (Figure 4.8, right). Due to the amount of lines, three lines (bias, signal and guard) per SiPM channel plus temperature sensors and LED, commercial solutions were difficult to find. Therefore, each KDB corresponding cable is split into four FFC just at the output of the feedthrough, using a Kapton adapter board with four DF9-Hirose connectors (can be seen in Figure 4.8, right). To further reduce the possible noise coupled to

Figure 4.6: (Left) SiPMs, LED and NTC soldered onto the KDB and end-tail connector of the KDB (right) .

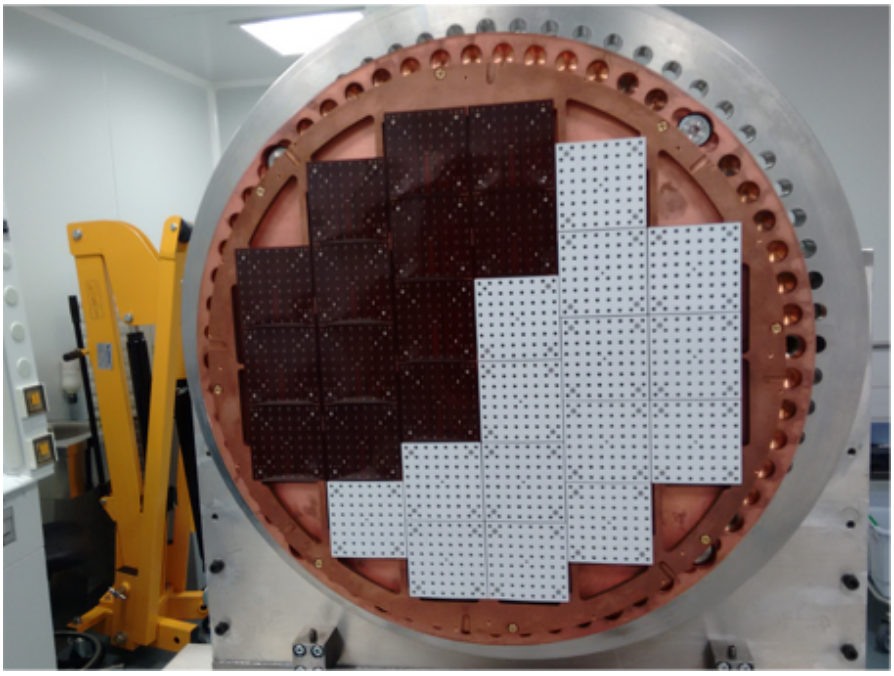

Figure 4.7: The NEW tracking plane made of 28 custom designed Kapton Dice Boards (KDB) with 64 ($1 \times 1\text{mm}^2$ SensL) SiPMs each, providing a dense array of 1 cm pitch for topological reconstruction. Half of the KDB was already covered with reflective teflon masks.

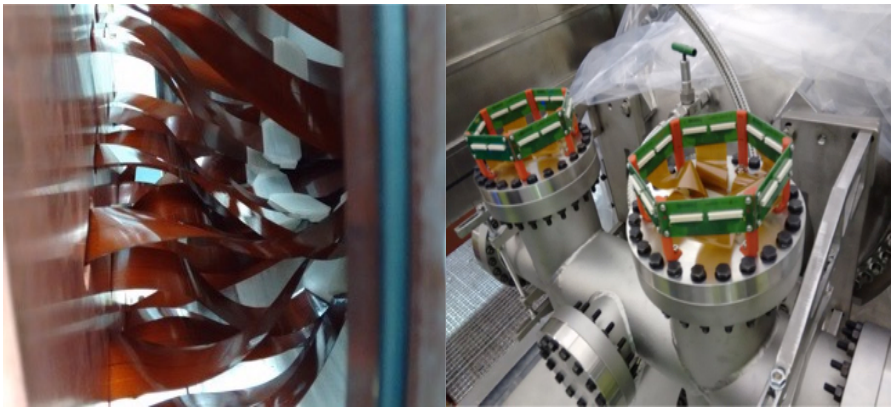

Figure 4.8: (Left) KDB end-tail connected through the copper shielding plate to the FFC towards the FR4 feedthroughs and adapter boards (right).

the cable, as the electronics have to be placed as close as possible but outside the shielding for radiopurity concerns, the external cables are wrapped in a mesh connected to the front-end ground [127].

It is also remarkable the in-house design and production of the SiPM power supplies (see Figure 4.10). These are programmable, multichannel power supplies with a temperature auto-compensation voltage loop and Ethernet interface for remote control [129]. The device produced provides gain stability for the SiPMs in the NEW detector of 0.5% in the operation range, with output voltage stability better than 2 mV.

4.4 The pressure vessel

The NEW pressure vessel (NPV) was manufactured with the same Ti-Stainless steel alloy selected for the NEXT-100 detector with an ASME pressure vessel certification.

The NPV was fabricated in three parts: a main cylindrical vessel and two symmetric torispherical heads. The dimensions of the NPV are intermediate between NEXT-DEMO and NEXT-100. The cylindrical central section of the vessel has an internal diameter of 64 cm, a length

of 950 cm and 2.4 cm thickness of steel. It includes three upper nozzles (CF60) —the central for calibration and the other two to host the high voltage feedthroughs— as well as two lateral nozzles (CF30), one for calibration and the other as gas output.
The two identical endcaps, of 1.26 cm wall thickness and 30 cm depth —including the nozzle (CF100)— close the central section bolting the flanges with an O-ring junction for tightness. They also have an extra gas nozzle each, for pumping the gas inside the vessel in the tracking plane side endcap and in the energy plane side to keep the volume created at vacuum or in a clean atmosphere (during commissioning the volume is filled with just over a bar of nitrogen). The CF nipples are all sealed using copper gaskets and all junctions have sniffer ports to test the seal tightness. The NPV can hold pressures of up to 20 bar CE certification.

Figure 4.9 shows the vessel during its first assembly in its horizontal operational position.

Following the *matrioska* concept, the radioactivity coming from the vessel is attenuated by an inner ultra pure copper shield (ICS). The ICS is also divided in three sections. 6 cm copper bars surround the field cage all along the central section of the vessel in the barrel section. A special shape to give stiffness and optimize the spacing was used in the machining. The bars are screwed to an inner thread in the vessel to keep them in place (Figure 4.9). The PMT sensors in the energy plane are supported by 12 cm of copper that close the copper cylinder at the EP side, called the carrier plate. It is screwed onto the vessel endcap inner thread, using two O-Ring gaskets, creating the isolated rear PMT volume to be kept at vacuum. The reduced shielding due to the presence of the PMTs themselves is compensated by 6 cm of copper fixed behind each sensor (Figure 4.9). A 12 cm copper plate with rectangular holes for the KDB tails closes the other side of the cylinder, called the support plate. It is also attached to the endcap but with sliding bars which are not tightened since the gas will flow around the edges of the shielding during operation.

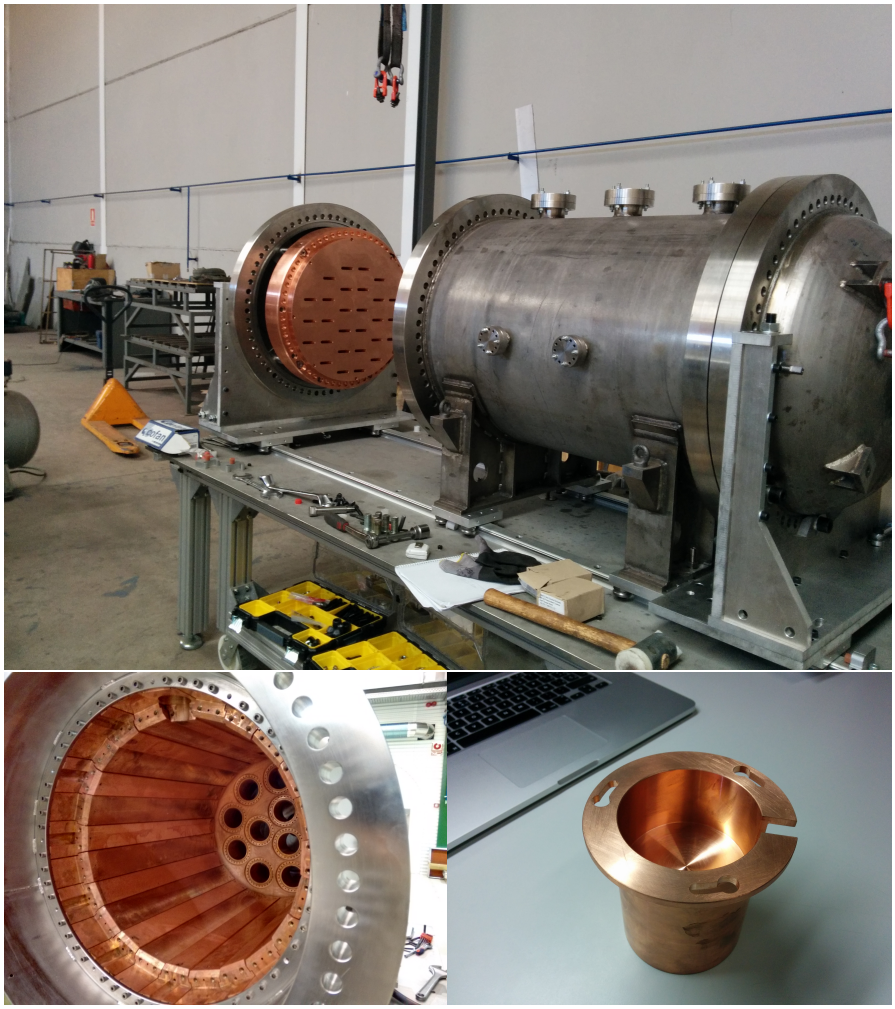

Figure 4.9: (Top) The vessel with the TP endcap opened showing the TP copper shielding. Copper bars barrel screwed on the inner vessel thread (bottom left) and the copper top-hat extra shielding (bottom right).

4.5 The readout electronics and data acquisition system

The NEXT data acquisition system (DAQ) has been developed through the prototype phases following the modular architecture of the scalable readout system (SRS) [130] developed with the CERN RD51 Collaboration [131, 132]. Lately, the SRS has been ported to the ATCA (Advanced Telecommunications Computing Architecture) standard.

The DAQ modules used are Front-End Concentrator (FEC) cards, which serve as the generic interface between the DAQ system and application-specific front-end modules. The FEC module can interface different kinds of front-end electronics by using the appropriate plug-in card. Those are based on FPGA and can interface a DAQ PC farm via GbE links, thus reducing the DAQ and trigger systems to a network-based architecture [133].

Three threads are differentiated in NEXT, and here are described for NEW. For the energy plane readout digitization, the first step in the chain is done at the PMT base, it shapes and filters the fast signals produced by the PMTs (less than 5 ns wide) to match the digitizer and eliminate the high frequency noise. An integrator is implemented by adding a capacitor and a resistor to the PMT base. The charge integration capacitor shunting the anode stretches the pulse and reduces the primary signal peak voltage accordingly. The design uses a single amplification stage based on a fully differential amplifier, which features low noise (2 $\mathrm{nV}/\sqrt{\mathrm{Hz}}$) and provides enough gain to compensate for the attenuation in the following stage, based on a passive RC filter with a cut frequency of 800 kHz. This filtering produces enough signal stretching to allow acquiring many samples per single photo-electron at 40 MHz, in the first stage of the DAQ.

The energy plane signal (12 PMTs) is read out from the EP feedthroughs (see Figure 4.5) via shielded twisted pair cables to 2 FE boards (8 channels per board in a 19 Eurocard crate) by Lemo conectors. The signals from the front ends are transmitted in groups of two via HDMI cables to two 24-channel ADC (7 channels used in one card and 5 in the other) mezzanine plugged onto half ATCA-FEC module (Figure 4.10). The 2 front-end amplifier boards are fed with an HMP4040 (HAMEG) power supply.

In Figure 4.10 the CAEN HV power supply for the PMTs can also be seen. The HV is fed from the CAEN unit to the front end using SHV cable and connectors, and is delivered to the twelve in-vessel PMTs via 12 HV cables.

In the tracking plane readout digitization, the SiPMs signals are extracted via 28 groups of 4 FFC (§ 4.3), a 4-group per KDB, to the electronics rack (Figure 4.10). There, the front-end boards integrate and digitize (12 bit, 1 MSa/s) the 64 SiPM channels per KDB, resulting in approx. 1 Mb of data per event per front-end board. The FEB64v2 front-end has a FPGA that read the ADC signal, implement the double buffer and allow the zero suppression. Counting 1 ms events and a 10 Hz trigger rate, the SiPM tracking partition generates 35 MByte/s in raw data mode [133]. Therefore, for reading out the 28 SiPM front-end boards in the tracking plane partition, one and a half ATCA-FECs (see Figure 4.11) and a total of three digital interface mezzanines (each one having 12 DTCC interfaces over HDMI) are used. Front-end boards work in free-running mode, storing data continuously in a circular buffer. Data are only sent to the ATCA-FEC modules when a timestamped trigger is received.

The trigger generation is implemented in a FPGA and search candidates based on early energy estimations, promt PMT signal and/or other threshold parameters [134]. The trigger front-end module is mezzanine connected to another half ATCA-FEC.

As a result, three ATCA-FECs are needed to read out the detectors energy and tracking planes and implement the trigger algorithm. Each ATCA-FEC interfaces a DAQ PC via 4 Gigabit Ethernet optical links.

At the top of the hierarchy, a PC farm running the DAQ software, DATE, receives event data from the DAQ modules via Gigabit Ethernet optical links. The DATE PCs (local data concentrators, LDCs) assemble incoming fragments into sub-events, which are sent to one or more additional PCs (global data concentrators, GDC). The GDCs build complete events and store them to disk for offline analysis.

Additionally, the slow control system (Figure 4.14) also comprises a small National Instruments compactRIO chassis, installed besides the vacuum pumps. The system is in charge of reading two temperature

Figure 4.10: Electronics racks: the Slow Control PC also resides in this rack.

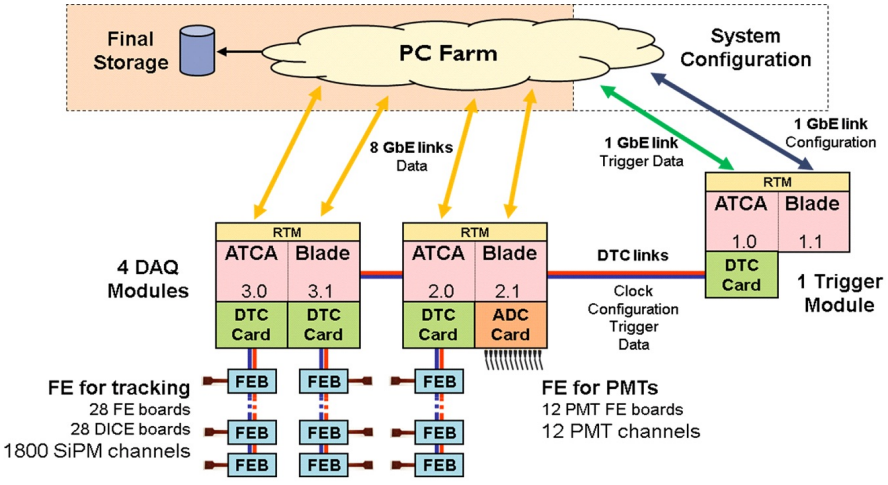

Figure 4.11: DAQ scheme.

sensors for the EP front-end boxes (used to detect overheating due to a malfunction in the fan tray or fire), one vessel pressure sensor and a PMT side pressure sensor. The above described electronics connect to the LSC mains power line via UPS units for enhanced safety and protection. All the electronics (front-ends, power supplies, slow controls...) stands close to the vessel but outside the shielding castle to reduce the signal transfer losses as can be seen in Figure 4.10.

4.6 The gas system

Unlike other detection media the quality of the xenon can be improved after assembling by continuously recirculating the gas through purifiers. To optimize the electron lifetime, and thus electron collection efficiency, the gas is filtered reducing the electronegative impurities (mainly O_2, H_2O and CO_2) that attach to the ionization electrons producing recombination. The knowledge acquired with the prototypes permitted the Collaboration to scale up directly to the gas system to be used for NEXT-100. The main improvements required for operation underground and with the expensive enriched xenon are related to safety. Certification of the system required the demonstration of different states of operation as well as emergency and planned recuperations.

A distinction of different parts included in the gas system can be done as the usual procedure:

1. Depressurization of the detector (Vacuum pumps):
   Three turbo molecular pumps —one dedicated to the detector, another used to continuously pump the evacuation tank and the last for the gas system itself—evacuate the system to achieve a vacuum level of 10^{-5} bar. There is an extra molecular pump to maintain the vacuum continuously in the volume behind the energy plane. Before filling with xenon the system is brought to vacuum and those parts of the system not sensitive to heat, the tubing and the main detector volume itself, are warmed to aid with the removal of any water vapour attached to the inner surfaces of the materials. After that, some cycles of filling the system with Argon and then vacuum-pumped again demonstrate to successfully reach the conditions to fill with Xenon. The process

is monitored and the amount of impurities check with two RGA giving the identification and quantification by spectrometry.

2. Pressurization of the detector and recirculation:
   Initial filling of the detector is done directly from the bottle since the system is at vacuum. Then the gas circulation starts thanks to the compressor. This is the most vulnerable component and has to have redundancy to avoid failure or leakage. NEXT chose a compressor manufactured by SERA [135], made with metal-to-metal seals on all the wetted surfaces. The gas is moved through the system by a triple stainless steel diaphragm. Between each of the diaphragms there is a sniffer port to monitor for gas leakages. The gas moves through the re-circulation loop passing by the getters that clean it, depending on the gas conditions by the cold getter (MicroTorr MC4500-902FV) usually first, and later on through the hot getter.

   The first removes water and oxygen, still some in the detector the firsts days of recirculation, but produces radon [136]. The gas system contain two cold getters in parallel with a bypass. The second spare getter is placed in parallel to allow, in case of accidental contamination of one of the getters, uninterrupted running. On the other hand, the hot getter also remove nitrogen and methane without radon emanation, but can be saturated and that is why the two of them in serie have to be operated.

3. Evacuation:
   Two different procedures and systems had to been implemented for evacuation of the gas. If the gas needs to be recovered in a controlled way, it is cryo-pumped with liquid nitrogen surrounding the recovery bottle by condensation producing pressure gradient. This recovers slowly the gas through all the gas system.

   On the other hand if an emergency recovery is needed, the CARTEN valve opens the gas flow path from the detector vessel itself to a vacuum kept recovery tank (actually the NEXT-100 vessel).

These main components are connected via tubes and valves shown in the Figure 4.12. It also includes calibrated bursting disks in case

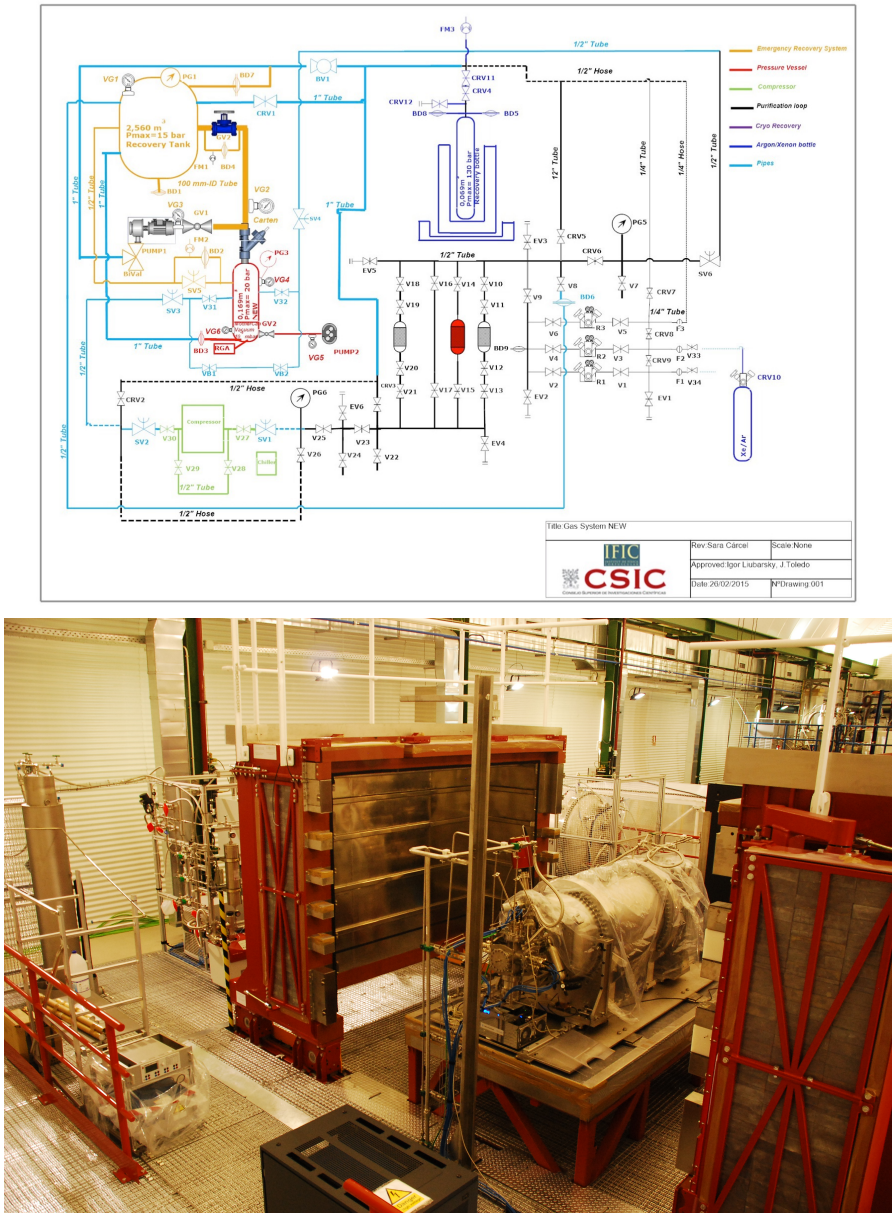

Figure 4.12: (Top) Gas system schematics and a picture of the whole gas system (bottom). The gas flows clock wise (picture below) from the detector energy plane side to the recirculation and cleaning loop, to the compressor (see Figure 4.13) and enters in the detector from the tracking plane side.

Figure 4.13: Compressor at the forefront and emergency recovery path through the CARTEN valve (blue) at the background.

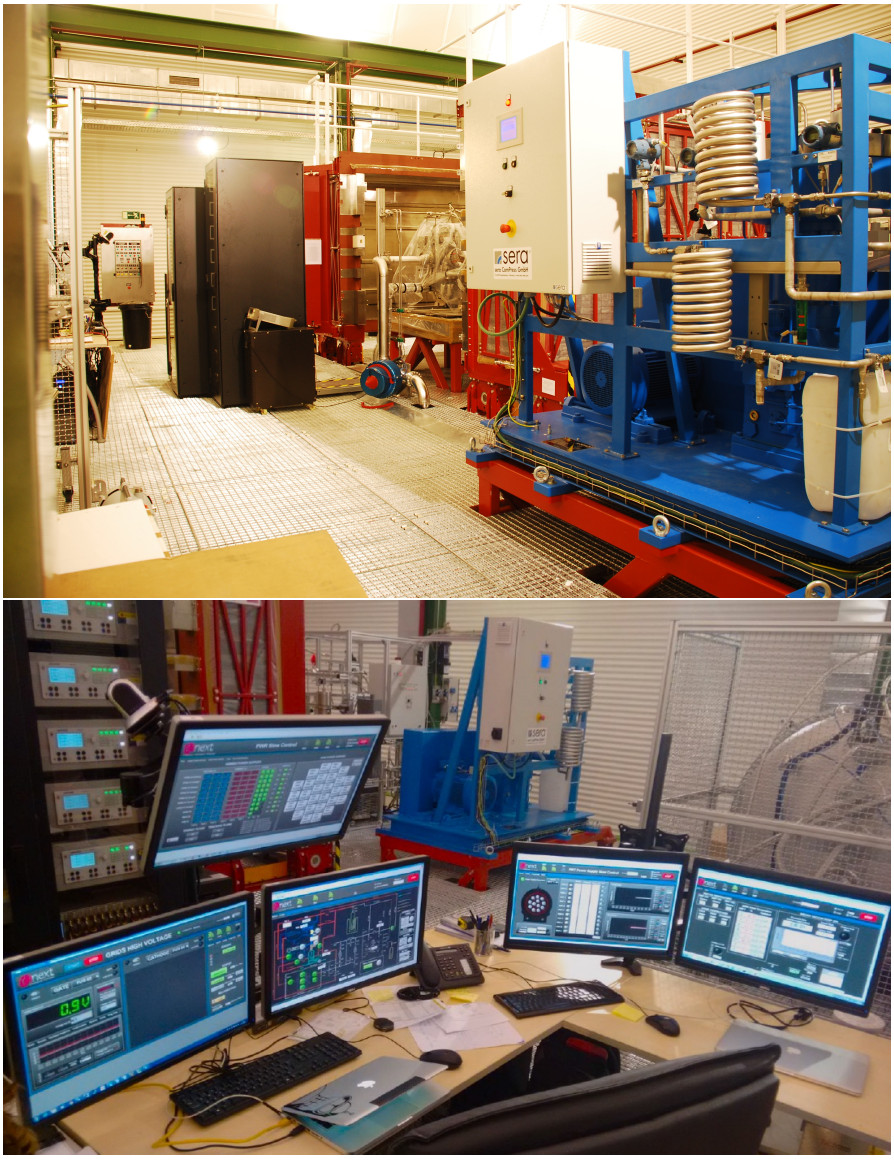

Figure 4.14: Slow control displays showing the monitor and controls for the gas system, HHV, sensors and electronics.

of over pressure as well as pressure and vacuum gauges controlled, programmed and continuously monitored by a complex LabView based slow control developed by the collaboration (see Figure 4.14). For example in the event of a leakage, automatic emergency shutdown of the compressor and gas recovery can be initiated.

4.7 The shielding system

As in other rare event detectors, together with the careful selection of the materials to avoid natural backgrounds, the detector must be shielded against external entering backgrounds.

Cosmic rays are significantly attenuated by operating underground due to the filtering power of the rocks. The Laboratorio Subterraneo de Canfranc (LSC) with $\sim$ 2500 meters water equivalent, offers five orders of magnitude reduction of the cosmic ray muon flux compared to sea level flux [37, 137], as a consequence muon-induced neutron backgrounds are also reduced (see more in Chapter 5).

To shield the detector from natural radioactive background coming from the laboratory rocky walls, a passive shielding was chosen already for NEXT-100. For this purpose lead is one of the most efficient materials due to its stopping power by its density. Ancient roman lead (in radioactive equilibrium with an activity in uranium and thorium lower than 0.4 mBq/kg) from the OPERA [138] detector was obtained by the LSC for a lead shielding castle around NEXT-100, insulating against external radiation. It is a rectangular box of 20 cm width walls, composed of $200 \times 100 \times 50$ mm^3 lead bricks half-timbered in layers. The total weight of the lead is $\sim$ 65 tonnes and the defined box dimensions are 195 cm width, 265 cm high and 293 cm length. Steel frame supports all the lead in place forming two halves mounted on a system of wheels that move on rails with the help of an electric engine. The castle has an open position for the commissioning and a closed position for the running term. The detector sits on the bottom wall of the lead box, not movable, fixed to the same structure as the rails. This very same pedestal is used also for the smaller detector NEW.

Due to the mild seismic activity of the part of the Pyrenees where the LSC is located, the detector —within the lead shielding castle— is fixed as a whole to an anti-seismic structure. This structure is anchored

through dynamic sink directly to the ground, being independent of the working platform to allow seismic displacements in the event of an earthquake.

An elevated working platform allows direct access to the detector and is where peripheral components such as the electronics racks are placed. Moreover, the gas system main components are placed to one side of the platform with the connective tubes passing through the platform floor to reduce dead volumes.

Both, underground operation offered by the LSC shielding and lead castle infrastructures, are already tested in NEW in preparation for the NEXT-100 operation.

Figure 4.15: Shielding structure during construction prior to any equipment and installation. Lead bricks conforming one wall of the shielding castle. View the shielding castle, without detector fixed on the pedestal, installed at Hall A of the Laboratorio Subterráneo de Canfranc

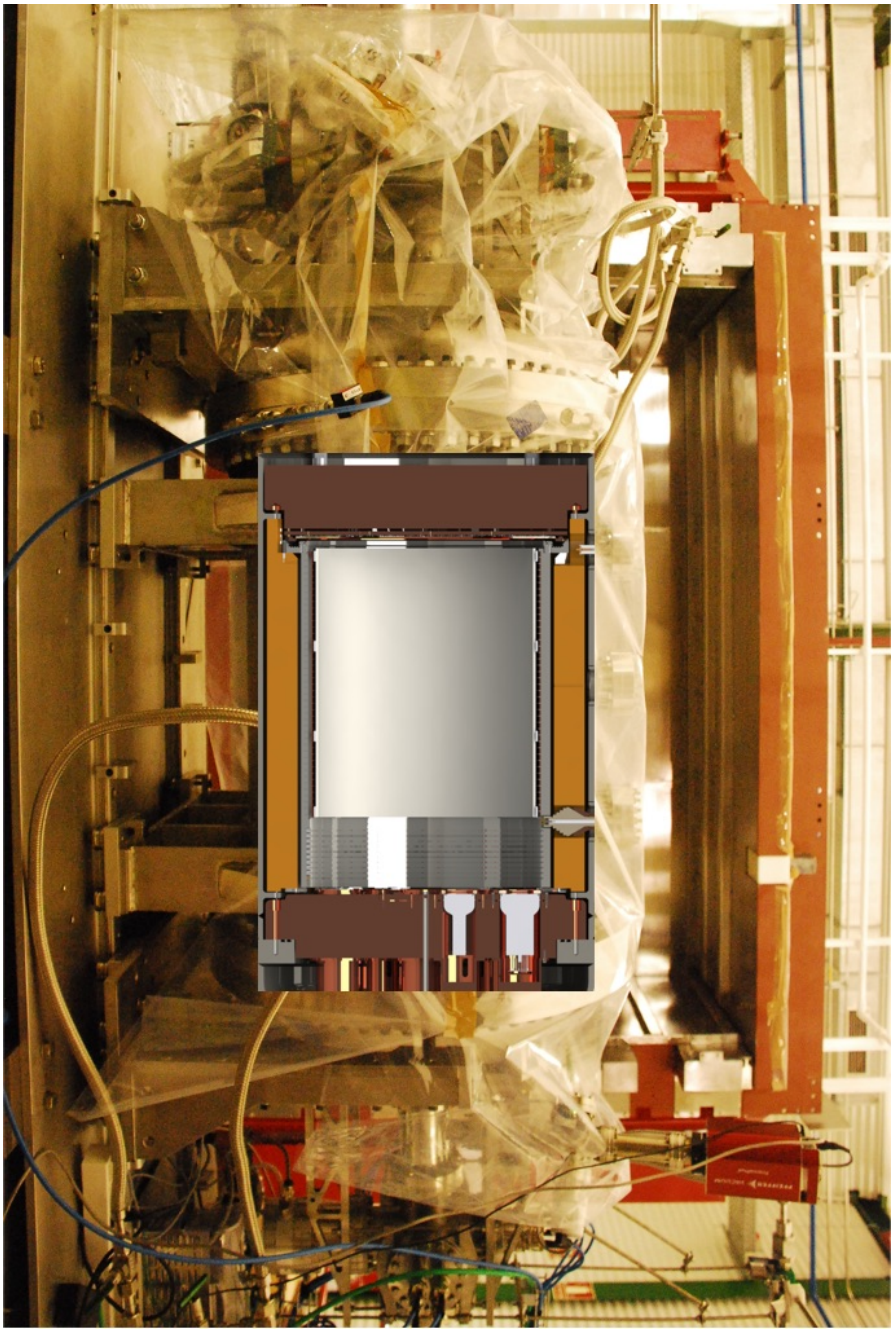

Figure 4.16: Artistic section cut view of the NEW detector in place.

"Our Sun is a second- or third-generation star. All of the rocky and metallic material we stand on, the iron in our blood, the calcium in our teeth, the carbon in our genes were produced billions of years ago in the interior of a red giant star. We are made of star-stuff."

Carl Sagan – "The Cosmic Connection: An Extraterrestrial Perspective"

Chapter 5

The background model of NEW

When starting a new experiment a preliminary evaluation of the performance has to be done to get a starting point for the design. Taking into account that NEXT Collaboration goal is search for $\beta\beta0\nu$ with NEXT-100, the intermediate step to acquire the knowhow has to fulfill some requirements.

NEW was conceived to demonstrate the four physics goals described in Chapter 4. The background rate predicted for NEXT-100 was based on detector activity simulations from material screening. Following the same approach, the modeling of NEW has been built on previous knowledge and extending it with some improvements. In this chapter a detailed description of how the model has been built up for NEW (§ 5.1) and the predictions that stand out are discussed (§ 5.5). It is also described how activity simulation can help in the design (§ 5.3) as well as how the extension of this model (and the improvements implemented on [110]) could validate it as a robust method for NEXT-100 sensitivity predictions.

For any experiment all possible interactions that can mimic the signal ($\beta\beta$-decay in the case of NEXT) are identified as backgrounds. Thanks to the features and the topology of our search (see Chapter 3), the high enough energy gammas producing ionized xenon electron

tracks as well as beta decays are object of background studies. For a complete model we distinguish different categories of background sources :

1. Radioactive contaminants for $\beta\beta0\nu$. These are impurities in detector components from the uranium and thorium series, particularly ^{214}Bi and ^{208}Tl decays from the materials. These are expected to be the dominant backgrounds around the energy region of interest for ^{136}Xe neutrinoless double beta decay ($\beta\beta0\nu$) searches, at $Q_{\beta\beta}$= 2.458 MeV. Therefore, their measurement is crucial for the verification of the NEXT-100 background model.

2. Radioactive contaminants relevant for $\beta\beta2\nu$. Besides the uranium and thorium natural radioactive series from materials, other radioactive contaminants with contributions in the $\beta\beta2\nu$ energy window are considered. The evaluation of the first will base the aforementioned background verification and the minimization of the last, expected to dominate at energies below 1.5 MeV, affect particularly the prospects for the measurements of the two-neutrino double beta decay ($\beta\beta2\nu$) of ^{136}Xe in NEXT in this energy region.

3. Radon contamination. As a intermediate product of the uranium and thorium series, it increases the ^{214}Bi (from ^{222}Rn) and the ^{208}Tl (from ^{220}Rn) contribution respectively. It is gas under normal conditions and being a noble gas, radon is chemically not very reactive and can diffuse easily through many materials infiltrating into the active region of the detectors. Two sources are considered: airborne radon surrounding the detector and generated from the material outgassing. Although chemically not very reactive has the possibility to be suppressed by active filtration system for its mitigation in contrast to the passive shielding used for the other backgrounds.

4. Backgrounds induced by cosmic rays and their by-products.

To study all the contributions, following sections describe how the detector and the physics processes are simulated, and how their impact is evaluated to provide the performance or the acceptable

levels of radioactive impurities of different proposed configurations. A brief description of the simulation tools used in these studies is given beforehand.

5.1 Simulation tools for Monte Carlo studies

The simulation software used is NEXUS (an acronym for NEXT Utility for Simulation), a Geant4-based [139] simulation program developed by the NEXT Collaboration [140]. NEXUS has been widely used by the Collaboration for sensitivity studies as well as for guidance during physics analysis. It has been validated using data whenever possible [77].

NEXUS covers the entire simulation process, from the generation and transport of particles interacting in the detector to the production of the associated primary signals (ionization electrons and scintillation photons) and their collection, amplification and detection.

Detector simulation in NEXUS is divided into several basic components that the user must define:

- `Detector geometry:` the physical layout of the simulated system, including a description (microscopic and macroscopic) of the materials used in its construction (§ 5.1.1).
- `Physics list:` a collection of physics processes and their associated particles to be considered in the simulation.
- `Event generation:` the initial conditions of each event to be simulated; that is, number and type of particles in the event, their position within the detector geometry and their initial three-momentum (§ 5.1.2).
- `User actions:` operations that retrieve data of interest to the user about the trajectory and interactions of particles as they propagate through the detector. This information is available at several processing stages during the simulation.

The user selects before runtime a component of each of the above categories via a macro file. These components may instantiate others, and have their own macro commands that let the user further refine the

simulation configuration. The output information from the simulation is saved in the form of high-level data objects —such as particles, tracks or detector hits— using ROOT [141].

For the case of background studies the energy deposited in the active volume by the radioactivity of the components that can mimic the signal is the objective. This can give the approximation to the signal to noise ratio of the detector. That evaluation, along with all the relevant physics processes produced in the detector (energy loss in xenon, primary scintillation, Compton and photoelectric interactions, pair production, electroluminescence ...) can be reproduced within NEXUS. Nevertheless there are CPU-time consuming processes bypassed for optimization. For the background model here described one of this simplifications is used: **Fast-Simulation**. Another time-saving-parametrization in simulations is used and described in Chapter 6 : **EL look-up tables**.

With the fast-simulation approach, the primary scintillation and the ionization charge plus its EL amplification is simplified simulating the energy and spatial resolution at the analysis level (§ 5.4) onto the MC-truth information. This gives a simulated response of the detector.

5.1.1 Detector geometry simulation

To study all the relevant processes to take into account, a virtual model of the detector has to be done. This could add information on how the detector behaves and what components become relevant. It has to reproduce all the real detector components, its performance —in terms of how they interact, block or favor our goals— and identify all the possible unexpected physics problems beforehand. Therefore, as an empirical model build up process, it has been focused in the parallel simulation development, to check the suitability of materials, more than the optimal statistical point of view for the ultimate model. Hence, this work has been carried out in direct contact with the design and building leaders, at the same designing time due to the bidirectional necessary communication. To get the most accurate virtual model some simplifications in the implementation of the designs (see Table 5.1) have been asumed. Also the feedback to the designing engineers team because of physics implications or not affordable components in terms

of backgrounds was needed (see § 5.2). Its important to recall that it is the first radio-pure detector designed by the Collaboration. Thus, we made all the project interactive and kept changing while improving it. This had some implications on the detector parts simulation order choice (following the necessity to check design performance in different steps) and moreover the number of events simulated due to the accuracy need for some critical components (see § 5.1.2).

The virtual model of the detector is done by reproducing with Geant4 its configuration. The building up of a simulated model is done in code modules that recreate each component. For optimum performance the components are nested emulating the real *matrioska* concept in the detector. They are arranged in subsystems so one component module could call several components to construct the subsystem. This organization system is shown in Figure 5.1. The idea is to encapsulate parts of the detector trying to not enclose all in one, this offers the possibility to modify separate parts as well as use specific parts of the detector to other simulation studies. Each part of the detector is in general a class by itself called later by other classes or by the detector general class. These features allow the use, for instance, of same external lead shielding class as NEXT-100 geometry (just as in real life) only changing few parameters in the initialization general class.

For implementing each module class component the code has typically three differentiated parts:

- Geometry constructor: Geant4 allows to produce several geometrical shapes with an invocation of the shape class method. The virtual component is called *logical volume*. In addition to the shape, it also allows to set dimensions, material and position on the virtual world via method parameters. Complex geometries can be created by adding or subtracting others, giving the possibility of simulate quite all the configurations but with a computational cost.

  Material properties are really important and had to be added or extended to the default Geant4 materials list within NEXUS to satisfy our special needs. The careful check and implementation

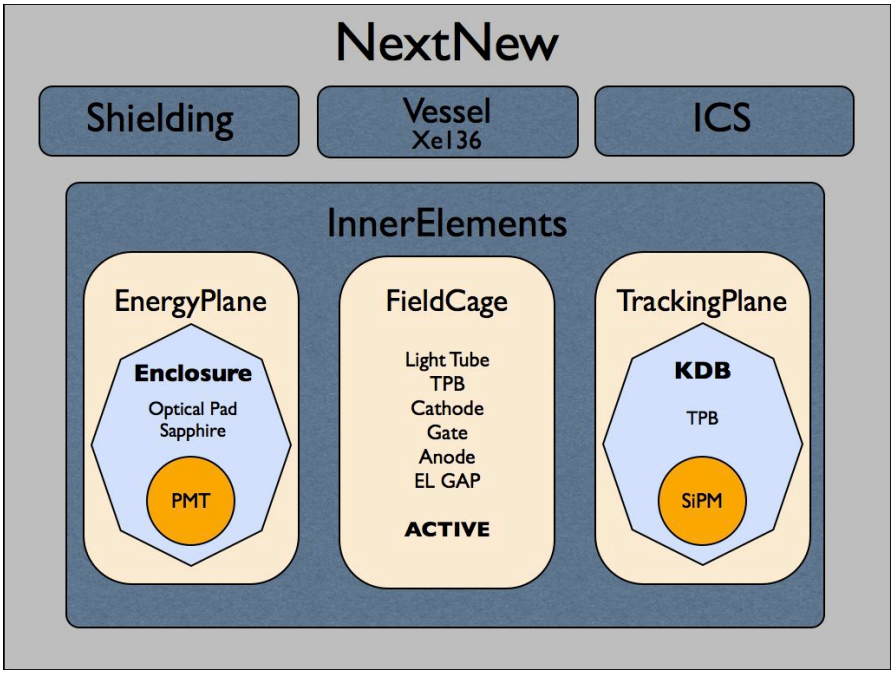

Figure 5.1: Hierarchical arrangement of the NEW detector NEXUS modules showing the independent classes and how are instantiated for the NEW background model simulation.

of the optical properties has to be taken into account since the detector uses photosensors readout. Any minor change on optical conversion, reflection or refraction factors to the photons interaction to be detected could become an important change in the final simulated performance. This is one of the things that was needed to update due to the lack of Geant4 models for the optical properties of some materials (TPB, teflon, sapphire...) [140].

It is also important to notice the physical properties set on the material for the process to occur when the particles interact with them, particularly the stopping power of the materials as shield for the case under study, is a common practice usage of Geant4 and no changes were needed.

- Point sampler: in order to meet the NEXT simulation needs, specially in the case of background studies, this feature had to be added too. Every single simulated component has a function implemented that samples a replicated geometry of the above constructor. It was needed to updated the Geant4 software within NEXUS to be able to launch each desired primary particles at the detector geometry parts needed. Since it is not how it was designed (mostly to register instead of generate interactions in a volume, energy deposited at the center of the experiment/collider) point coordinates —*vertex*— generator had to be implemented [140]. This generated vertices are then used by the next function on the class.

- Vertex generators: the previous function returns a collection of coordinates points from which generate the initial particle to study, but not all the components or parts of the same component have equal probability of action (in terms of activity simulation). In other words, intricate geometries do not have the same probability weight of radioactive events in all the points. For example, in the simple case of simulating an event from the vessel, that is constructed by a cylinder body and two symmetric endcaps, the probability of being shot from one of the elements its proportional to its volume. Therefore, the biggest the element (related with its mass and hence its activity) the more probable to be selected.

Besides the probability of action, the point sampler gives a coordinate relative to its element sampled and then in the vertex generator has to be rotated and/or translated to the actual place of the element in the whole model. When simulating an statistical high enough amount of events, they are distributed following the geometry of the element (§ 5.4).

Nevertheless, it has to be taken into account that even though a detailed model is preferred, it has to be paid in computing time and then some simplifications in the geometry implementation have to be done. This requires a careful addition for the element parts not simulated but added to the total mass evaluation. For the same example as above, the vessel nozzles are not sampled and its weight assigned to each containing element. The simplifications assumed for the NEW background model geometry construction are resumed in Table 5.1.

When started the building up of the NEW model implementation, the first approach was to implement a basic geometry with a few components of the detector (sensors, vessel, field cage body, ICS and ^{136}Xe), to check the behavior of the processes. Then add elements to the geometry simulation to be the most close to the final detector design. The virtual geometry of the detailed model of NEW can be seen in Figure 5.2.

5.1.2 Event generation

Among the developments needed for the simulation of NEW, there were some primary particle generators. One of the objectives of NEW is the background evaluation for the NEXT concept, but also the measurement of the $\beta\beta2\nu$. Therefore, not only the well characterized backgrounds for $\beta\beta0\nu$ but lower energy backgrounds were under study.

Changes were introduce to use *ion gun* generator instead of *single particle* generator. The first generator let us create a radioactive element —by specifying the mass number (A) and the atomic number (Z) at the configurable macro— and take advantage of the Geant4 RadioactiveDecay physics package. Unlike *single particle* that creates only the electron or the gamma desired for a specific background study,

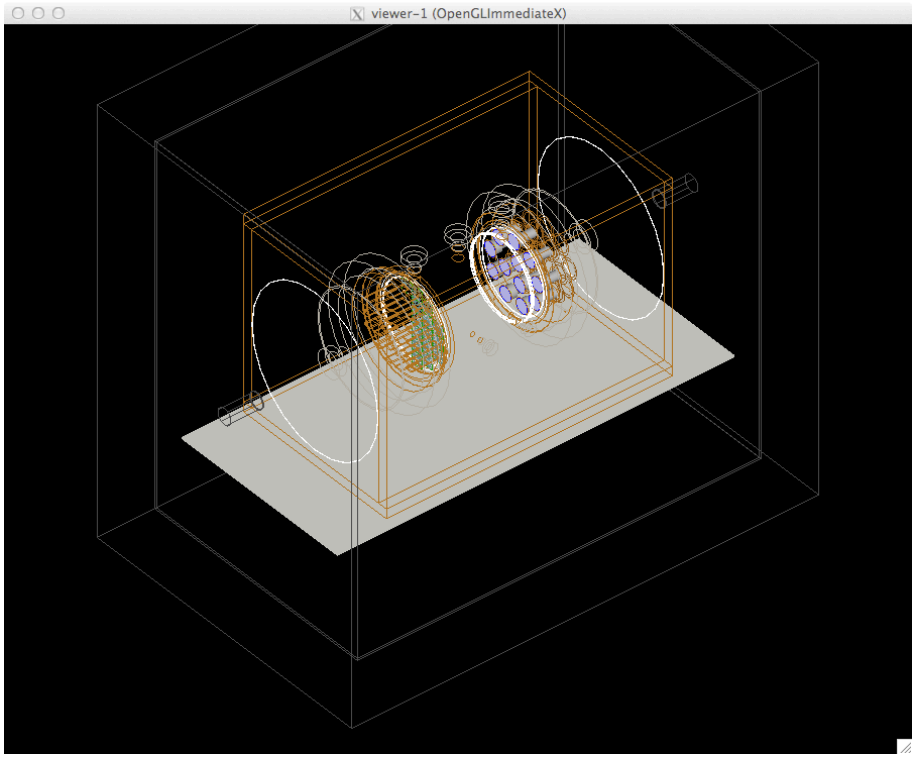

Figure 5.2: Simulated NEW detector geometry visualization.

Table 5.1: Table of all available coded NEW geometries with some comments on their implementation.

vertex name	Sim. material	comments
ACTIVE	gas	gas type via parameter, set of attributes
BUFFER	gas	gas type via parameter, set of attributes
CATHODE	dielectric	optical material properties
DRIFT_TUBE	G4_TEFLON	light tube
DRIFT_TPB	TPB	optical material properties
FIELD_RING**	G4_Cu	no vertex sampler (use HDP)
HDPE_TUBE	HDPE	barrel active+buffer
EL_GRID_GATE	dielectric	optical material properties
EL_REGION*	gas	EL_TABLE
EL_GAP	gas	gas type via parameter, set of attributes
ANODE_QUARTZ	FusedSilica	OpticalMaterialProperties
TPB_ANODE**	TPB	OpticalMaterialProperties
ITO_ANODE**	ITO	OpticalMaterialProperties
ICS	G4_Cu	cylinder with penetration holes
CARRIER_PLATE	G4_Cu	cylinder with holes and front buffer
ENCLOSURE_BODY	G4_Cu	passing cylinder with backside shield, host next pieces
ENCLOSURE_WINDOW	Sapphire	OpticalMaterialProperties
OPTICAL_PAD	OpticalSilicone	OpticalMaterialProperties
PMT_BODY	Kovar-FusedSilica-G4_Al	two body volumes, window and photocathode union, vacuum inside, sensitive detector, total and partial vertex
PMT_BASE	G4_KAPTON	one factor for all base components
SUPPORT_PLATE	G4_Cu	cylinder with holes and tread, host next pieces
DB_PLUG	PEEK	build at its final place, not connected, constructed in TP
DICE_BOARD	G4_KAPTON	only simulated the square front, no tail. ClassName: KDB, host next pieces
TEFLON MASK**	G4_TEFLON	constructed in KDB, no vertex sampler (use KDB)
SiPM**	G4_Polycarbonate-G4_Si	MaterialProperties, sensitive detector, no vertex sampler (use KDB)
VESSEL	Steel316Ti, gas	body, flanges, endcaps and nozzles. filled with different gasses. include generators for the SOURCE_PORT_ ANODE, UP and AXIAL
SHIELDING_LEAD	G4_Pb	external box, only 2 internal cm active
SHIELDING_STRUCT*	Steel	only those beams facing the detector, placed inside the lead
SHIELDING_STEEL	Steel	internal box
SHIELDING_GAS	gas	to use for air or nitrogen shielding, used also for radon attached on walls: RN_SHIELDING_GAS*
EXTERNAL		extra space for NEUTRONS simulation
CU_CASTLE*	G4_Cu	possible internal shielding
RN_CU_CASTLE*		used for radon attached on walls
PEDESTAL	Steel	only steel plate
RN_TUBE*	gas	surrounding detector for radon studies
MUONS		vertex generator above the shielding
LAB		vertex generator environment

*only for specific studies **no vertex generator

this allows to study the complete chain of decay products. Thus one can study the impact of the well known radioactive backgrounds for rare event searches, the ^{238}U and ^{232}Th natural radioactive chains. The implementation, debugging and usefulness of this generator is partially part of this work. It serves for specific study needed for the evaluation of the NEW backgrounds and is discussed in § 5.3. This upgrade was also used for the evaluation of the NEXT-100 sensitivity [110].

Two other generators in the simulation were also developed for necessity: Neutron generator and muon generator. This was done for the specific evaluation of the cosmic induced backgrounds in NEXT. Its discussion is done in § 5.3. The implementation of dedicated generators has been done due to the further improvement of using *single particle*, as well as for the previous case, but their different origin: not radioactive decays of itself but induction of other decays. For the case of the neutrons, the measured energy profile of its activity in the LSC [142] was implemented in the generator. The proper activity in the LSC is then reproduced for NEXT coming from the outside of the shielding. The neutrons are generated in a thin layer surrounding the shielding in order to minimize their travel distance. If their were shoot from the lab walls their tracking through the air would have consumed CPU resources. Moreover, the neutrons are generated isotropically.
The same background inducer nature of the cosmic muons arriving to the LSC indicate the same procedure. Thus a dedicated muon generator reproducing the spatial profile of the measured muon activity at the LSC [137] was done. Figure 5.3 shows the reproduced energy spectrum for the neutrons and the angular spectrum for the muons in the LSC by the implemented generators.

For the generation of the signal ($\beta\beta2\nu$) events the DECAY0 [71] generator was used.

Following the the Monte Carlo data generation, after the use of one of the aforementioned generators, all the relevant physics processes are taken into account and the energy deposition of charged particles in gas are recorded.

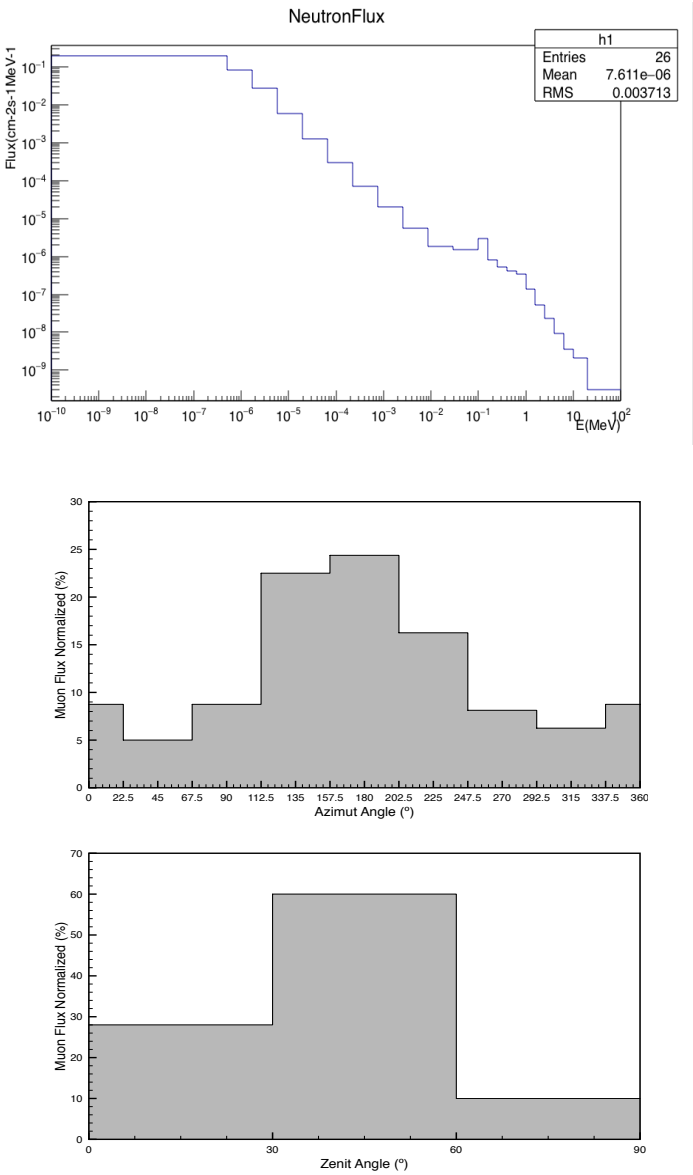

Figure 5.3: Neutron energy distribution (top) and Muon angular distribution (center and bottom) reproduced by the NEXUS generators from the measured LSC activity.

5.2 Material activity assessment

Besides the software simulations, the other big contribution to the background model comes from the input of measured radioactivity of the materials used. This is a huge work done mainly by the radiopurity service group and implies, as the communication with the design engineers for the geometry simulation, a direct coordination with the people in charge of the activity measurements. Cooperative work is needed: they give the measurements for the model to evaluate its impact and some ordering (critical components first) advise or the necessity of further investigation (in case of limits and materials with huge activity contribution) can be given.

With the objective of measuring the radioactive rate of all the materials to be used in NEXT, a material screening and selection process for NEXT components has been underway for several years, both to inform the experimental design and to help construct a realistic background model. Screening campaign has been weight driven, sampling a little amount of each construction material while the optimum would be to screen the whole system. This implies the assumption that the whole material behaves as the sample screened, specially in the case of big elements with the chance to measure different manufacturers of the same material (*batch*) previously to its fabrication. For example, the stainless steel for the vessel, the copper for the inner shielding, plastics for the field cage barrel, lead for the outer shielding, steel for the supporting structures, substrates for electronics... Nevertheless some other components were screened once fabricated, with previous selection from literature information, in one piece like the sensors (PMTs and SiPMs).

Determination of the activity levels is based on gamma-ray spectroscopy using the ultra-low background high purity germanium (HPGe) detectors (see Figure 5.4) of the Radiopurity Service of the LSC [143]. Despite the high environmental isolation, cleaning and detector sensitivity, the exposure of some components reached the background of the HPGe. That only allows to set un upper limit on the activity of the exposed material. For most components the measured activity or the upper limit was enough information to evaluate them and be classified as low background contribution to NEXT. For those material which could be sampled and can stand or afford complete destruction

of the material, glow discharge mass spectrometry (GDMS) and/or inductively coupled plasma mass spectrometry (ICPMS) techniques were used to improve the measurement or limits. Other materials —like quartz— can not be sample and/or are too expensive to lose them, hence limits or other measurements quoted from literature have been used.
Another assumption for the material activity assessment, once the spectroscopy data has been analyzed with the distribution effect weighted from simulations, is the upper-lower chain stability assumption [109]

It is worth to mention some particular cases of material screening because its approach or its results:

- The PMTs measurement: The knowledge before hand (from the NEXT-100 simulations) that sensors would be the most relevant component as background contribution, drive to a different approach for PMT screening. With the necessity to check all of them not just a sample, but the too large time scale for individual characterization, the measurement of three PMTs at a time allowed to identify non tolerable activities and select those PMTs matching the requirements. At the end it had enable the characterization of all in a reasonable time and asses a measurement for the PMT activity showing equivalent activity between them. A joint analysis of the eighteen independent corresponding runs have been performed resulting in the publication of all the results [144] found in good agreement with other studies [145, 120, 146, 147].

- The SiPMs measurements: This is one of the specific cases where the analysis brought up an alert on the use of the material. The activity measured by the HPGe was not high but its contribution to the total background after the analysis for NEXT-100 showed an unacceptable high activity values for the Hamamatsu MPPCs. Mainly due to its position in the detector, the impossibility to shield them and the amount of them to be used. SiPMs from the SensL company were chosen following a successful radioassay.

- The Shielding structure paint: In the previous cases, the sensors, were critical due to their crucial role in the detector, but another

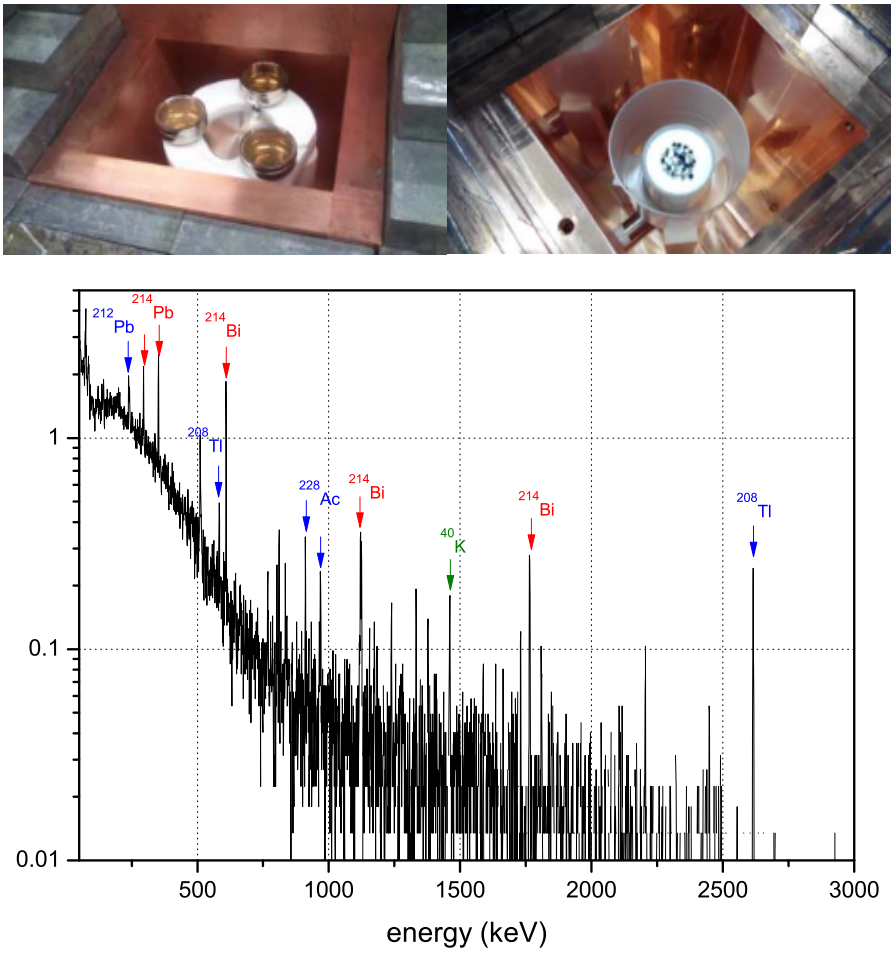

Figure 5.4: (Top) Pictures from the LSC Radiopurity Service of the procedures and sample installation of material screening: PMT R11410-10, Hamamatsu (run 17) at left and SiPMs 6×6 mm^2, SensL at right. (Bottom) Recorded spectrum of a complete screened material by the HPGe *Oroel*.

Table 5.2: Radioactive budget of the NEW detector.

Component	Material	Unit	Quantity	^{208}Tl	^{214}Bi	^{40}K	^{60}Co	Technique
Dice Boards	Kapton Boards	Bq/Unit	28 Units	1.00E-05	7.00E-05	1.45E-02	<6.00E-06	Ge/NEXT
	LEDs	Bq/Unit	28 Units	1.08E-09	1.40E-09	<4.00E-09	<3.00E-09	Ge/NEXT
	SenseL 1x1	Bq/Unit	1792 Units	<7.20E-10	<2.70E-09	1.60E-08	<8.00E-10	Ge/NEXT
Anode	Quartz	Bq/kg	1.5 kg	3.40E-05	2.10E-04	6.50E-04		EXO
Field Cage	HDP	Bq/kg	17.11 kg	<7.56E-06	<6.20E-05	4.16E-03	<1.40E-04	ICPMS/NEXT
	Resistors	Bq/Unit	84 Units	1.10E-08	8.50E-08	4.00E-05	1.10E-06	EXO
	Copper rings	Bq/kg	15.54 kg	<4.3E-05	<1.2E-05	3.1E-05	<2.00E-04	GDMS /NEXT
ICS	CuA1	Bq/kg	615 kg	<1.44E-06	<1.20E-05	6.20E-05	4.10E-05	GDMS /NEXT
PMT Body	Hamamatsu	Bq/Unit	12 Units	1.90E-04	3.50E-04	1.18E-02	3.73E-03	Ge/NEXT
Vessel	316Ti SS	Bq/kg	645 kg	<1.48E-04	<4.60E-04	<1.20E-04	4.40E-03	GDMS/NEXT
Carrier Plate	CuA1	Bq/kg	215 kg	<1.44E-06	<1.20E-05	6.20E-05	4.10E-05	GDMS/NEXT
Support Plate	CuA1	Bq/kg	303 kg	<1.44E-06	<1.20E-05	6.20E-05	4.10E-05	GDMS/NEXT
Enclosure Body	CuA1	Bq/Kg	49.2 kg	<1.44E-06	<1.20E-05	6.20E-05	4.10E-05	GDMS/NEXT
Enclosure Window	Sapphire	Bq/kg	1.654 kg	4.40E-05	<3.1E-04	<2.10E-04	<7.00E-04	EXO/NEXT
	Optical Gel	Bq/kg	0.02568 kg	<6.50E-03	<2.2E-02	<1.73E-01	<4.5E-03	Ge/NEXT
Shielding Lead	Lead	Bq/Kg	15614.7 kg	3.39E-05	3.47E-04	1.24E-04	<8.00E-05	GDMS/NEXT
Shielding Struct	Steel	Bq/Kg	418.99 kg	1.60E-03	1.20E-03	3.2E-03	1.80E-03	Ge/NEXT
	Paint	Bq/Kg	1.3 kg	4.70E+01	5.23E+01	1.85E+02	<5.00E-02	Ge/NEXT
Pedestal	316TiSS	Bq/Kg	360 kg	<1.48E-04	<4.60E-04	<1.20E-04	<4.40E-03	GDMS/NEXT
Cu castle	CuA1	Bq/Kg	4056.56 kg	<1.44E-06	<1.20E-05	6.20E-05	4.10E-05	GDMS/NEXT

case where the analysis brought up an alert on the use of a material was for an apparently harmless structural material. The steel structure used for holding the lead shielding bricks in a box design, had the need to be rust protection painted. Thanks to the detailed plans of the radiopurity service to study and/or screen all the materials used in the construction, this paint was found to be to high contribution for a non unavoidable material approach (see § 5.5).

- The electronic connectors: The necessary connector for the SiPM boards were already know from bibliography to be quite active but the measurement of different providers support the solution of the Kapton® boards (KDB) design. The long flexible Kapton® tails place the radioactive connectors behind the copper shielding, thus allowing the usage of the known connectors from the background model studies.

The procedures, measurements and plans of the radiopurity task has been published in [109, 148, 149, 128, 150, 144] where all the materials studied for the NEXT design can be found; here only the selected ones and therefore used in the background model are referred.

The radioactive budget of the NEW detector is summarized in Table 5.3. For every major detector element, the activities of ^{208}Tl (from the thorium series), ^{214}Bi (from the uranium series), ^{60}Co and ^{40}K are listed. Most of these measurements have been carried out by the NEXT Collaboration and the LSC Radiopurity Service.

5.3 Backgrounds: identification and description

NEXT need a vast knowledge of its backgrounds since its conception due to the nature of its searches. This has been extended as the experience on setting up the prototypes, simulations and projections of performance was taking place.

In this section the current knowledge of the nature for the affecting backgrounds, the work done to its understanding and how are studied,

is described, with the focus on NEW (as experience gives information) but some implications for NEXT-100 are also presented. The most updated picture of the model with the analysis used to get to the final numbers is discussed in the following sections (§ 5.5, § 5.4).

It has been introduced previously the classification of the backgrounds for NEXT with the distinctiveness that the NEW physics goals has opened a different treatment of backgrounds. That is to say that the differentiation and look for new candidates to be backgrounds in the $\beta\beta2\nu$ energy region has to be taken into account in addition to those for the $\beta\beta0\nu$ contributions to think on the validation of the model for NEXT-100. The definition to become a background to be studied is any signal-like event (single track topology Figure 3.1) inside the active volume. Any signal produced in the detector that can mimic the search is a background, for NEXT four types are distinguished:

5.3.1 ^{208}Tl and ^{214}Bi decays relevant for $\beta\beta0\nu$ energy window

The natural abundance of the radioactive daughters elements in the uranium and thorium decay chains is a well known problem for all rare events searches. For the NEXT physics case, the ^{208}Tl and ^{214}Bi (coming from ^{232}Th and ^{238}U decay chains respectively, see Figure 5.5).

The ^{208}Tl beta decay emits an electron and a de-excitation gamma from the daughter (^{208}Pb stable) with 2614.511 keV [151]. The electron track coming from the surrounding elements, in case of energy close to the region of interest (ROI), can be vetoed. Instead, the contribution from the de-excitation gamma, that eject an electron from the xenon by photo-electric production with this energy, emulates the signal track and bounds the right side of the $\beta\beta0\nu$ ROI. The Compton edge of this 2.6 MeV gammas bounds the other side (2382 keV), fortunately leaving a clear space for detecting the ^{136}Xe $\beta\beta0\nu$ (2458.1 keV) if good enough energy resolution.

More complex is the ^{214}Bi beta decay, which its ^{214}Po daughter emits also some de-excitation gammas around the $Q_{\beta\beta}$. Most of them are low probability emission gammas but the 2447 keV (1.57% intensity [151]) just at the ROI, produces a photoelectric peak that partially

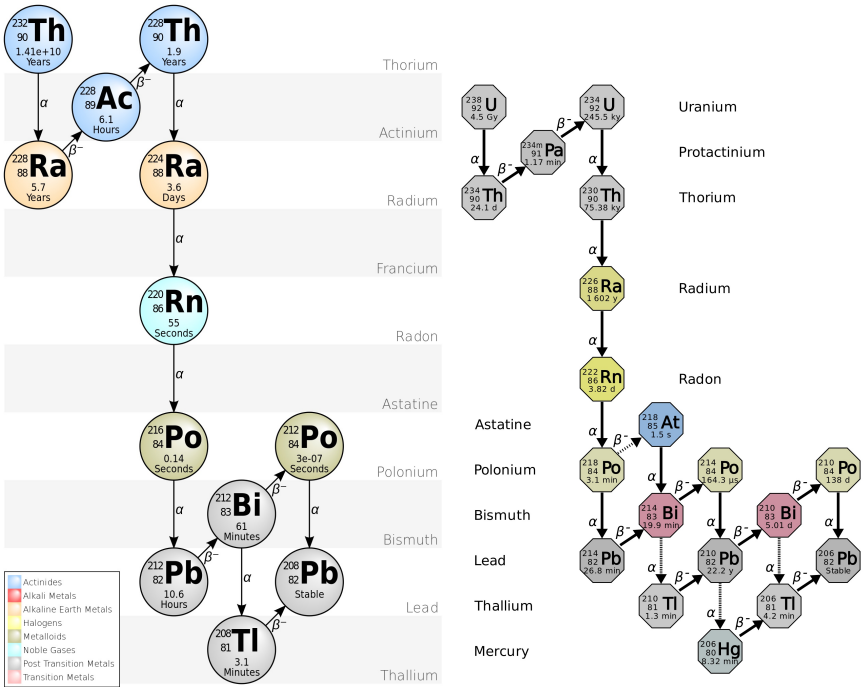

Figure 5.5: Natural decay chains of ^{232}Th and ^{238}U [152].

overlaps with the signal even with the best energy resolution [110].

Therefore, the minimization of this contributions will help to achieve the desired low background contributions for the $\beta\beta0\nu$ searches in NEXT-100. The characterization of the total amount of ^{214}Bi and ^{208}Tl with NEW will allow to extrapolate its contribution in the ROI, assess the background rate and the sensitivity of NEXT-100 in the very same design. For this reason, although not too relevant for the NEW physics case, this background type emphasizes in the necessity of characterizing as much used materials as possible, this is the contribution of this work to the study of this background type.

5.3.2 Radioactive contaminants relevant for $\beta\beta2\nu$ energy window

Being one of the goals of NEW the measurement of the $\beta\beta2\nu$ half-life, not only the backgrounds in the $Q_{\beta\beta}$ region have to be studied but in the whole energy spectrum (the $\beta\beta2\nu$ ranges from 0 to $Q_{\beta\beta}$ keV).

Then, the above contributors, although being well known backgrounds for $\beta\beta0\nu$ searches, had to be particularly characterized for the whole energies. That is to say, to study how the natural abundant ^{238}U and ^{232}Th series could cover up the $\beta\beta2\nu$ spectrum. First approach was to define the NEW ROI and check if some other elements from de radioactive series could have a relevant impact. Using the NEXUS generator (§ 5.1.2) and registering the tracking of all those elements generated by G4RadiactiveDecay from the initial isotope of the chain (^{238}U and ^{232}Th), all the gammas emitted and its producer can be identified for all the decay time. In the Figure 5.6 is shown all the emitted gammas in the decay chain, with its probability and identified the emitters. There can be seen that the gamma emission is more abundant below 1 MeV. Thus a preliminary characterization of those above is shown.

Besides the gamma interaction potentially producing electron tracks via photoelectric or Compton, it is really interesting for NEXT the pair production process, which can bee seen as an double electron track (electron-positron) that emulates the $\beta\beta$-decay topology. With gamma energies above 1022 keV, pair production events can occur. The 2.615 MeV gamma emitted from the decay of ^{208}Tl, can produce e^+e^- pairs (double electron track like) and the positron annihilation producing two back to back 511 keV gammas that escape the detector (miss the energy reconstruction) creates the prominent ^{208}Tl double scape peak at 1.6 MeV (see Figure 5.19). These events, an electron and a positron emitted from a common vertex, have the same $\beta\beta$ topology, and can be used to show the pattern-recognition capabilities [77].

In addition to the previous contributions, it is known from the literature that some isotopes use to became backgrounds for rare events searches [153], of which ^{40}K and ^{60}Co are presents in the screening of some material for NEXT [109]. With prominent peaks in the middle of the $\beta\beta2\nu$ energy distribution (1.17 MeV, 1.33 MeV gammas from

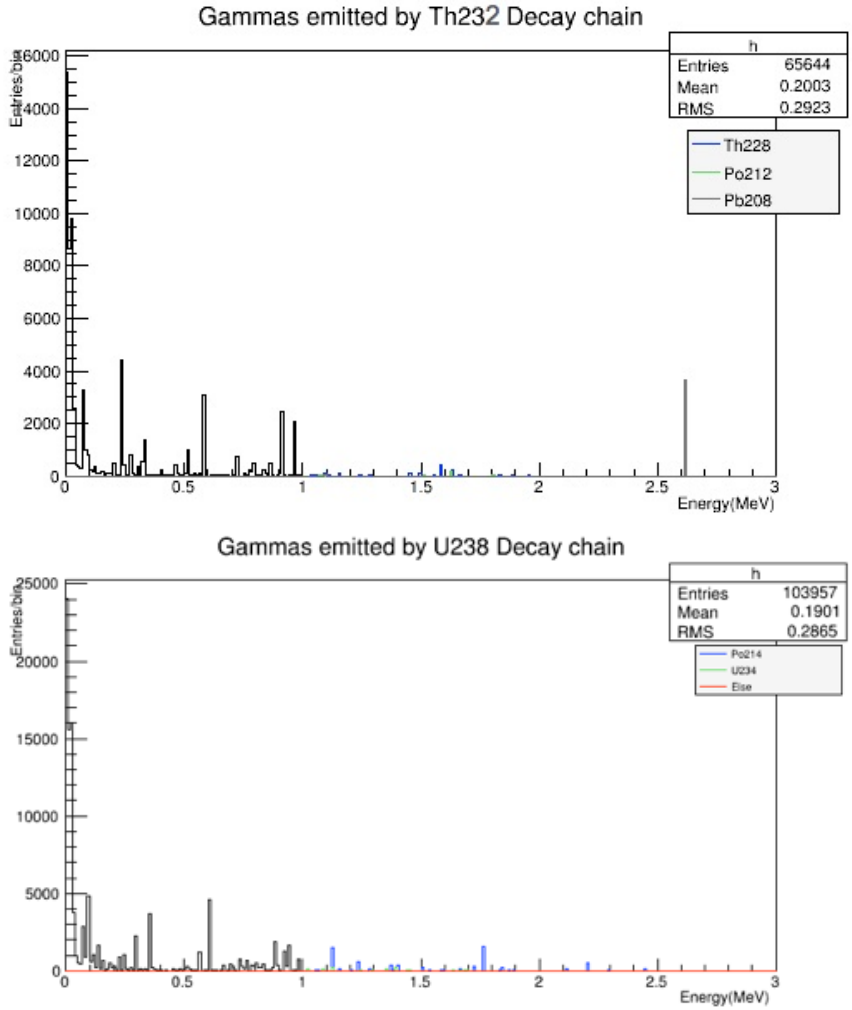

Figure 5.6: Gammas produced by the radioactive decays of the natural ^{232}Th (top) and ^{238}U (bottom) chains. In the Thorium chain, de-excitation gammas from ^{228}Th after ^{228}Ra decay, ^{212}Pb (64.06%) after ^{212}Bi decay and ^{208}Pb (35.94%) after ^{208}Tl decay can be seen. In the Uranium chain, ^{238}U produces 1.8 MeV (32%) and 2.5MeV (65%) gammas from Internal Transition (280ns); de-excitation gammas from ^{210}Pb (0.02%) after ^{210}Tl decay; internal transition (0.125ms) gammas of 1.1 MeV from ^{206}Pb (0.00013%) after ^{206}Tl decay; de-excitation gammas from ^{234}U after ^{234}Pa decay; de-excitation gammas from ^{214}Po (99.98%) after ^{214}Bi decay. Times an ratios from [151]

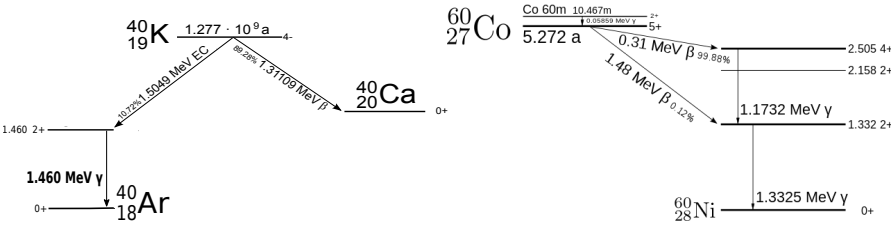

Figure 5.7: Decay radiation scheme for the isotopes potassium 40 (left) and cobalt 60 (right).

^{60}Co and 1.46 MeV gamma from ^{40}K), its contribution could make difficult the measurement of the half-life. Therefore the minimization of materials with high ^{40}K and ^{60}Co or the selection of cleaner materials has been done up to some point although those are not relevant for $\beta\beta0\nu$ searches.

The Compton distribution from ^{40}K and ^{60}Co can hide the $\beta\beta2\nu$ continuum at only moderate activities. Therefore an optimization of the low boundary of the ROI to establish the exact value is useful, because of the higher the value the more efficient in simulating time (only write information of interactions above this energy). On the other hand, the higher the threshold —since we try to avoid low energy backgrounds— the less $\beta\beta2\nu$ events. Therefore an optimum value where to establish the low energy threshold as a balance of both has to be decided. In Figure 5.6 can be see that below 1 MeV the backgrounds begin to rise to the low energy region. However in Figure 5.8 can be seen that establishing the lower threshold at 1 MeV give only the 40% of the $\beta\beta2\nu$ signal. Accordingly, a compromise of increasing the signal efficiency up to 70% lowering the cut to 0.7 MeV, where the ^{232}Th and ^{238}U backgrounds are still moderate, was determined.

5.3.3 Radon contribution to the background.

Most of the high energy radioactive gammas described above can be attenuated by the nesting shielding system (e.g. the natural contamination from the laboratory rock walls is absorbed by the lead shielding down to 4 orders of magnitude). Nevertheless, a gaseous material that

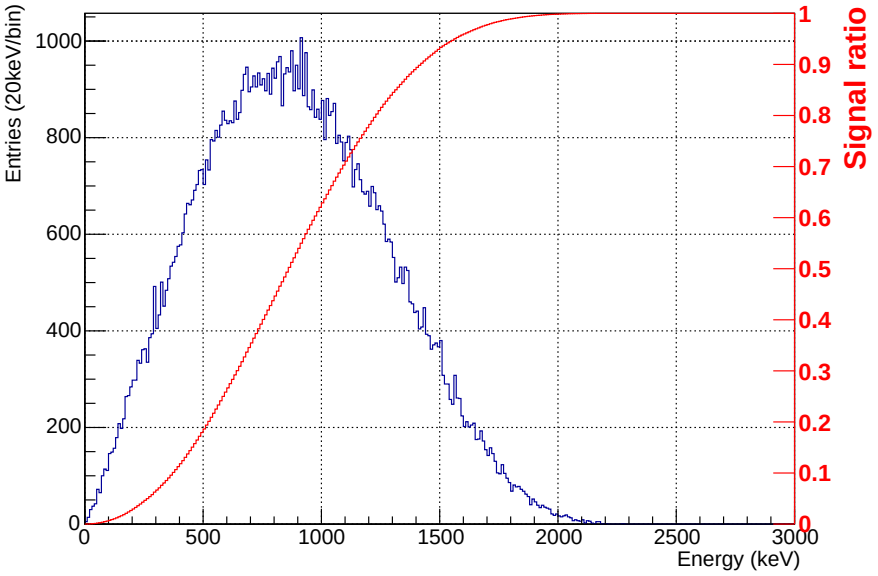

Figure 5.8: ^{136}Xe double beta decay with neutrinos energy spectrum (blue histogram) and the percentage of the signal ratio as function of the energy (red curve).

can diffuse into anything is more complicated to shield. Radon is a radioactive noble gas that use to be an headache for all the underground rare events searches. It is an intermediated decay product of the uranium and thorium series. As noble gas, is not very reactive and can diffuse easily, infiltrating into the active region of the detectors and their daughters (polonium after the alpha decay) tend to adhere to surfaces because of electrostatic charge. Two radon isotopes arise from the ^{232}Th and ^{238}U chains, the ^{220}Rn and the ^{222}Rn with 55 seconds and 3.8 days of half-life. The difference between their half-lifes makes the latter much more abundant. Then, the ^{222}Rn, becomes an extra contribution to the ^{214}Bi activity in the detector.Its measurement *in situ* resulted in 66 Bq m^{-3} of airborne radon (^{222}Rn) at the LSC Hall A [154]. However, its presence near the detector can be, in principle, externally mitigated if needed § 5.5 by filtering the environmental air or flushing continuously the detector surroundings with, for example, nitrogen [150].

Moreover, radon can also emanate from detector components and be transported to the detector active volume through the gas circulation, then becoming a background impossible to shield against. However, as said before, the radon daughters tent to adhere to surfaces and so the ^{214}Bi and ^{208}Tl beta decays will occur on the edges of the active volume (mainly in the cathode due to the gas flow) allowing to discriminate their betas by fiduciallity as all the backgrounds. On the other hand, the alpha decay of the ^{220}Rn and the ^{222}Rn on the cathode can be used to monitor the concentration of radon in the detector [136, 69]. However, despite of rejecting the beta electron from the active boundaries, its previous de-excitation gammas can generate background electron tracks in the xenon active volume.

Furthermore, if the progenies decay before reaching any surface, generate a signal like electron trace inside the active. In particular, a small fraction (0.2%) of ^{214}Bi β-decays occurring in the xenon bulk will produce an electron track with energy around $Q_{\beta\beta}$. This β disintegration of ^{214}Bi is followed shortly after by the α decay of ^{214}Po ($T_{1/2} = 164$ μs). The detection of this so-called Bi-Po coincidence can be used to identify and efficiently suppress these background events and will be studied in NEW.

Therefore, even with the hard fact of the high impact of radon to the background rate, NEW will characterize its relevance and its possible attenuation with gas filtering, radon emanation trap, Bi-Po tagging... on the actual running phase.

5.3.4 Backgrounds induced by cosmic rays and their products.

As the previous background type, there is another contribution that can not be avoided with the material selection. Rare experimental searches require very clean environment in terms of matter interactions. For decades underground laboratories has been built, upgraded and gone deeper to look for these aimed facilities. Specifically the large reduction of the cosmic ray muon flux compared to that at surface laboratories is of great advantage for rare event searches.

Even locating the detector underground (LSC is 850 m under the Tobazo mountain 2450 m.w.e. [154]) not all cosmic ray flux is shielded. The LSC has measured a muon flux of $3 \times 10^{-2}\mathrm{m}^{-2}\mathrm{s}^{-1}$ [137]. This muons crossing the detector can be easily identified by its straight extended track with constant energy deposition in the active volume [116]. Their interaction in the environmental facilities producing electromagnetic showers and these filling up the detector could be, in principle, rejected by muon veto instrumentation. Anyway, these muons may produce fast neutrons and unstable nuclides in surrounding materials by muon spallation, elastic scattering on neutrons, photo-nuclear reactions from electromagnetic showers, nuclear capture of stopped muons and secondary neutron reactions [155]. The last is a detailed focus objective of low background searches, particularly of $\beta\beta0\nu$ experiments. By neutron capture the isotope used could transmute to other isotopes that could generate beta signals or even $\beta\beta$. For the ^{136}Xe $\beta\beta0\nu$ searches in EXO, the ^{137}Xe activation become 25% of their background counts in their ROI [155], showing up its relevance. In this work the possible relevance of other activations covering the $\beta\beta2\nu$ is studied.

In addition to the muon induced neutrons, although underground laboratories provide a low radioactive background environment, the rocks of the cavern are radioactive (as already known an thus the lead shielding) also in neutrons. In the case of the LSC, the neu-

tron integrated flux has been measured to be $\phi_{\mathrm{HallA}} = (3.44 \pm 0.35) \times 10^{-6} \mathrm{cm}^{-2}\mathrm{s}^{-1}$ [142]. Those neutrons as function of its energy can also produce background signals or xenon activation.
Therefore, as neutron background being a limiting factor in many rare event experiments because of the large penetrability of neutrons and the possibility of inducing background signals in the detection system, is also taken into account to backgrounds types.

A precise estimation with NEW will advance work for the future design shielding strategies and quantify sensitivity limits or systematic corrections.

5.4 Analysis of the background model

Once the isotopes under study (§ 5.3) are generated (§ 5.1.2) and its interactions through the detector geometry (§ 5.1.1) are registered, the next step in the simulation of the background model is the analysis of the physics process and detector response.

Within NEXUS simulation, a first preselection cut is done for time/memory saving. Only those events with total energy deposited in the active volume above 0.6 MeV are stored. This loose low boundary avoids edge effects when analyzing data with the low energy threshold at 0.7 MeV.

The event selection then goes through a series of filters on which is based the **Fast-Simulation** analysis:

1. A *fiducial* cut :
   $\beta\beta$ events are produced in the active volume, while background events come from the materials enclosing it. Therefore, only those events that are fully contained in an inner fiducial volume are selected. Energy deposition (*hits*) greater than 10 keV in the 2 cm region from the active walls are rejected. This cut eliminates the background events with charged particles entering the active volume.

2. Energy *smearing* :
   Detection and reconstruction effects are taken into account by smearing the event true energy deposited to the 1% FWHM

resolution. Even-though has been demonstrated that can be up to 0.5-0.7% with the prototypes [106, 117], before commissioning the NEW detector the use of 1% FWHM was a conservative approach. After demonstrating the energy resolution of NEW this will be updated.

3. *ROI* energy cut:
   A more precise cut on the energy of the events is made selecting only those that enter in our region of interest (ROI) window. That window is defined before in order to maximize the sensitivity and change among the 2ν or the 0ν analysis. For the NEW background model analysis has been set to 0.7 MeV - 2.7 MeV. Therefore those events with smeared energy outside the ROI are rejected.

4. *Track reconstruction*:
   One of the features of NEXT is the ability to reconstruct event topology. The simulated events are reconstructed with the *voxelization* algorithm (it looks for a finite space volume with an energy deposition different from zero) to 1 cm^3 3D hits. Afterward those hits are interconnected forming the track produced by the particle in the detector.

5. *Topological (1 track)* cut:
   Only events containing a single reconstructed track are accepted. It is based on the high selection efficiency for signal events (70% are single track) and high rejection of backgrounds (90% have 2 or more tracks)[140, 77].

6. *Topological (2 blobs)* cut:
   Those tracks are analyzed comparing their associated end *blob* (high energy deposition in a small region at the track end, compatible with the Bragg peak at the stopping points of the candidate decay electrons). The energy of a blob candidate is defined by summing all the energy contained within a volume of 20 mm radius from the reconstructed track extreme and a minimum required energy of 400 keV. The event tracks with one *blob* (background-like) are discarded and those with two *blobs* (signal-like) at the ends are selected [140, 77].

In Figure 5.9 can be seen the event rejection factor per source as function of the selection cut. Two different source of backgrounds are shown to compare the efficiency as function of its origin. ^{208}Tl from the most internal source —the dice boards— and from the most external element —the shielding lead— can be seen. Also the selection efficiency for the $\beta\beta2\nu$ events is referred.

This analysis gives, as an event selection filter, the rejection factors for each source as function of its origin (how well shielded are), the rejection potential of each filter and the total rejection factors (Figure 5.10).

At the end of the analysis an energy distribution for each event type generated is obtained. This can be normalized and used as a probability density function (*pdf*) which weighted with the measured activity of each source gives the total contribution per event type. Just because of technical resources, the event simulation was split in several threads for simulation and analysis and then summed to have one pdf per isotope and source.

On one hand, the rejection factors of each background (isotope/source) per its activity measured (§ 5.2), taking into account the total amount of material (number of pieces, mass or volume), can be computed. On the other hand, applying the same analysis to the signal events ($\beta\beta2\nu$) with its rejection factors and multiplying per its activity (the EXO measured half-life of ^{136}Xe has been used [69]), on its total mass as for the backgrounds. This gives the overall picture of signal ($\beta\beta2\nu$) to noise (backgrounds) ratio used for discrimination of materials and/or designs, as well as the prediction of the total contribution. The next section uses this picture to describe some feedbacks from the MC results to the real detector configuration and the projected performance of NEW.

5.5 Background model results: NEW prospects

The background contribution with respect to the signal ($\beta\beta2\nu$) in NEW is the result of the virtual modeling, physics process simulation, real material activity measurement and counterbalance of its performance. The model developed allow the consistency or suitability check of each modification under study. The Figure 5.17 shows the standard overall picture of the background model of NEW. It was conceived to identify

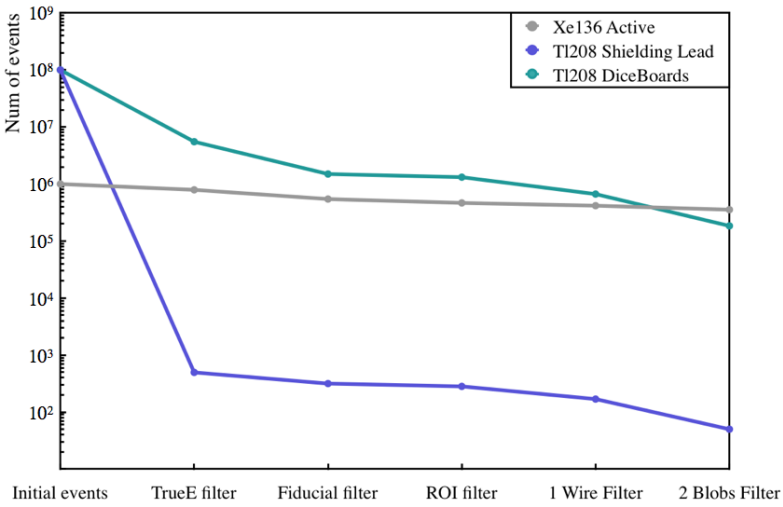

Figure 5.9: Variation of number of events as function of the analysis filters for two backgrounds (the most internal and the external) and for $\beta\beta2\nu$ events.

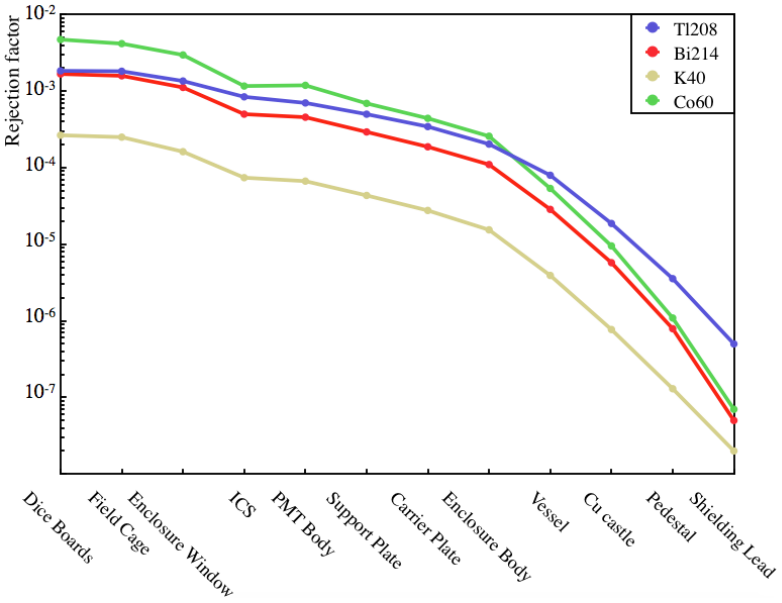

Figure 5.10: Rejection factors as function of the origin of the background sources differentiated by isotope.

possible drawbacks as well as to evaluate the ability to measure the ^{136}Xe $\beta\beta2\nu$ half-life.

The different issues identified, their description and prospects to reduce their impact or elimination are discussed here.

Radon for NEXT

As has been detailed in § 5.3 that radon is a sensible background for NEXT. With the measured activity of airborne radon (^{222}Rn) at the LSC Hall A, 66 Bq m^{-3}, its contribution has been evaluated with an specific study. Figure 5.11 shows the radon activity compared with the signal after analysis for two models: as the radon progenies attaches to surfaces the most simple model is to assign the radon contribution to decays on the vessel surface with a virtual surrounding tube (left) and an elaborate model considering that the radon adhere to the vessel and lead castle surfaces proportionally to is exposed surface (right). The last also add a passive veto system, an extra copper shielding (copper castle) that attenuates the radon contribution one order of magnitude. Nevertheless both models show that this scenario would represent an intolerably high background source for the NEXT experiment. Therefore the requirement of an active veto system that reduces the airborne radon levels up to 3 orders of magnitude is needed.

To fulfill the requirements, mitigation and the monitoring plans for radon-induced backgrounds, a radon abatement system by ATEKO has been purchased by the LSC. The system was installed in Hall A in December 2015 (see Figure 5.12). The system should be capable of delivering air to NEXT with a maximum ^{222}Rn content of about 1 mBq/m^3 [154], reducing 4–5 orders of magnitude the ^{222}Rn content at the detector surroundings. With this radon contamination reduction, it drops to a negligible contribution to the overall background budget.

Airborne radon is no the only problematic source, radon can also emanate from detector components and diffuse to the active volume through the gas system [140]. As will be shown in Figure 6.16, its control and reduction —if possible— will be studied in NEW in order to evaluate its impact for the NEXT-100 sensitivity [156, 157].

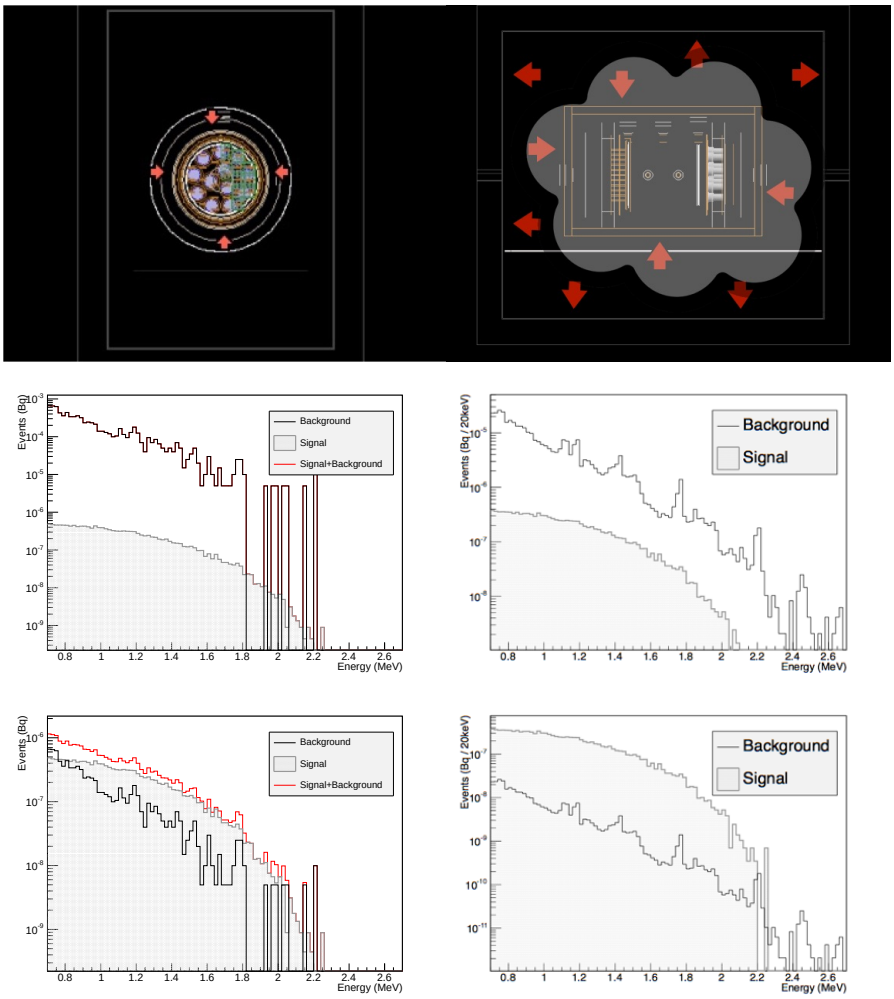

Figure 5.11: (Top) Two simulated models of radon contribution: virtual radon tube surrounding the detector (left) and radon attached to the surfaces proportionally to their area (right). (Center) Radon-induced background in NEW assuming the nominal activity measured in the air of the LSC (66 Bq/m^3 at Hall A). (Bottom) Radon-induced background in NEW reducing by three orders of magnitude the concentration of ^{222}Rn in the air.

Figure 5.12: Radon abatement system installed at the LSC.

Copper manufacturer

At the design stage two copper types were considered to be used, the CuA1 (OFHC radiopure) for the barrier of the ICS and the CuC1 (less radiopure) for the copper endcaps. The results showed too high level of radioactivity from the CuC1 requiring the usage of the best copper.

SiPM sensors

The evaluation of the measured activity of the SiPM sensors depicted for DEMO operation result in a non tolerable contribution, mainly due to the amount of total SiPMs and its location impossible to shield. This drive the change from the Hamamatsu S10362-11-050P [122] SiPMs, to the SensL MicroFC-10035-SMT-GP (1×1 mm^2) [125] SiPMs. The latest also result in lower dark current, improving their calibration (see § 6.1.2).

PMT bases

The front end electronics for the PMTs is placed at the end of the PMT itself. The base where the PMT is pinned is home made to match

the NEXT specifications, that allow us not only tune the electronic features but also the capability to choose its components. Being a element as exposed as the PMTs, it has no shielding and practically free path to the active volume, its background contamination can be extremely important regarding the usage of commercial components to fabricate them: substrate, glue, capacitors, resistor, welding and pins. The evaluation of a huge range of potential components for the base fabrication has been carried out to guide the final design [109, 144].

Anode quartz plate

The evaluation of the NEW technological approach of an anode quartz for the field cage in terms of background contribution was needed beforehand. It results in a tolerable background addition, well below other components with the caveat of using an activity of quartz from literature.

Shielding structure paint

The radioassay material program brought up an alert on the activity of the paint used for protecting the steel structure of the lead castle. The first simple evaluation show an intolerable contribution to the NEXT-100 radioactive budget, thus requiring a more detailed analysis. In order to enlighten the suitability of an already built component a careful simulation of the critical structures for the background contribution was done. In Figure 5.13 the simulation of those frames not shielded by the lead of the shielding structure can be seen. The rate for NEXT-100 is to high ($\sim$20% of the total contribution to ^{208}Tl and $\sim$ 10% of ^{214}Bi in the $\beta\beta0\nu$ region [158]) although for the $\beta\beta2\nu$ measurement with NEW could be tolerable due to the other backgrounds. For the NEW detector in order to face this problem and the impossibility of disassembling the whole castle to remove the paint while NEW is already built, an extra copper shielding will be implemented. This extra copper shielding surrounding the vessel will be made out of the same copper bars of the ICS but larger. The sum of the 6 cm of the ICS and the 6 cm of the copper castle will give the 12 cm of shielding that are planed for NEXT-100. Accordingly, the background contribution from the

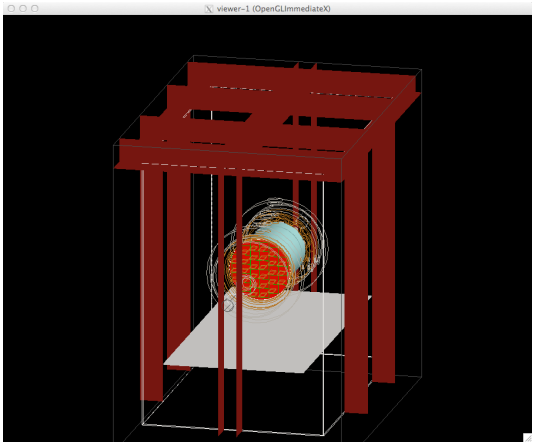

Figure 5.13: Geant4 simulation of the shielding structure of the lead castle.

paint will be reduced in the $\beta\beta2\nu$ region below the other background contributions for NEW.

Cosmogenic backgrounds

Two detailed studies have been developed to compute the relevance of the cosmogenic induced backgrounds: muon activity and neutron activity. Neutrons an muons have been simulated as described in § 5.1.2. Their direct interaction in the active volume as well as the induced products by their interaction in the detector surroundings that deposit energy in the active volume has been studied. Following the same procedure as in the background from the materials components (§ 5.2) an evaluation of the activity has to be taken as an input. Therefore, the characterization of the LSC neutron activity [142] and muon activity [137] has been used.

We separate here two types of interactions, electromagnetic interactions occurring in the first 5 ms after the incident particle; and delayed (10^4 ms) interactions that come from the Xe activated β-decays. There are also interactions around 10^{12} ms (mainly from ^{137}Ba) that correspond to half-lifes of more than 30 years, out of our time scale and

therefore neglected in the analysis. Then backgrounds studies of the two processes must be carried out separately as they belong to different time scale events.

The earlier events coming from the muon activity can be vetoed by muon tagger panels outside the detector identifying the background events produced after an incident muon. Although high energy neutrons could also lead to electromagnetic backgrounds (4.14×10^{-6} Bq, well below the natural radioactive backgrounds), its reduction could be done with a passive veto explained latter. In Figure 5.14 can be seen the electromagnetic interactions that mimic the signal induced by neutron activity.

It is remarkable the pair production peak emerging at 1.202 MeV, which comes from the deuteron decay (2.22 MeV) created by an hydrogen neutron capture. Although being a natural possibility to evaluate the neutron electromagnetic activity as well as the topology capabilities (as explained in § 5.3.2) its low activity below other backgrounds and its coincidence with the 1.173 MeV ^{60}Co gamma make it difficult. Nevertheless, as can be seen in Figure 5.14, a detailed analysis of the NEXT-100 ROI (2.3-2.6 MeV) will be interesting to asset the actual activity and the necessity of a passive neutron veto.

Calculations of shielding the neutrons by 20 cm of borated polyethylene gives a reduction of two orders of magnitude. These studies addresses the possibility of an upgrade of NEW to use a neutron shielding and a muon tagger [159] to evaluate the specific shielding implementation for NEXT-100.

Concerning the delayed events, the incoming neutrons from the natural radioactivity and neutrons produced by cosmic muons can produce neutron activation of ^{136}Xe. This neutron capture can produce gammas from nuclear de-excitation and decay radiation from a generated radionuclide. EXO has observed, for instance, that most of the neutron induced β-decay came from the ^{137}Xe activation [155]. In our case, activation of the ^{137}Xe, ^{135}Xe, ^{133}Xe, ^{132}Xe, ^{131}Xe and ^{130}Xe isotopes have been observed. Only the ^{137}Xe, ^{135}Xe and ^{132}Xe radiate gammas of energies inside 0.7-2.7 MeV region. The ^{132}Xe is stable. It has four de-excitation gammas in coincidence of energy below 7.7 MeV what

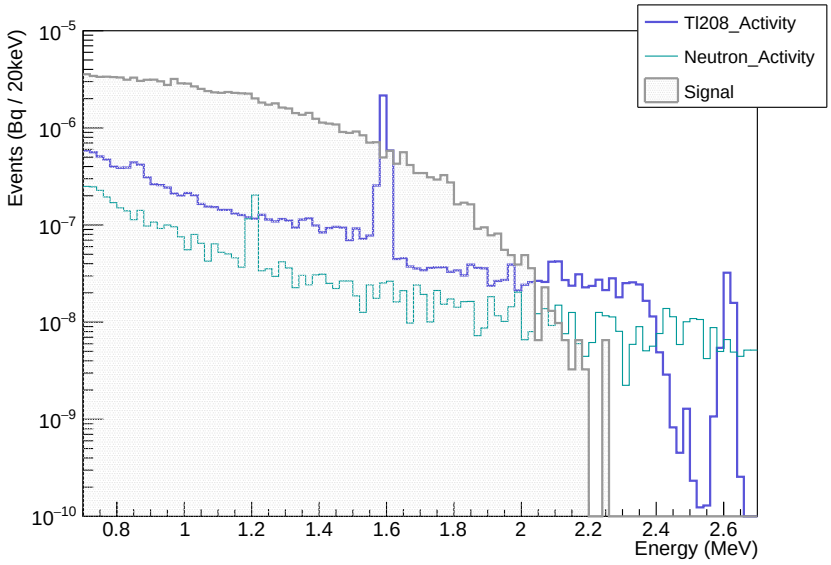

Figure 5.14: Neutron induced activity compared with ^{208}Tl background and $\beta\beta2\nu$ signal.

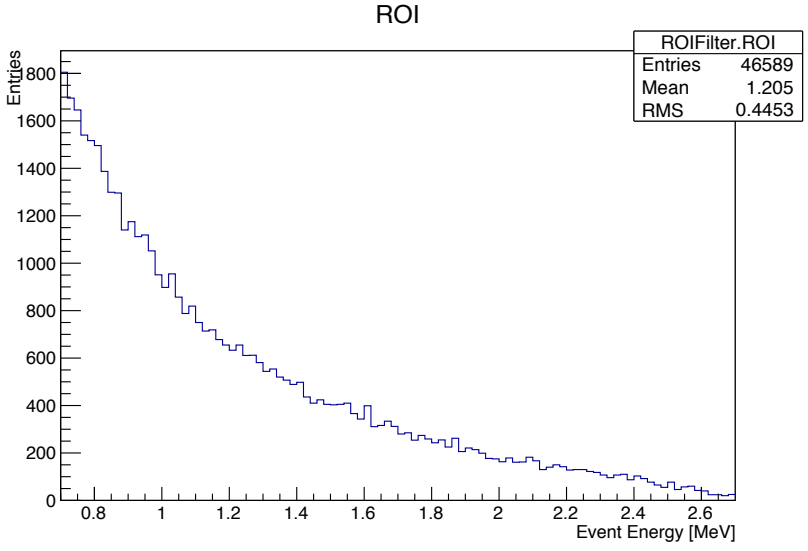

Figure 5.15: ^{137}Xe neutron activated decay events as function of its energy deposition.

makes the possibility of a $\beta\beta2\nu$ fake signal insignificant. The ^{135}Xe excited state after activation radiate gammas from internal transition below 0.7 MeV. If the ground state is produced in the activation, it beta decays 100% with a half-life of 10^7 ms and 300 keV gamma energy. Its ^{135}Cs daughter emits two de-excitation gammas of 787 keV and 846 keV. Their low energy and their production rate makes them fall bellow the crowded low background region population with a 1.2×10^{-8} Bq contribution, despite that due to its active volume origin only a 1.3×10^{-2} analysis rejection factor is achieved. On the other hand the ^{137}Xe activation produces gammas an betas that deposit energy all along our energy window (see Figure 5.15). Nevertheless, its production rate and the analysis cuts (4.66×10^{-2} rejection factor, suffer the same as previous case) makes its total contribution become 3.27×10^{-7} Bq. This is one order of magnitude larger than the previous but still bellow the natural radioactive contributions.

Next section summarizes the background impact of the NEW model. Although the issues described above, some achievable considerations have been done for the final contribution based on the results: the radon is assumed to be reduced by the abatement system to negligible contribution; the shielding structure paint is assumed to be attenuated by the copper castle and therefore the copper castle contribution evaluated; regarding the cosmogenic backgrounds, given their low contribution and the possibility to be shielded neither are shown.

5.5.1 Predicted background rate

The Table 5.3 summarizes the contributions of each element taken into account the overall background rate separated by isotope. It is also shown its relative percentage importance and the total relevance.

The Figure 5.16 shows the absolute background contribution per isotope for each component. There can be seen how the low energy backgrounds (^{60}Co from the vessel, PMT, ICS and field cage; ^{40}K from the dice boards and field cage) dominate the rate by an order of magnitude. Regarding the ^{214}Bi and ^{208}Tl, the vessel stand above the remainder.

The Figure 5.17 shows the energy spectra of signal ($\beta\beta2\nu$) and

	^{208}Tl (Bq)		^{214}Bi (Bq)		^{40}K (Bq)		^{60}Co (Bq)		Total (Bq)	
Dice Boards	5.1815E-07	3.92%	3.2931E-06	14.07%	1.0788E-04	76.08%	8.0014E-07	0.29%	1.1249E-04	24.84%
Anode quartz	9.3935E-08	0.71%	5.2793E-07	2.26%	2.5906E-07	0.18%	0.0000E+00	0.00%	8.8092E-07	0.19%
Field Cage	1.4525E-06	10.98%	1.9906E-06	8.51%	1.8816E-05	13.27%	1.8362E-05	6.69%	4.0622E-05	8.97%
ICS	7.4657E-07	5.64%	3.6946E-06	15.79%	2.8266E-06	1.99%	2.9407E-05	10.72%	3.6675E-05	8.10%
PMT Body	1.5996E-06	12.09%	1.9182E-06	8.20%	9.4589E-06	6.67%	5.3356E-05	19.44%	6.6332E-05	14.65%
Vessel	7.5895E-06	57.37%	8.4738E-06	36.21%	3.0341E-07	0.21%	1.5232E-04	55.50%	1.6868E-04	37.25%
Carrier Plate	1.0662E-07	0.81%	4.8403E-07	2.07%	3.6871E-07	0.26%	3.8931E-06	1.42%	4.8524E-06	1.07%
Support Plate	2.1819E-07	1.65%	1.0664E-06	4.56%	8.1606E-07	0.58%	8.5958E-06	3.13%	1.0697E-05	2.36%
Enclosure Body	1.4411E-08	0.11%	6.4968E-08	0.28%	4.7098E-08	0.03%	5.2009E-07	0.19%	6.4657E-07	0.14%
Enclosure Window	3.2526E-07	2.46%	1.2056E-06	5.15%	7.7586E-07	0.55%	3.7841E-06	1.38%	6.0907E-06	1.34%
Shielding Lead	2.6504E-07	2.00%	2.7107E-07	1.16%	3.8724E-08	0.03%	8.7442E-08	0.03%	6.6228E-07	0.15%
Pedestal	1.8916E-07	1.43%	1.3082E-07	0.56%	5.6160E-09	0.00%	1.7266E-06	0.63%	2.0522E-06	0.45%
Cu castle	1.0924E-07	0.83%	2.7990E-07	1.20%	1.9366E-07	0.14%	1.5834E-06	0.58%	2.1662E-06	0.48%
TOTAL	1.32E-05		2.34E-05		1.42E-04		2.74E-04		4.5285E-04	

Table 5.3: Background contribution and relative importance of each detector component to the total background rate after shielding and analysis.

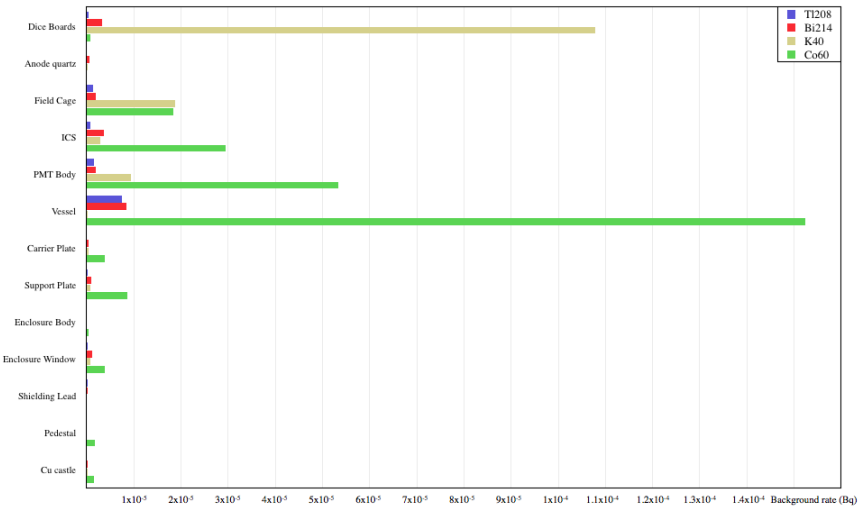

Figure 5.16: Total background rate per isotope for each component of the NEW background model.

background in the energy region between 0.7 and 2.7 MeV with the budget aforementioned. Several peaks are clearly visible in the background spectrum. From left to right: ^{60}Co gamma lines at 1.173 MeV and 1.332 MeV; ^{40}K gamma line at 1.460 MeV; double-escape peak of ^{208}Tl at 1.6 MeV; and ^{208}Tl gamma line at 2.615 MeV. The lower part of the energy spectrum is, therefore, dominated by activity from^{60}Co and ^{40}K.

The model is constructed from separated source components contribution to each isotope considered. The Figure 5.18 (^{214}Bi), Figure 5.19 (^{208}Tl), Figure 5.20 (^{40}K) and Figure 5.21 (^{60}Co) can show the source contribution per isotope identifying the most relevant elements of the detector in terms of background emitters. There can be seen that the contribution to the total ^{214}Bi is almost in the same order for all of the components, although the vessel stands higher. In the ^{208}Tl case, is clearly visible the vessel standing out one order of magnitude higher than the others. The vessel being the most relevant contribution, could be due to the limited attenuation of its activity by the moderate width of copper in the barrel. Regarding the ^{40}K contribution it is clear

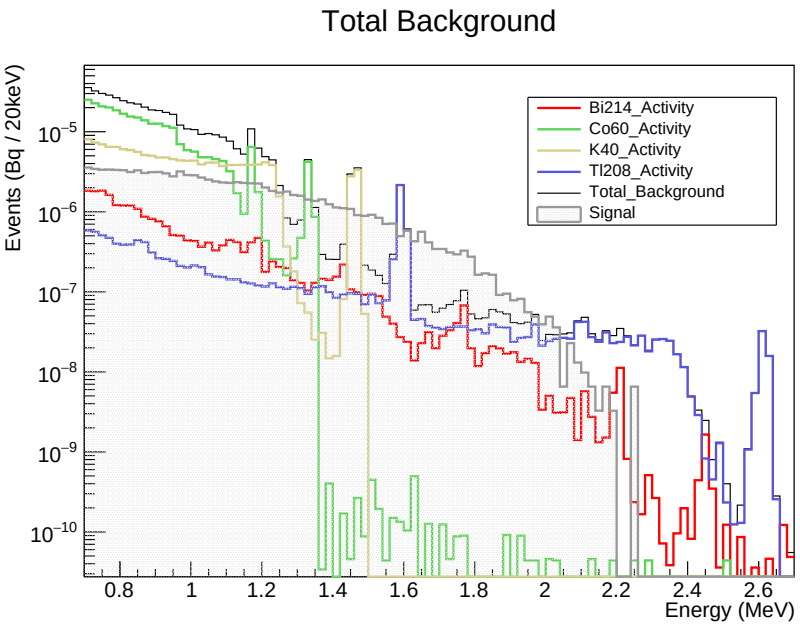

Figure 5.17: Background spectra differentiated by source and compared to the $\beta\beta2\nu$ signal rate. Here, the gamma lines from ^{60}Co (1.173 MeV and 1.332 MeV), ^{40}K (1.460 MeV) and ^{208}Tl (1.6 MeV and 2.615 MeV) can be easily identified. Also the 2.204 MeV and 2.447 MeV gammas from ^{214}Bi can be glimpsed.

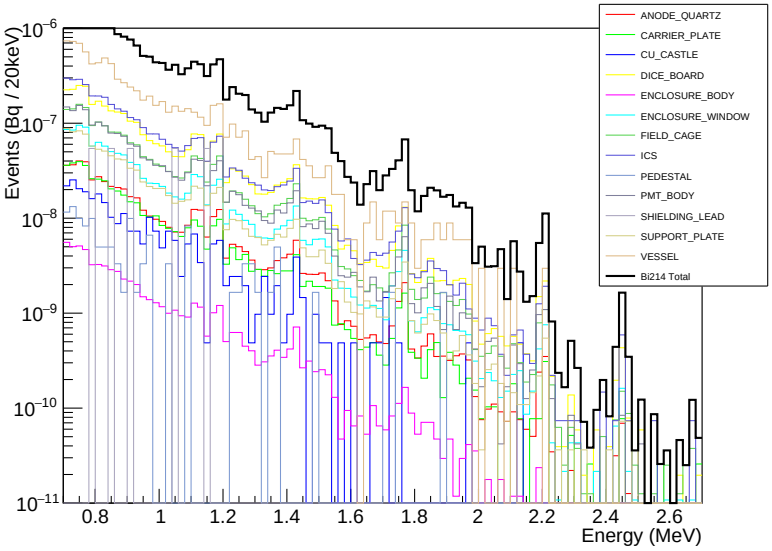

Figure 5.18: ^{214}Bi sources of background. It is shown the contribution of each component.

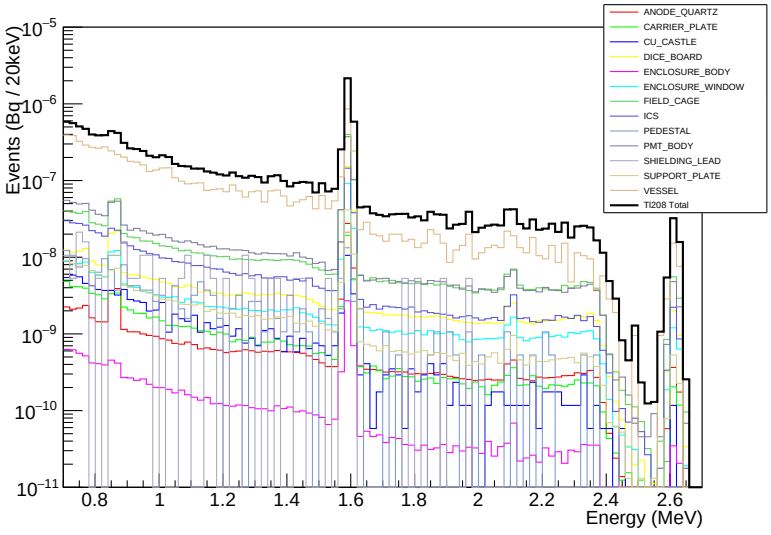

Figure 5.19: ^{208}Tl sources of background. It is shown the contribution of each component.

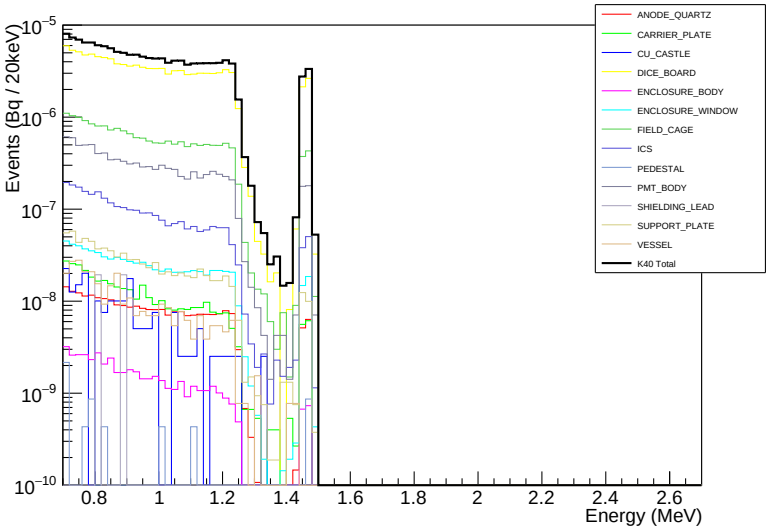

Figure 5.20: ^{40}K sources of background. It is shown the contribution of each component.

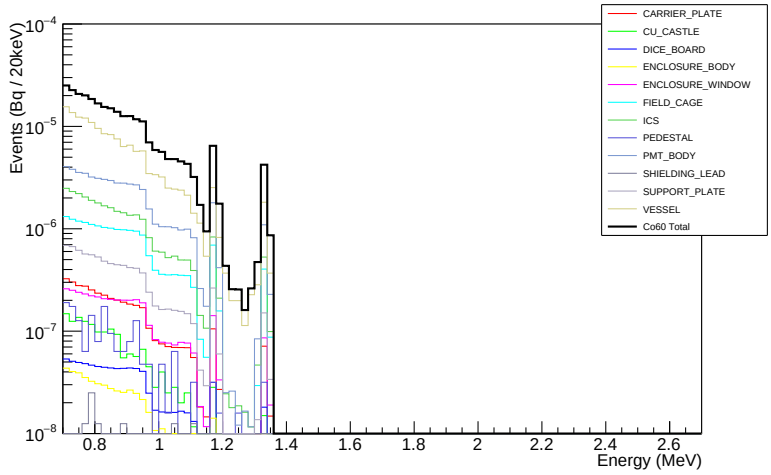

Figure 5.21: ^{60}Co sources of background. It is shown the contribution of each component.

the contribution from the dice boards (the adhesive from the flexible circuits substrate) an order of magnitude higher than the next three components (field cage, PMTs and ICS) while the remainders are two orders of magnitude below. The ^{60}Co contribution is more distributed, being the most relevant (vessel, PMTs, ICS and field cage) within the same order of magnitude.

The discrimination of backgrounds as function of its source origin will be also studied in NEW data with the positioning of the background events in the vetoed regions. Therefore this information is useful for their identification.

5.5.2 Predicted sensitivity

One of the objectives of the NEW detector is the validation of the background model comparing the estimated total contribution energy spectrum (Figure 5.17) with the data. This will allow to check the background rate predictions for NEXT–100.

Another of the objectives, is the measurement of the $\beta\beta2\nu$ half-life, if posible with precision, to show the capabilities. Therefore, simulations of this measurement has been also carried out by the Collaboration.

The background model works as a tool to estimate possible experiments given the signal to noise ratio. Hence the evaluation of the performance by simulating a number of experiments that follow the predicted rate (*pdf*) of the model as function of time, allow to get a large data sample. Multiple experiments instead of using a generated *pdf* are used in order to simulate the statistical fluctuations of the Poissonian distribution. This data sample can be fitted using the individual training samples (pdf_i) to evaluate the scale factors per energy bin and then the estimated half-life.

$$Data_{exp} = \sum_i n_i \cdot pdf_i \tag{5.1}$$

If this is done increasing the exposure, for each fitted parameter over the error a Poissonian tendency of $\sqrt{\mathrm{n}}$ as can be seen in Figure 5.22. The Collaboration estimate that a NEW enriched ^{136}Xe run of about 90 days accumulated exposure should be sufficient to extract a non-zero $\beta\beta2\nu$ component from the energy spectrum of $\beta\beta$ candidate events with a significance of about 5 sigmas.

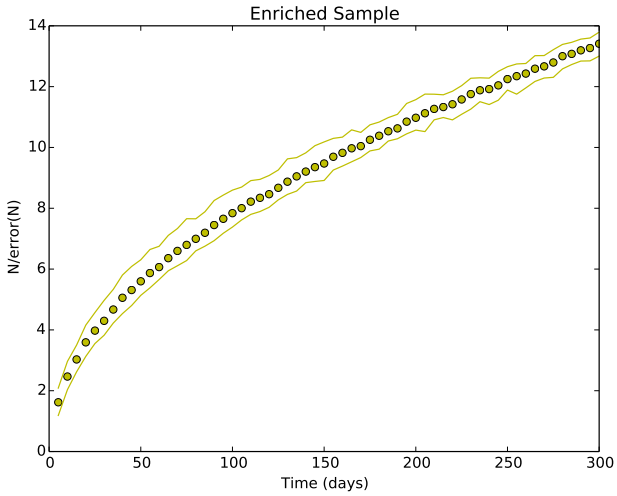

Figure 5.22: Expected significance (in number of sigmas) of the $\beta\beta2\nu$ measurement in NEW as a function of exposure. The markers indicate the average sensitivity, and the band the expected uncertainty ($\pm1\sigma$) [160].

"You shall have your sunset. I shall command it. But I shall wait, according to my science of government, until conditions are favorable."

Antoine de Saint Exupéry
"Le Petit Prince"

Chapter 6

Calibration of the NEW detector

As part of the commissioning of the NEW detector, its calibration and first data are discussed here. In the first section (§ 6.1) the calibration of the sensors is described with emphasis on the PMT calibration method developed. The main section § 6.2 is devoted to the novel geometrical corrections using low energy source calibration ($^{83}Kr^{m}$). The analysis developed with Monte Carlo data simulation is discussed with the detail to later apply to the first NEW detector data. During the commissioning, test of the gas system performance in terms of cleanness and purification, as well as tests of the high voltage have been performed (§ 6.2.2). This limits the available data as well as the quality but gives some interesting clues to understand the detector performance instead. These analysis results are described in § 6.2.3.

6.1 Sensor calibration of NEW

The NEW detector, follows the NEXT detector concept described in Chapter 3 and has two separated optimized readout planes, one made of PMTs for calorimetry and the other of SiPMs for tracking. In this section the different calibration methods used for each readout are described.

6.1.1 Calibration of the calorimetry readout

The calibration of the energy plane sensors is extremely important to optimize the energy resolution of the detector.

As explained in Chapter 3, the NEXT concept uses photomultiplier tubes (PMTs) as the optical readout to measure the energy of an event. At the PMT, optical photons that arrive to the photosensitive cathode behind the quartz window extracts electrons that drifts to the first dynode under the influence of a voltage potential difference given by the power supply. A chain of dynodes creates an avalanche, multiplying the number of electrons and thus giving an amplified current. The PMT acts only as a counter triggered by a photon and the signal can be amplified by increasing the supply voltage which increases the number of electrons per avalanche (gain). This behavior persist until the the voltage is too high and the number of electrons produced is no longer linear with respect to the number of detected photons. This linearity voltage regime is usually indicated by the PMT supplier but a double check for operation and linearity has been made for all the PMTs. Once the working regime is established, being sure that the signal recorded by the PMT is proportional to the trigger signal, one would like to know what is this proportionality constant to be able to determine how large the trigger signal will be. This is done by measuring and characterizing the signal response for a given operational voltage to a well know trigger. In the NEXT case, as the sensor measures optical photons, one would like to know how many photons are measured and which is the amount of energy carried by them.

The former is done measuring the signal produced by the amplification of the PMT as the response to one incoming photon. There are various methods which could be used to calibrate the sensors, most of which use the response to low level illumination. Using the scintillation photons themselves [161] which has the complication of producing only a few photons per event, using thermally generated electrons (dark current) [123] or by using a controlled light source at a wavelength similar to that of the photons that will be detected by the sensor under normal operating conditions.

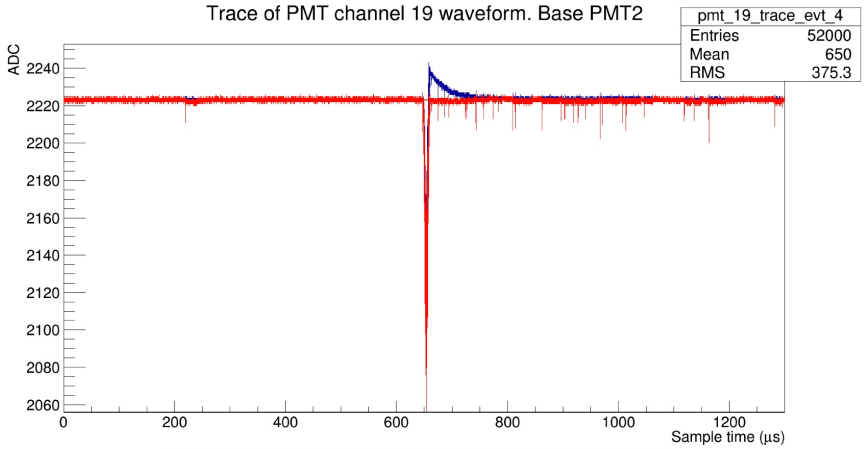

Figure 6.1: PMT waveform in ADC counts with time. At the center the S2 triggered signal can be seen preceded by a very little S1. In blue it is registered the raw differential signal and in red the online deconvoluted signal.

The use of LEDs for calibration was proven to be useful and debugged at the DEMO phase (Appendix 7). Using a 400 nm LED, close enough to the wavelength shifted Xe scintillation given the price and instabilities of VUV LEDs, in a low emitting range to provide one photon per pulse (single photoelectron response); the proportionality constant (ADC per photoelectron) can be established for a given working voltage of the PMT. Due to the statistical fluctuations of ensuring the single photon emission, it enters in a Poisson regime where most of the times nothing is read by the sensors, sometimes one photon reach the sensor and from time to time more than one photon is recorded. For this reason, not only the equivalence of one photon to ADC had to be measured (fit the position peak where one photon events are stack at the histogram) but the correlation between the multiple photons recorded (0, 1, 2, ..., N). This gives us a robust method to convert the digital signal of the readout (ADCs, see Figure 6.1) to the physical signal (photoelectrons).

From a technical point of view, if one has the possibility to choose the design of the calibration system, the more homogeneous the source the better. LEDs are the most extended, cheapest and simplest way to calibrate sensors but have some issues. The exact amount of energy released is not constant in time, it has some variations and it gets harder going to shorter wavelengths. Also the electronics to control the power can introduce noise. But one of the most important thing that we learned prototyping is the relevance of the spacial distribution. It is important to cover the total area homogeneously without changing to much the functionality of the detector or interfering the signal of the sensors due to crosstalk with the LED power (see Appendix 7). Therefore in NEW, one LED per DICE board is mounted on the tracking plane (see Figure 4.6) shooting towards the PMTs planar, minimizing the solid angle geometric aberrations. The LEDs are electronically controlled by the same slow control of the SiPMs and powered by the same supplies, allowing usage with the SiPMs switched off. They are pulsed for short intervals ($\sim$ 25 ns) multiple times for every trigger. Triggering read-out so that multiple regularly spaced LED pulses are captured per trigger, allow for high statistics calibration. Integrating the resulting digital trace for each PMT in the regions correlated with the LED pulses gives the low light spectrum for each channel while integrating in anti-correlation with the LED pulses gives a robust 'no light' spectrum.

The histogram of the integrated signal is then fitted to a basic PMT response function to extract the relevant parameters:

$$F(x) = N_0(P(0;\mu)G(x, x_p, \sigma_p) + \sum_{n=1}^{N_{max}} P(n;\mu)G(x, nx_1 - x_p, \sqrt{n\sigma_1^2 + \sigma_p^2}), \tag{6.1}$$

where N_0 is a global normalization, $P(n;\mu)$ is the Poisson detection probability of n photoelectrons given mean μ (a combination of LED flux, acceptance and sensor quantum efficiency), x_p and σ_p are the pedestal centroid and sigma, x_1 and σ_1 are the 1-photoelectron response gain (G) and sigma, and N_{max} is the maximum number of photoelectrons considered in the fit. Responses are modeled as Gaussians. N_{max} was determined for each fit as that of the highest n which would yield a Gaussian with integral >= 100 ADC. The fit procedure was devel-

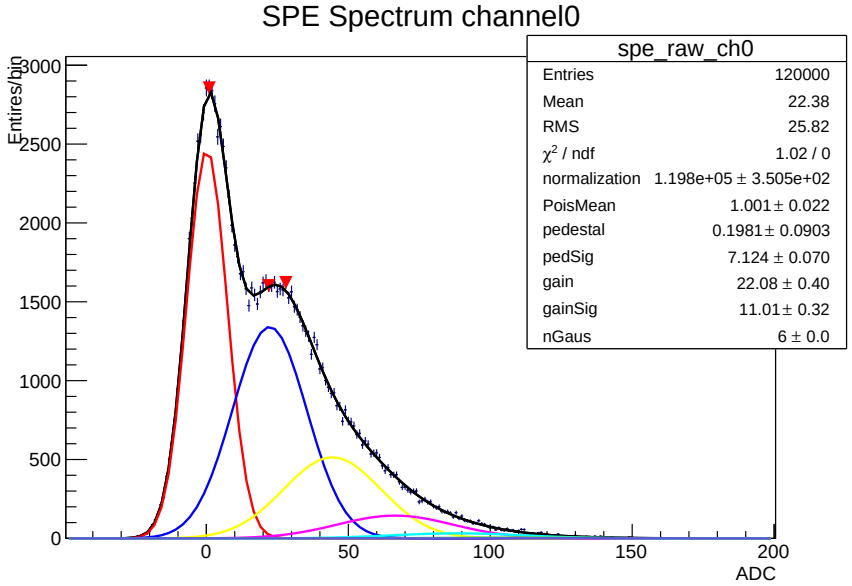

Figure 6.2: Single photo-electron calibration total response spectra of a central PMT in NEW (blue points are data measurement and black line the total fit). In red can be seen the pedestal fit component corresponding to no photon detection whereas the contribution to the total fit by the 1, 2, 3, 4... photons response are shown in blue, yellow, magenta, cyan... respectively.

oped in the DEMO phase (see Appendix 7) and improved here. The Figure 6.2 shows an example of the calibration of one inner ring PMT in NEW. There can clearly be seen the pedestal peak and the single photoelectron peak.

The readout of the PMT signal is done by a home made base design with some advantages and some drawbacks. One of these, is the distortion of the signal done by the capacitors to obtain a differential signal. The electronics makes a derivative of the physical signal to send it with more stability but it introduces a non-physical negative component in the signal. This implies some previous signal treatment for

de-convoluting the real signal and the electronic induced signal distortion and also some noise fixed with digital base line restoration (DBLR) made by some filters. This work has been developed by analysis and testing offline, with the objective of implementing this deconvolution directly in FPGAs to allow the production of a total real signal online in the DAQ (see Figure 6.1). The DBLR implies an extra calibration of the PMTs response to extract the deconvolution coefficients to be used in the signal processing.

Not only the calibration of each PMT individually is needed but also the calibration of the whole detector plane. Not all the sensor measure the same amount of light from different calibration positions, there is a geometrical effect to take into account. As will be shown later, the geometrical distortions can be corrected if its effect is calibrated in advance.

6.1.2 Calibration of the tracking readout

Just like the PMTs, SiPMs are gain characterized beforehand. They are arranged according to performance as explained in Chapter 4. Once at detector calibration stage, the procedure is similar as above, response to photons emitted by 400 nm LEDs positioned at the energy plane is registered. There is another possible source of calibration with thermally generated photoelectrons (*dark currrent*) from the SiPMs itself [123, 124]. The low dark current rate allows to count very few photons and fit them to identify the proportional constants but the electronic noise dominates over the low counts overdoing the automatic SPE peaks searches. In addition the LED emission allows fastest calibration as the photon emission is tuned at the level of the electronic noise, not having to wait for large statistics.

Therefore, registering data with low level light pulses (pulsing an LED in one of the PMT cans every 100 μs) a basic estimation of the conversion gain can be determined. This is done by using the difference in position of the pedestal (most probable value) and the next peak which corresponds to the ADC due to one avalanche in the channel. Hence, with the registered data, the most probable value and the sigma of the peak corresponding to zero avalanches in each event can be seen

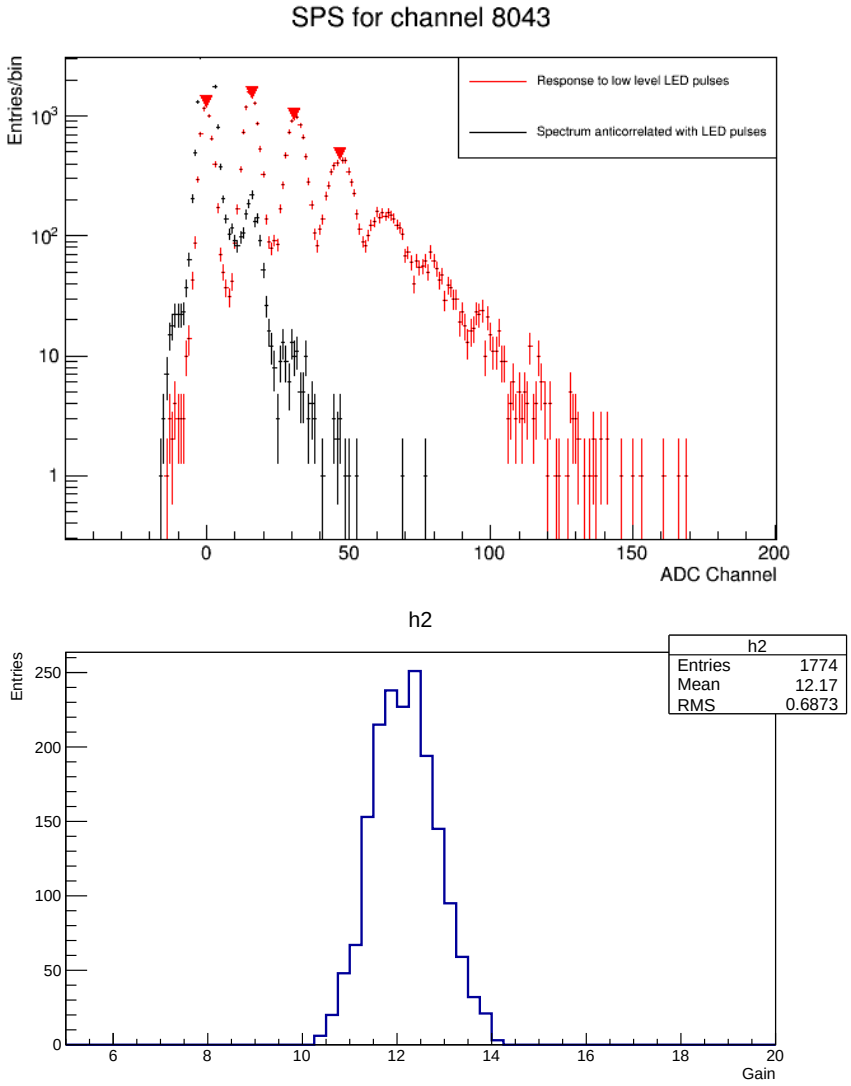

Figure 6.3: (Top) Single photo-electron spectrum of one SiPM when illuminated from a LED in the energy plane and the same channel with the LED switched off. (Bottom) Distribution of the SiPMs gains obtained fitting the single photo-electron spectrum of each SiPM.

in Figure 6.3. The pedestal is defined as the mean of the most probable values over the course of the run and the sigmas define the rms. That characterizes the electronic noise useful for monitoring the stability of the electronics. The characterization of the electronic noise can be also determined using automatically triggered data without external (LED) light input.

Afterwards, in the same analysis, fitting a Gaussian to the peaks corresponding to the numbers of photoelectrons and using the position in a linear fit provides the conversion gain (Figure 6.3).

At the end all the sensor calibration parameters are stored in a database and accessed by the data preprocessing jobs at the first stage of the offline data acquisition. It converts the ADC waveforms information from the electronic stage to photoelectrons.

6.2 Geometric effects correction with low energy calibration

The basic signal used in NEW is the sum of the signal from each of the PMTs. This sum must be normalized for geometric effects of two main types which cause the response of the detector to vary according to where the energy was deposited. The first is due to electron attachment during ionization electron drift, which causes deposits closer to the EL gate to be registered with higher charge. The second corrects for transverse position with a number of effects such as variation in reflectivity, charge losses at borders and variation of TPB deposit contributing to the variation in registered charge.
That is to say, for the same energy released by an event, sensors in different positions can measure different amount of light due to various effects: light collection efficiency, boundary effects, solid angle effects... For detector physics is well known that a spatial characterization of the detector is needed to have a good resolution. If energy resolution is a must, as in our case, a detailed understanding of these effects is relevant. For this reason a detailed calibration for mapping the response of the energy measurement of the whole detector is needed, the more positions characterized the better understand of the detector.

As shown in [123] the most effective way to characterize the most amount of spatial position response is with small energy deposits contained within virtually point-like areas distributed throughout the detector volume. This hypothesis was proven with xenon K_α X-Rays ($\sim$ 30 keV) as point-like sources of energy. External gamma sources can extract internal shell xenon electrons. These events are produced and usually recorded while taking data with severals sources, but is not optimized since the excitement of the K-shell by an interacting gamma only accounts for a small fraction of the events meaning that a full characterization of the detector would require a very extended run. Therefore, the statistics and spatial distribution can be improved with a dedicated calibration source.

This lead to the idea of use other low energy and higher activity radioactive point-like sources. As demonstrated in [162] the use of the isotope $^{83}Kr^{m}$ results in a effective way of characterizing a scintillation detector. $^{83}Kr^{m}$ atoms are produced through the decay of ^{83}Rb atoms trapped in a zeolite molecular sieve. This is introduced in a trap filter in the gas system of the detector. By circulating the gas through the rubidium zeolites, the krypton from the decay diffuses into the gas and is distributed throughout the entire system. $^{83}Kr^{m}$ emits a 32.1 keV conversion electron (99%) and a second 9.4 keV conversion electron (75%) or gamma with 154 ns delay (Figure 6.4). This time delay make both electrons indistinguishable for the readout, as shown later, due to the slow time response of the TPC. Thus, in almost all cases we detect a single deposit of 41.5 keV (similar to the X-Ray method).

This calibration source allow the characterization of the scintillation (S1) and electroluminescence (S2) response at low energies. Those $^{83}Kr^{m}$ energy deposition can be considered as point-like events that, by diffusion of krypton in gas, cover all the detector leaving low energy interactions. This allow to characterize the detector response to events all over the active volume to give geometrical correction weights for larger events.

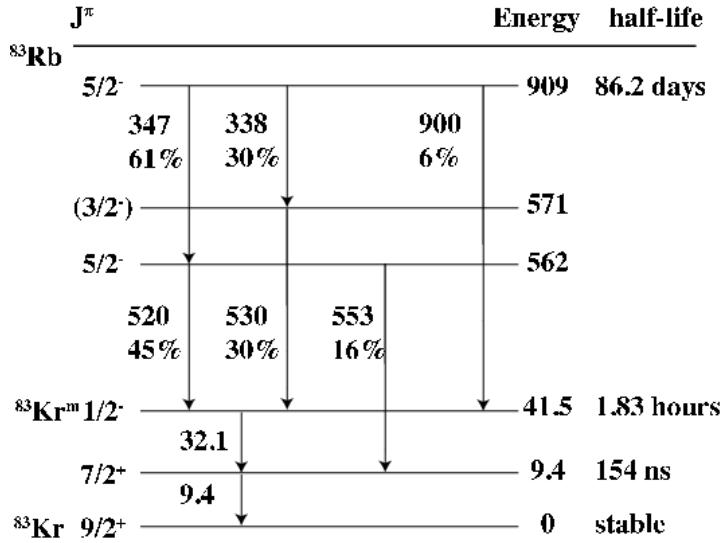

Figure 6.4: ^{83}Rb energy level decay scheme from [162]. ^{83}Rb decays 81% to the ^{83}Kr^{m} excimer state with a half-life of 86.2 days. This ^{83}Kr^{m} state emits a 32.1 keV conversion electron (99%) and a second 9.4 keV conversion electron (75%) or gamma with 154 ns delay.

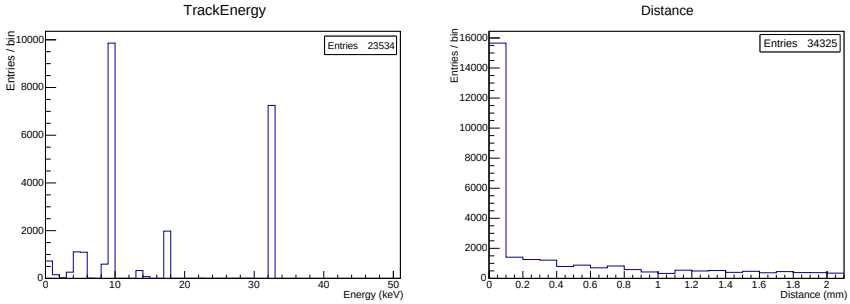

Figure 6.5: $^{83}Kr^{m}$ deposited energy (left) and track length (right).

6.2.1 Monte Carlo studies and analysis development

Unlike the sensor calibration, here the procedures for the spatial detector calibration have been exercised with MC simulation due to the difference between DEMO and NEW made unable the direct usage of the procedure.

The simulation of the $^{83}Kr^{m}$ radioactive source is done with **NEXUS**, and as in the case of other sources (§ 5.1.2) a specific generator for $^{83}Kr^{m}$ has been developed. In Figure 6.5 it can be seen the MC truth information of the deposited energy of $^{83}Kr^{m}$ decay generator. There can be identified the 32.1 keV electron and the 9.4 keV electron well separated, accompanied by a range of X-Rays. It is shown also the true track length of the energy deposition to base the point like feature.

The simulation tools here differ from those used for the background model (§ 5.1) at the point of the reconstructed signal. Besides NEXUS, an additional simulation toolkit is used:

- elparametrization: code to parameterize the response of the EL production grids.
- detsim: package to simulate the secondary scintillation signals and to produce sensor waveforms from MC true information. It can also reproduce the trigger.

As explained in § 5.1 the large number of photons simulated of scintillation and electroluminescence per interaction is very demanding

in CPU memory/time managing. In this case this is simplified by characterizing its potential response by a set of parametrical functions.

The photon detection probability for a given SiPM is parameterized by a polynomial function that depends on the distance of the SiPM to the EL emission point. The detection probability for PMTs is also a polynomial function that only depends on the radial distance of the EL point to the center of the chamber.

Starting with the NEXUS events and passing through the light production parametrization and a simulation of sensor response, which uses calibration information from NEW, the response of the detector is simulated. From this point the software that processes and analyses MC and data is the same. The framework used for data processing is **ART** (event-processing framework [163]). Preprocessing data modules convert the waveforms into an art-based event model, reconstructing the sensor hits and applying the charge calibration (ADCs to PEs in the data case) from the database.

A simple average of the response of the 12 PMTs is taken and signal pulses of two types are sought. The S1 signal, corresponding to the prompt scintillation light, is sought first by requiring charge above a minimum threshold for a minimum duration. Where at least one S1-like pulse is found, S2 (ionization) signals are sought in the same way with appropriate thresholds.

The final step of the preprocessing involves using the time information of the selected S1s and S2s to add SiPM information for tracking. An additional requirement that a SiPM has charge greater than the baseline calibration value, corresponding to an exclusion of 99% of the noise plus dark current, is also imposed. In this way the information from both sensor planes in the region of a selected event are collected together to be presented to reconstruction algorithms.

Figure 6.6 shows the simulated krypton events in NEW filling all the active volume. Simulation studies show that the event reconstructed rate for 1 kBq $^{83}Kr^{m}$ source could be 900 Hz taking into account our trigger. Thus with $\sim$ 10 hours on data taking $\sim$ 600 events per 2×2 mm x-y bins can be reached. That shows the necessity of large amount of events to fully characterize geometrically the chamber with high statistics.

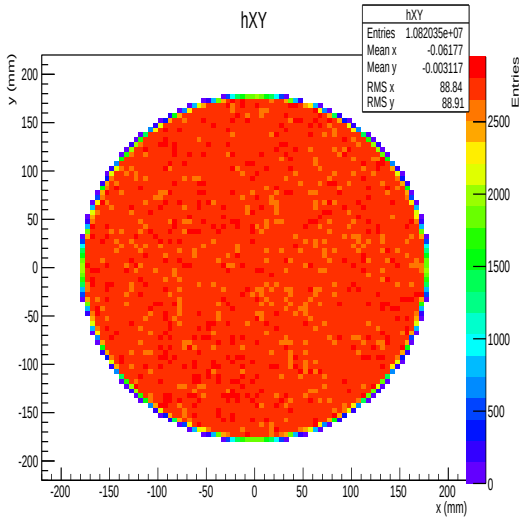

Figure 6.6: Simulated krypton events in NEW

Point like event selection

From DEMO experience the necessity to ensure the point like geometry of the events was faced. Even with MC data shows up that not all events fulfill the requirement, due to overlapping of the first $^{83}\mathrm{Kr}^{\mathrm{m}}$ electron with a second gamma producing a second separated electron. Although it would be treated as unique electron track due to diffusion in real data, it has to be exercised for the real data case where other event can also happen. Therefore an analysis filter was developed by requiring:

- Event filter: A maximum of one S1 and soft cut in total energy at the S2 charge between [20,1600] photoelectrons is required per event.
- Cluster builder: A basic reconstruction of the position of the event is done by a simple barycenter algorithm to enable the positioning of the events. Being point-like events, compute the position by simple calculation of the x-y event coordinate by SiPMs touched around the maximum is enough.

- XRSelector module: Ensures the selection of point-like depositions by requiring:
  - fiducial cut of 2 cm far from the light-tube walls, optimized later for the data.
  - only one cluster per time slice (z coordinate).
  - maximum x-y distance between two contiguous clusters of 5mm to avoid possible distortions.

Here, for the development of the code and the selection study, MC reconstructed data was used and then the overlap of the two electrons in DAQ time is seen (Figure 6.7). In the simulation, $^{83}\mathrm{Kr}^{\mathrm{m}}$ in NEW at 10 bar and a EL yield of 1545 pe/e^- giving a conversion of 35 pe/keV was set. Then the above shown true MC deposited energy of the two electrons (32.1 keV and 9.4 keV) is reconstructed as summed peak at 1452.5 pe (41.5 keV).

The most relevant selection cut (as can be seen in Figure 6.7) is the fiducialization that reject half reconstructed events due to deposition of part of the energy outside the detector active volume or close to the edges where is partially reconstructed.

The peaks that can be seen in the histogram correspond to $\sim$ 500 pe the 9.4 keV gamma, $\sim$ 900 pe the xenon k_α X-Ray and $\sim$ 1400 pe the two electrons.

Drift Velocity

Next process studied in MC to prepare the analysis for the data was the characterization of the detector conditions. $^{83}\mathrm{Kr}^{\mathrm{m}}$ MC data in NEW at 5 bar was used. The measurement of the drift velocity is needed in the experiment. This allow to monitor the stability of the detector, to compare runs with the same conditions and to characterize the detector giving the z dimensions from measured data (this will allow us to make fiducial cuts in z).

Electron drift velocity (v_d) can be determined analyzing the longitudinal event time distribution in the TPC. The drift time (t_d) is well defined by the difference in detection time between the S1 and S2 signals in the events selected. There exists a maximum drift time (t_{dmax}) corresponding to the events just inside the drift region next to

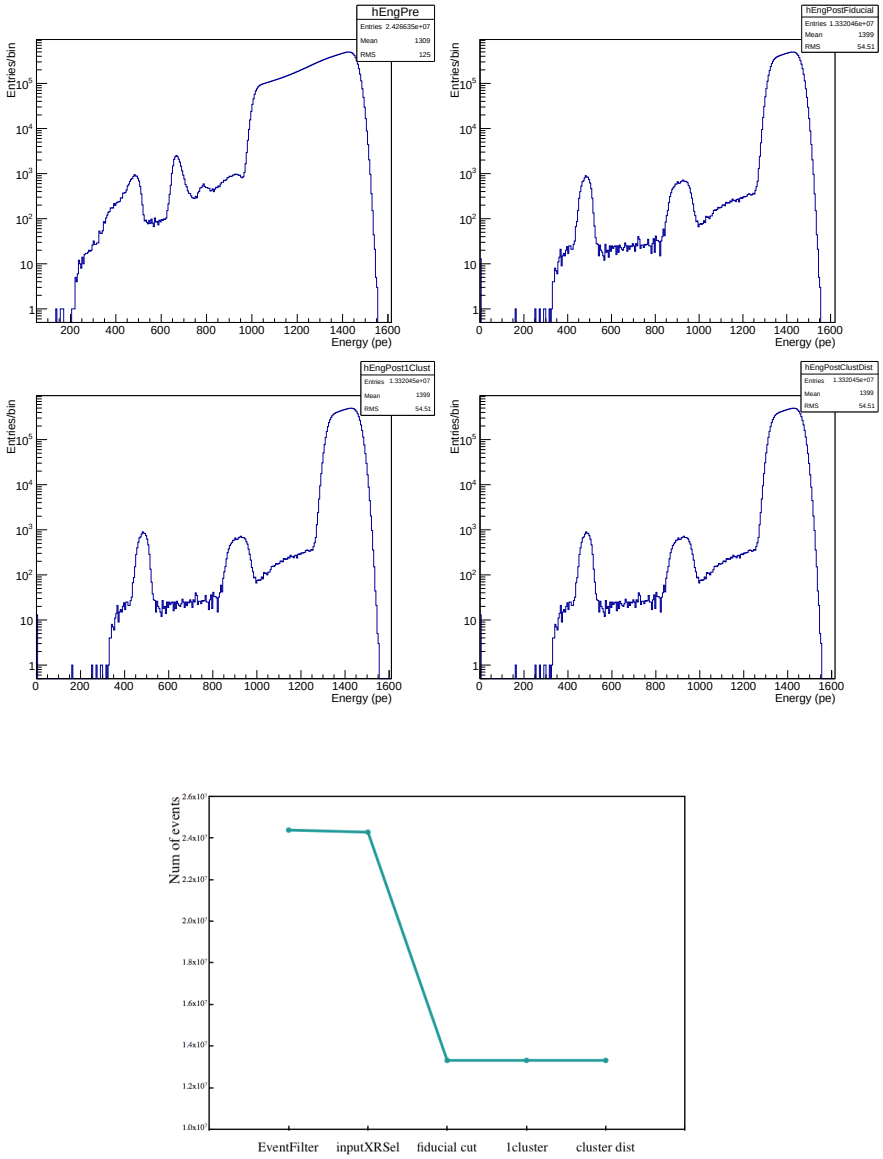

Figure 6.7: Point like krypton events selection in NEW from MC data. (Top, left) Initial energy distribution of $^{83}Kr^{m}$ events. (Top, right) $^{83}Kr^{m}$ events energy distribution after the fiducial cut. (Center, left) Resulting spectrum after one cluster per slice requirement and maximum distance in x-y between clusters (center, right). (Bottom) rejection factors per analysis cut summary.

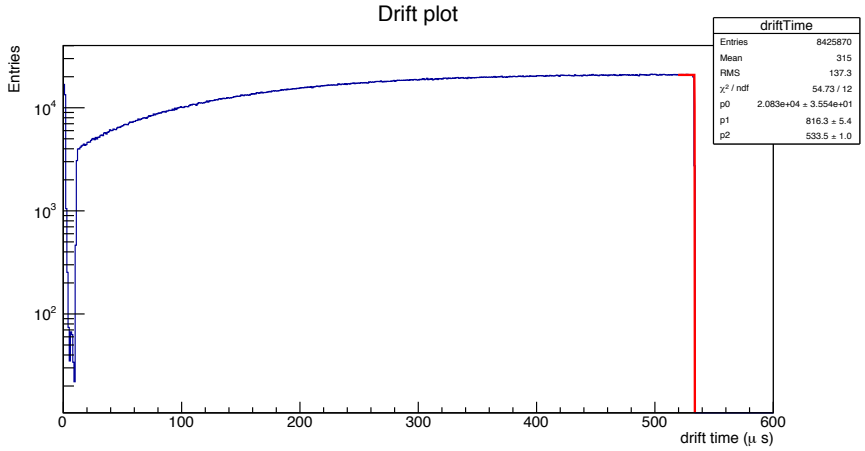

Figure 6.8: Drift velocity analysis from MC data with a simulated 1 mm/μs drift velocity in nexus and reconstructing 1.001 ± 0.004 mm/μs drift velocity from the fit.

the cathode. This maximum can be determined as the half-maximum of a Heaviside function fitted to the event time distribution (shown in figure Figure 6.8). The maximum drift distance can be calculated from the detector design parameters as the total drift distance plus half of the width of the EL region, since the peak of light production is well estimated by that point [123].

The drift velocity can be then calculated from the ratio between the maximum drift distance D_{dmax} and the maximum drift time t_{dmax}:

$$D_{dmax} = \quad 532 + (4/2) \quad = 534 \text{ mm} \tag{6.2}$$

$$v_d = \quad \frac{D_{dmax}}{t_{dmax}} \quad = \frac{534 \text{ mm}}{t_{dmax}} \tag{6.3}$$

Where the design values of the NEW detector are used, 532 mm from cathode to gate and 4 mm of the EL gap. Taking $t_{dmax} = 533.5 \pm 1.0$ μs from the fit, we reconstruct 1.001 ± 0.004 mm/μs drift velocity.

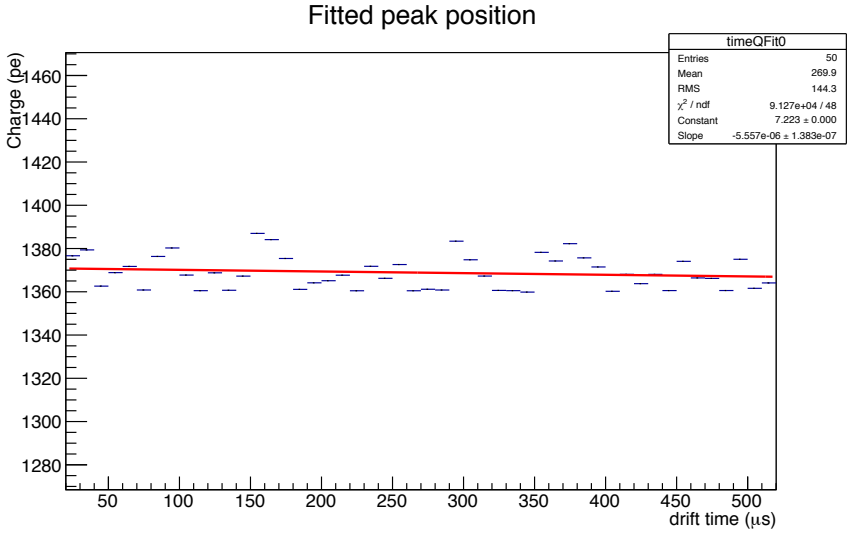

Figure 6.9: ^{83}Kr$^{\mathrm{m}}$MC electron lifetime measurement. Since no attachment is simulated, the life time is large.

Electron lifetime

As mentioned before the data will need to be corrected for attachment during drift due to gas impurities. This can be studied or at least prepared with Monte Carlo simulations. Electron attachment is determined via the average energy measured along the z position for ^{83m}Kr events (Figure 6.9). Fitting an exponential to the measured charge

$$N(t_d) = N(0) \cdot exp(-t_d/\tau) \tag{6.4}$$

where $N(t_d)$ is the measured charge at a given drift distance (t_d), $N(0)$ the original charge and τ the decay constant; an estimation of the τ can be obtained to apply it later to the data, reconstructing the corrected data by electron attachment.

Geometrical corrections

The S2 light collected by each PMT depends on the position of the EL where it was produced, and on the location of the PMT on the energy plane. There are some circumstances that can distort the energy measured, mostly events happening in the borders, its relative acceptance, the TPB inhomogeneities... causes than can be thought in advance.

The geometrical factor affecting these events can be computed using low energy calibration data. Knowing this factor, a better estimate of the total energy can be obtained. To estimate the geometrical corrections, a large dataset of $^{83}\mathrm{Kr^m}$ events is used dividing the EL plane into 5×5 mm^2 bins. The energy spectrum in each bin is is fitted to a Gaussian distribution. From the mean and sigma of the Gaussian distribution we computed the geometrical corrections. The method assumes that each PMT should have seen the same amount of light if there were no geometrical factor effect. This factor $(f_i(x, y))$depends on the PMT and the bin position in the EL grid. It can be computed by normalizing the mean of the gaussian in each bin for a given PMT to a given reference value (for example the charge for the bin in the center of the chamber). The total energy is then the weighted sum of the charge measured by each PMT:

$$Q_{tot} = \sum_i q_i \cdot w_i(x, y) \cdot f_i(x, y) \tag{6.5}$$

Where PMT weights $(w_i(x, y))$ are obtained from the sigmas of the gaussians for a given EL position. In Figure 6.10 it is shown the energy correction factor for a given PMT as a function of x, y in the EL plane. It can be seen that the geometrical factors vary smoothly along the distance from the center of the chamber.

From Figure 6.11 can be said that the geometrical corrections obtained with this method work well at least for the same energy deposition. The mapping of the chamber and the correction factors application, with the development and exercise in Monte Carlo data, shows an achievable energy resolution in NEW of 3.79% FWHM at 41.5 keV $^{83}\mathrm{Kr^m}$peak that can be extrapolated to 0.49% FWHM at $Q_{\beta\beta}$ a ssuming a $\sqrt{E}$ dependency.

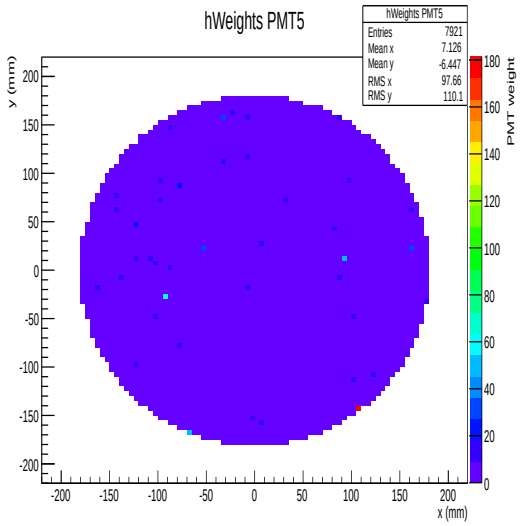

Figure 6.10: PMT number 5 weight factor as function of x-y measured charge.

6.2.2 NEW data: conditions and preprocessing

The NEW data sets used to study the geometrical correction tables with the low energy calibration source of $^{83}\mathrm{Kr^m}$ are described here. The $^{83}\mathrm{Kr^m}$ source is placed inside in the gas system. The source pipe volume contain small ^{83}Rb zeolite spheres, with two filters at the extremes to prevent any solid chip to cause damage. The gas flow carry the ^{83m}Kr isotopes into the chamber. There is also two valves to redirect the gas flow through the source when $^{83}\mathrm{Kr^m}$ calibration data is desired or block this path instead (see Figure 6.12). With the 1 kBq activity ^{83}Rb source (although had decay at least a half-life and a trigger on low energy S2 was used) about 5.3 events per second had been recorded. The Figure 6.12 shows the trigger rate of krypton events increasing as the rubidium valve opens and introduces $^{83}\mathrm{Kr^m}$ in the active volume from the gas system.

As explained in § 4.5, DATE is the DAQ software framework used in NEXT [164] which records the data indicated by the trigger system

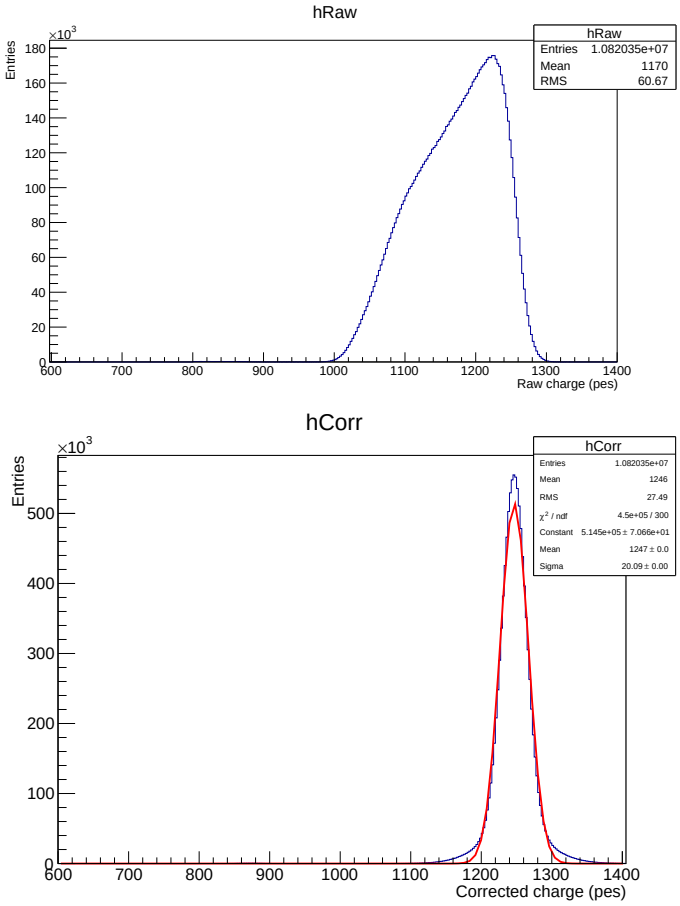

Figure 6.11: Reconstructed charge from $^{83}Kr^{m}$ MC data (top) and the same peak corrected by the weight and spatial factors obtained from the same $^{83}Kr^{m}$ MC data (bottom).

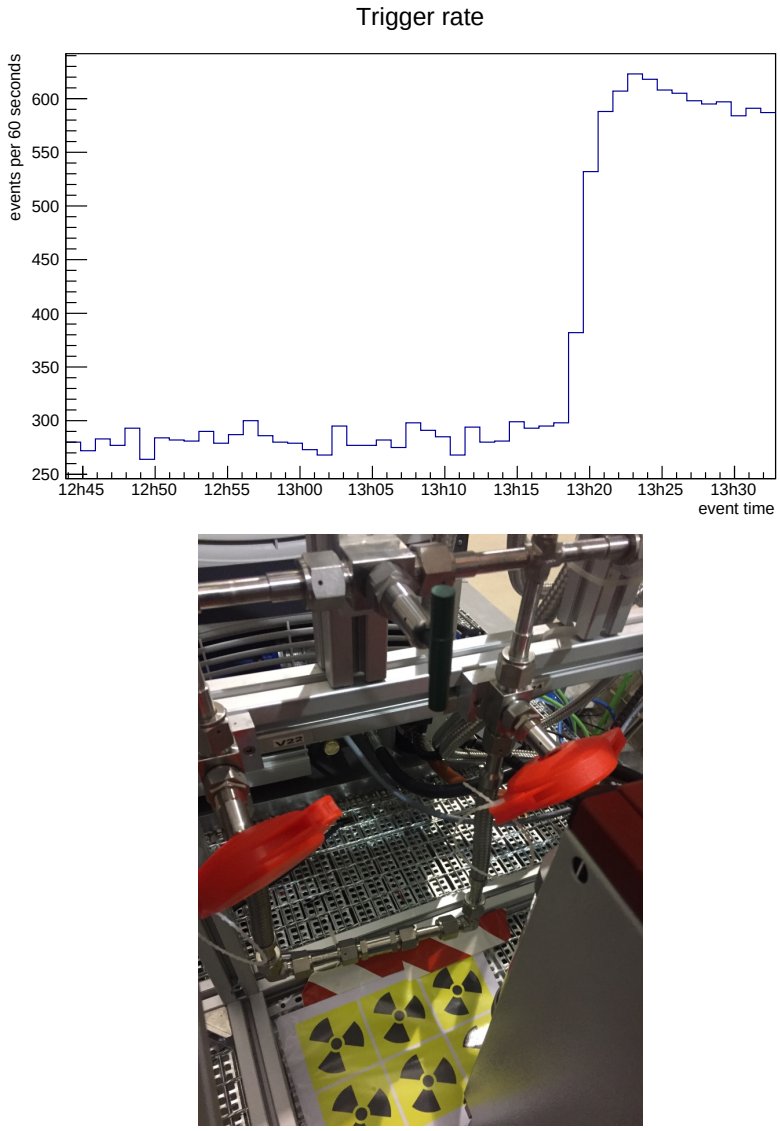

Figure 6.12: Krypton triggered events in NEW as function of time. The ramp up corresponds to the opening of the the gas system valves, shown in the bottom picture, that includes the rubidium sieve into the gas path flow.

(see Table 6.1), then the data is is processed to convert the binary data into into a readable format, an art-based event model [163]. Raw data are then processed with the application of calibration parameters for each channel (ADCs to PEs) resulting in full event buffer information in photoelectrons. Afterwards the selection of possible scintillation (S1) and ionization (electro-lumiescently amplified) S2 signals is done, as explained before for the MC data analysis.

During the commissioning different runs changing the voltages to test the performance (stability and sparks), to achieve a comfortable E/P and correctly tune the trigger system has been carried out. Nevertheless only those relevant subsets for this topic are discussed here. The main data set used for this study is the 2980–2991 run, 5 days stable data taking. The previous set (run 2455) is used for comparison. It was recorded during commissioning and first test of $^{83}Kr^{m}$ trigger. Due to the instabilities and the fact that an extra filling of xenon was needed due to partial emergency recovery, not totally compatible useful data were obtained. Nevertheless this change in detector conditions seem to be responsible of the inhomogeneous distribution along drift of the main data set studied (2980–2991). This will be discussed later as can be seen clearly in the drift velocity study.

The latest set (4196) shows the improvements on the data taken optimization. This new set of data was recorded after an intervention in the detector due to a field cage damage. The construction of the HHV feedthroughs was improved and the quartz anode replaced. For this upgrade the TPB and ITO were decided to be coated at the same side (facing the active) instead. As will be discussed latter, data showed a possible charging up of the TPB layer without the possibility of discharging while the electrons were blocked by the quartz in its way to the grounded ITO. This possibly caused the changing EL yield that can be seen in Figure 6.18. Moreover, the spark rate since the change has ben reduced. The detector conditions for the data sets analyzed are summarized in Table 6.1.

	Detector conditions			Trigger conditions					
run	pressure (bar)	cathode (kV)	gate (kV)	Number of PMTs	Baseline dev (ADC)	Q_{min} (ADC)	Q_{max} (ADC)	MinT (ns)	MaxT (ns)
2545	7.00	22	6.5	1	100	1000	10×10^6	0	150000
2980	7.03	21.5	6.5	12	100	3500	25000	500	150000
4196	7.2	28	7	11 (5)	10	8000	4000	2000	40000

Table 6.1: Detector conditions for data sets analyzed.

6.2.3 Data analysis and results

The main results of the commissioning of the low energy calibration procedure are discussed here. The point-like nature of $^{83}Kr^{m}$ events means that they can be used to monitor fundamental properties of the gas and detector as said before. Therefore, the analysis is done as with the MC study: the calibration processing modules analyses the data to estimate, electron drift-time, electron attachment and the geometrical corrections.
The selection of point-like $^{83}Kr^{m}$ events is done with the filter described in § 6.2.1. Here the parameters are tuned to one S1 requirement and S2 charge between 100 and 1000 photoelectrons. The main change from the MC analysis is done in the fiducial cut. Due to the characteristics of the data and being the first calibration runs, the necessity of fully map the whole plane even the radial borders is evident. Therefore a 0 cm fiducial cut is required ensuring data as larger in radius as possible covering the light tube transverse plane as can be seen in the Figure 6.13. The $^{83}Kr^{m}$ reconstructed positions show some spots with less events which correspond to four dead SiPM channels and two faulty channels.

For the drift velocity computation has been necessary to add a background term to the fit. The difference from the MC data (Figure 6.8) where after the cathode position the event rate vanish, to the data recorded where lower rate events beyond cathode are measured, can bee seen zoomed in Figure 6.14. This background could be removed with a data cut in z, but while the objective is to determine the drift length would be impossible to force a cut in z beforehand without affecting the measurement. There can be identified the cathode position an then, as explained in § 6.2.1, a drift velocity of 0.914 ± 0.007 mm/μs is obtained.

The data reveal a good way to better determine the drift length (582 ± 2 μs), showing some discrepancy with the simulated designs. This has been used to tune the future simulations.

The measured drift velocity form combined data run sets (2980 to 2986) of 0.92 ± 0.01 mm/μs is compatible with MagBoltz simulations for this drift filed of 0.913 mm/μs. In Figure 6.15 is shown the drift velocity obtained for each individual data set, showing some variations mainly

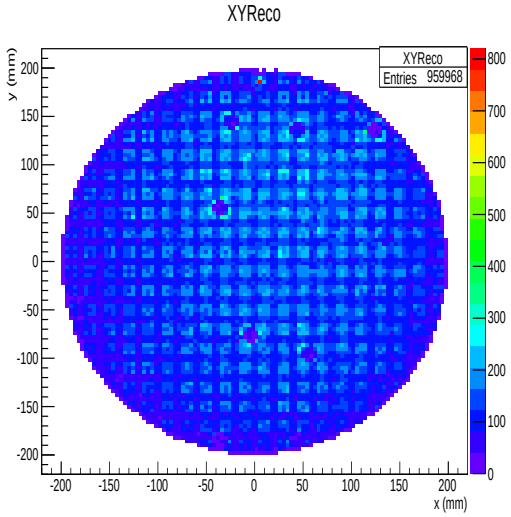

Figure 6.13: Reconstructed position of the $^{83}Kr^{m}$ events along the XY transverse plane.

due to the fitting procedure. Not all the runs have the same statistics and that can harm the fit. Lower statistics runs show larger discrepancy.

Also in the data the spatially distribution of events along the drift axis show some considerations to be discussed. For the main data set (2980–2991) the events tend to accumulate at the first half of the drift length chamber (see Figure 6.16). This was seen in the analysis comparing with other test runs. It seems to be due to the trigger requirements. The trigger bias the data, asking for minimum deviation of the baseline signal greater than 100 ADC counts. This requirement limits small signals far from the anode (input of the gas flow) at high drift (due to diffusion). In addition the trigger was set to wait for only one PMT trigger signal (previous 2545 run) or one of the 12 PMTs (2980 run) while for the upgrade a coincidence of five of the eleven PMTs (one of them was not working) was required, setting out more background events (see Table 6.1). This trigger was finally used for the upgraded detector data taking (4233). Nevertheless as can be seen

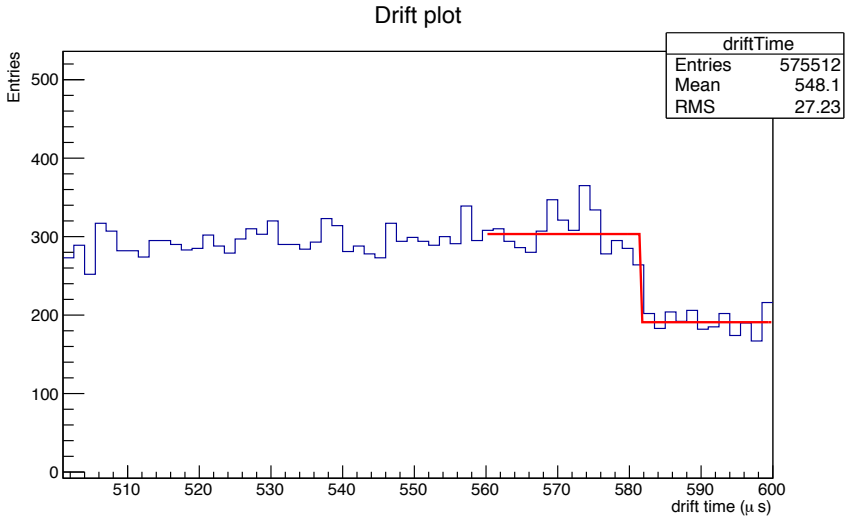

Figure 6.14: Drift length fit with the Heaviside plus background function.

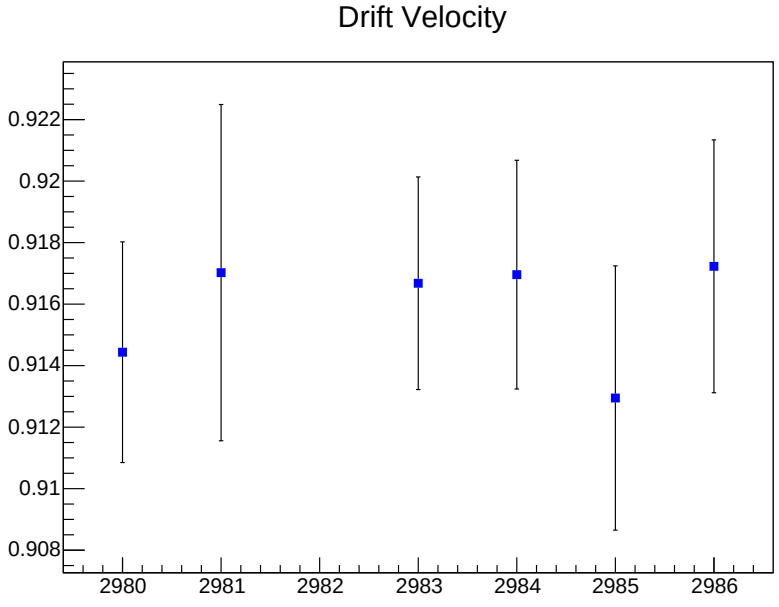

Figure 6.15: Drift velocity variation between runs.

in Figure 6.16 not the full length is covered, the population tends to decrease further form the anode. There can be seen also the nature of the background events entering in the krypton trigger. The peak at the cathode position are alpha decays from the radon attached to the cathode wires. This data taking was done under cold getter gas recirculation what is known to be radon producer [111, 136]. This allows to estimate the radon emanated from the detector components (7 mBq) and monitor its evolution to update the NEXT-100 radon backgrounds estimation.

The difference between the two first data sets (2545 and 2980) in event population is explained by the gas quality drop when refill the detector (2980). Better gas quality was achieved in the first data sets due to the commissioning time when almost 3 months of argon running and purifying to certificate the gas system removed the most quantity of impurities.

Figure 6.16 shows the $^{83}\mathrm{Kr}^{\mathrm{m}}$ events distribution along the drift z-axis. This is very useful for the electron life-time calculation. The procedure is done as for the MC, but as can be seen in Figure 6.17 event population above 300 μs distort the fits. Therefore the electron lifetime calculation is done for the region with large statistics.

This electron life-time correction is needed to equalize the charge along z direction. Effectively the peak position varies form run to run as the gas gets cleaner increasing its yield (as can be sen in Figure 6.18). It can be also due to charging up of the TPB layer, latter changed in the upgrade placing the ITO below the TPB on the active side of the anode to allow them to discharge. In Figure 6.18 is plotted the mean of the peak and the rms as a distribution error.

The correction map is then obtained by the $^{83}\mathrm{Kr}^{\mathrm{m}}$ selected events using 10×10 mm x-y grid. Computing the weight and geometric factor per x-y bin by fitting the measured charge the factors are stored. As done before, only $^{83}\mathrm{Kr}^{\mathrm{m}}$ events in the first half of the chamber are selected to test the quality of the method. Since the factors only depend on x-y coordinates and the data is already corrected by attachment a fiducial z cut can be applied. Once enough statistics is achieved this map can be applied latter to other data.

Figure 6.19 shows the performance of the method. The upper plot

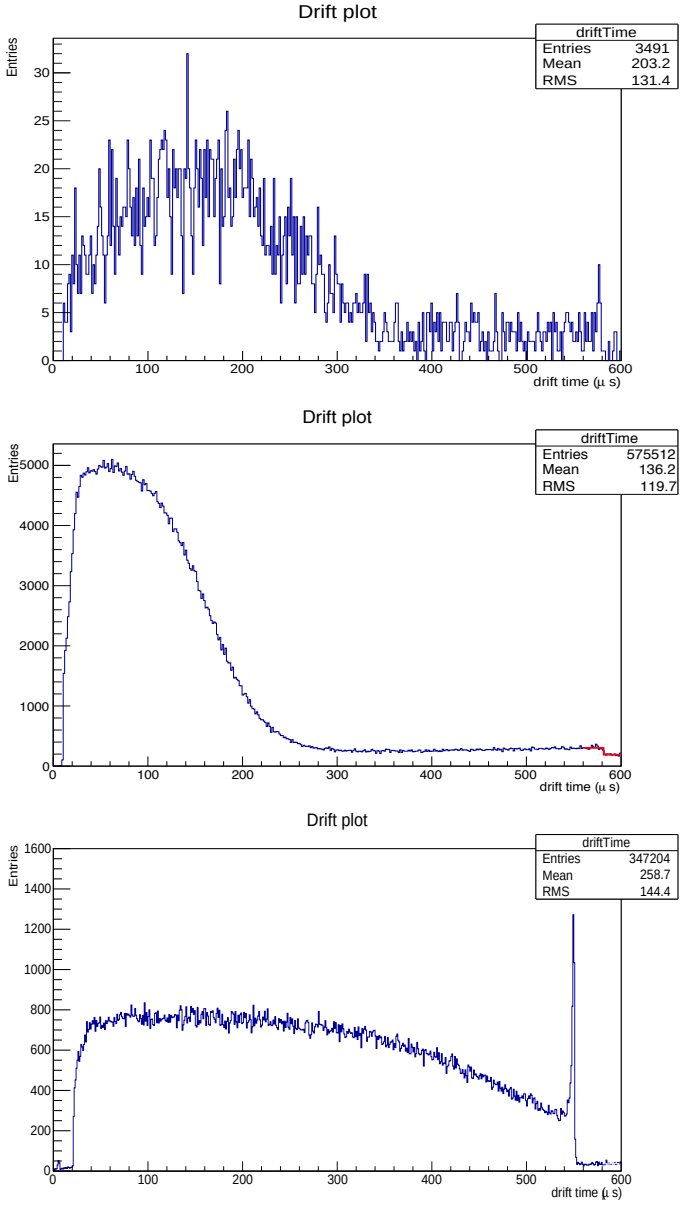

Figure 6.16: $^{83}Kr^{m}$ triggered events distribution along the drift direction for the 2545 run (top), 2980 run (center) and 4196 run (bottom).

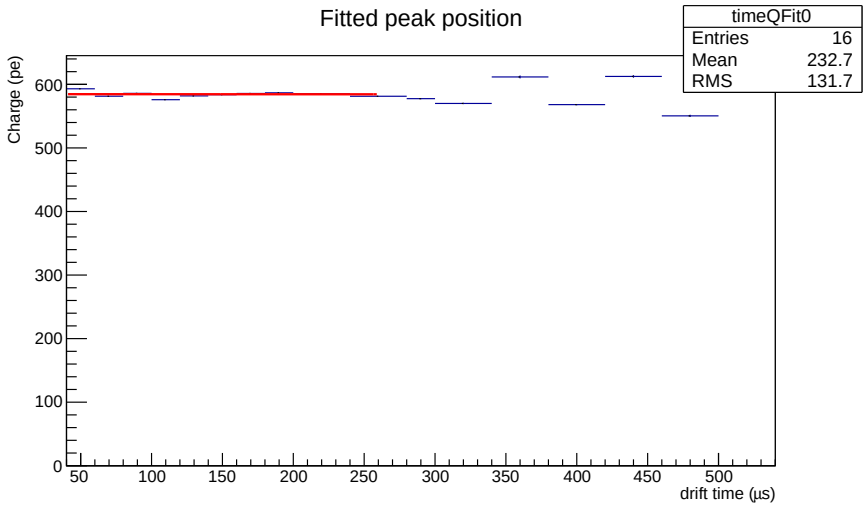

Figure 6.17: Electron attachment measurement analysis from data measuring an electron lifetime of 4 ms.

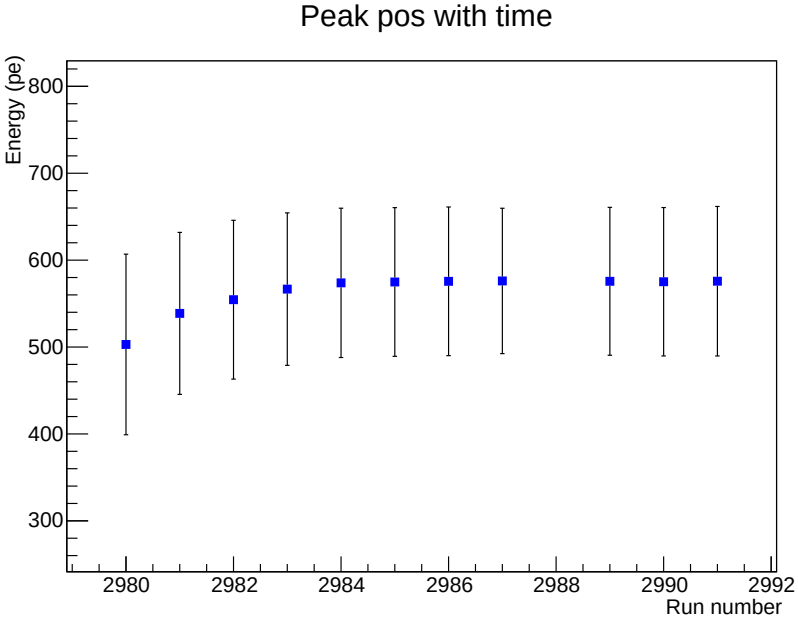

Figure 6.18: Krypton peak energy variation with time (run number) as the gas gets cleaner.

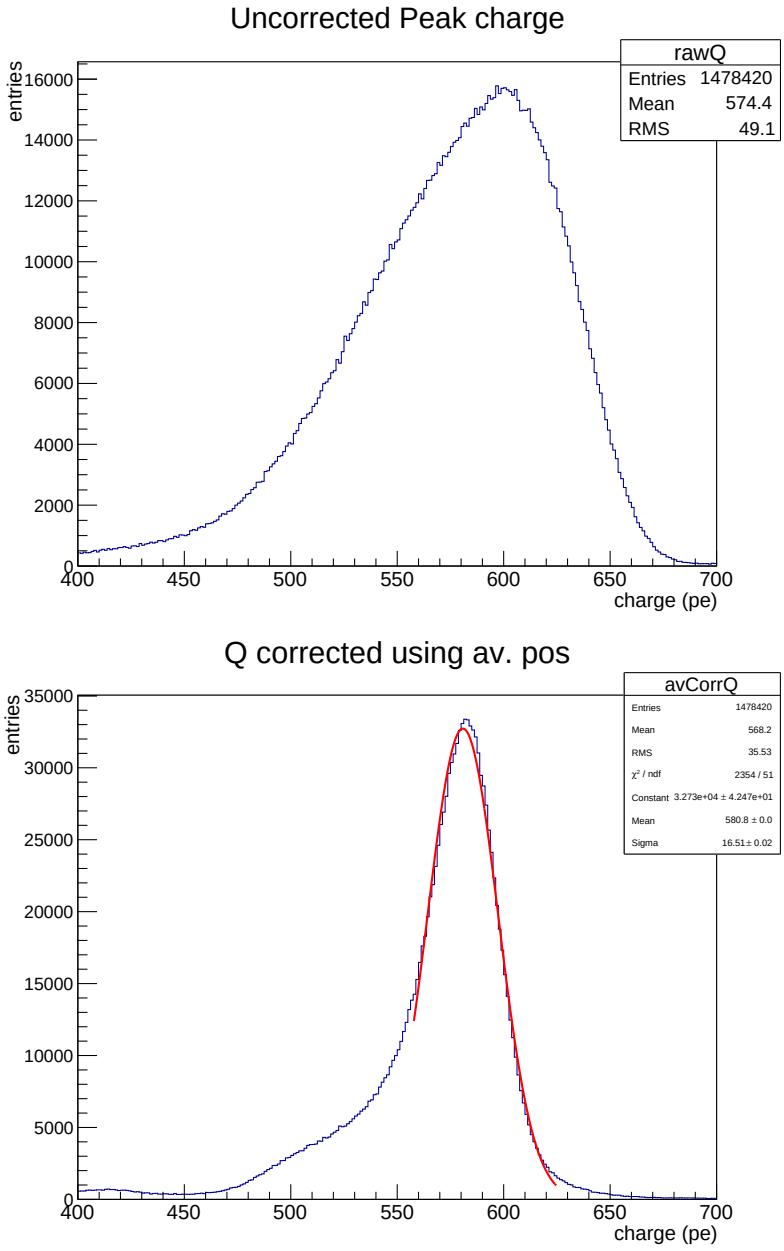

Figure 6.19: Uncorrected $^{83}Kr^{m}$ energy peak at 41.5 keV (top) and geometrically corrected $^{83}Kr^{m}$ energy peak with the electron attachment correction (bottom).

shows the charge initially measured by the PMTs and the lower plot the corrected charge. The fit to the corrected charge show a 6.68% FWHM energy resolution in the measurement of the $^{83}Kr^{m}$ energy (at 41.5 keV). This energy resolution extrapolates to 0.86 % FWHM at $Q_{\beta\beta}$. Its is clearly seen the improvement done with the use of corrections although it can be also seen the low tail of uncorrected events that leave room for improvement. Therefore even reaching the desired $< 1\%$ FWHM extrapolated energy resolution, despite the data conditions, a dedicated study of the detector conditions improvements to fulfill all the requirements for this $^{83}Kr^{m}$ calibration method will improve this results.

As a monitoring tool of the conditions of the detector as well as the $^{83}Kr^{m}$ and sensors calibration, regularly alpha events naturally occurring in the chamber are measured. Since is not an specific calibration source gives the advantage of taking data periodically even when other sources placed at the detector.

6.3 Energy calibration

In addition, once all the sensors and the geometrical effects are calibrated, the energy conversion factor has to be set. Also its stability with the energy scale. Therefore, different calibration sources are used to give the conversion factor from the charge measured (photoelectrons) to the known energy deposited (keV).

NEXT goal is $< 1\%$ FWHM at $Q_{\beta\beta}$ and this can be demonstrated either measuring the energy resolution close to the $Q_{\beta\beta}$ or extrapolating the behavior. The extrapolation is made using several calibration sources from low energy to high energy, measuring the energy resolution and look for the projected performance. A simple extrapolation with $1/\sqrt{E}$ has been demonstrated in [77].

Hence different photopeaks of ^{22}Na, ^{56}Co, ^{137}Cs and ^{228}Th are measured to extract the energy conversion factor and the energy resolution scaling. Moreover cobalt and thorium sources can generate pair production ($e^{+}e^{-}$) giving a topological signature similar to a $\beta\beta0\nu$ track.

With Monte Carlo studies of ^{208}Tl (Figure 6.20) the energy resolution in NEW extrapolates to 0.58% FWHM at $Q_{\beta\beta}$.

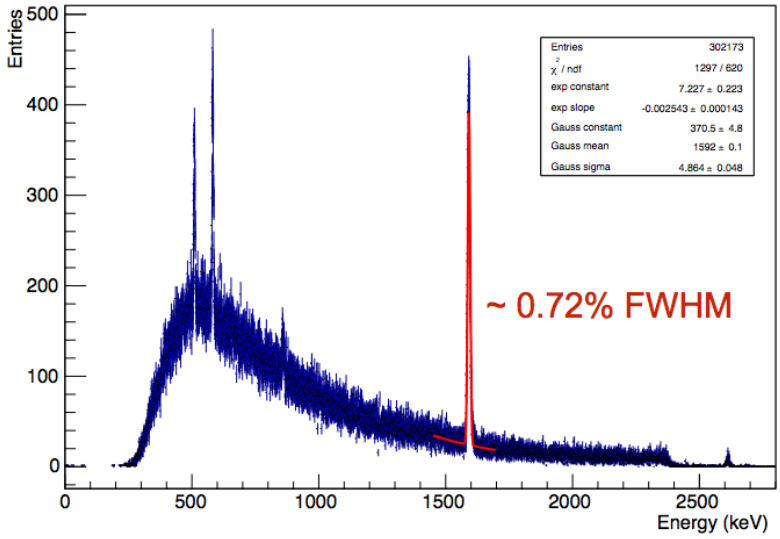

Figure 6.20: MC track energy of ^{208}Tl calibration events in NEW.

"You will not apply my precept," he said, shaking his head. "How often have I said to you that when you have eliminated the impossible, whatever remains, however improbable, must be the truth?"

Sherlock Holmes in "The Sign of the Four'

Chapter 7

Summary and conclusions

The current knowledge of the neutrino interactions, with the observation of the neutrino oscillations implying the first evidence of physics beyond the Standard Model (neutrino mass) opened the door to a new scenario trying to explain the neutrino mass nature (§ 1.2). The Majorana mass nature of the neutrinos (§ 1.3) is nowadays the most satisfactory way to explain the smallness of the neutrino mass and the baryon number asymmetry. The best experimental method that can confirm if the neutrino is a Majorana particle is the search for neutrinoless double beta decay (§ 1.4). Therefore this experimental confirmation of the Majorana nature of the neutrinos has become in the past decades a trendy field. The $\beta\beta0\nu$ searches can be carried out with various approaches optimizing the parameters that can give a positive measurement, the half-life measurement and then the neutrino mass value (§ 2.3). In this work a description of the current experimental techniques has been done (§ 2.4) to present the NEXT technology as the best candidate for this search.

The NEXT collaboration proposes a high pressure xenon time projection chamber for neutrinoless double beta decay searches in the ^{136}Xe isotope. The main advantages of this technique is the usage of xenon as source and detector target, the excellent energy resolution and the availability of topological reconstruction to discriminate backgrounds (§ 3.1). To reach the ultimate sensitivity for $\beta\beta0\nu$ searches the Collaboration has prototyped the technology to demonstrate its feasibility with small devices of kg scale (DEMO, DBDM). In a second

phase, we have built the NEXT-White detector (NEW), of around 10 kg, that implements new technological design solutions and the use of radiopure materials. Finally the Collaboration will construct the NEXT-100 detector with the lessons learnt from his little brothers (§ 3.3). The current experiments have observed the need to go further to a tonne scale detectors to fully cover the inverted-hierarchy region of neutrino masses. In this sense, only those technologies effectively scalable to the tonne scale would take the lead.

This thesis focuses on the NEW design and commissioning. Therefore, a full description of the NEW detector was presented (Chapter 4), focusing in all the technological solutions implemented. Besides the validation of the technology, the NEW detector goal is the demonstration of commissioning a radiopure detector to validate the assumptions and extrapolate to NEXT-100. How the design, concerning the radiopurity needs for the Collaboration, has been adapted from simulation results has been discussed. For this purpose a Geant4 based model of the NEW detector was developed (Chapter 5). How this model was implemented (§ 5.1.1), the assumptions made (§ 5.4), the tools used (§ 5.1, § 5.1.2) and the background activity from the materials simulated (§ 5.2) is described in detail. This allows to project a global picture of the NEW performance. Here has been demonstrated the feasibility and convenience of carrying a simulation study while designing a radiopure detector to check the optimal design and materials to be used.

The analysis of the simulated performance lead to some lessons improving its implementation. The main result of this work on the modeling is the help to the selection on the materials during the design phase: copper manufacturer, SiPM sensors, PMT bases, KDB plug, anode quartz plate and shielding structure paint; as well as the definition of the NEW energy window, the identification of possible backgrounds for the requirements of NEW (low energy backgrounds) and NEXT-100 (radon and cosmogenic backgrounds)(§ 5.3, § 5.5). Moreover, it provides a tunable prediction model that could be adapted during the commissioning. Hence, once validated with the projected low–background data from NEW, it will deliver a nice tool for the predictions on NEXT-100.

Concerning the NEW's goal of the studies of possible backgrounds

and its implication to the $\beta\beta2\nu$ measurement objective, the state–of–the–art of the model has been used to show the overall resulting energy spectrum of NEW demonstrating the richness of analysis used for background rejection. At the end a background rate of 1.32E-05 Bq in ^{208}Tl , 2.34E-05 Bq in ^{214}Bi, 1.42E-04 Bq in ^{40}K and 2.74E-04 Bq in ^{60}Co has been predicted from the MC analysis. This is 4.5 mHz total background rate in the NEW energy window (0.7-2.7 MeV). The radon and neutron contribution has been found negligible compared with the previous after the analysis from the MC simulated rate in NEW. Furthermore, the possibility of a $\beta\beta2\nu$ measurement from the energy spectrum of the $\beta\beta$ candidates with 5σ significance in 90 days has been shown.

On the other hand during the commissioning of the NEW detector, the sensor calibration (§ 6.1) and first calibration data are reported. In this work the simulation and development of the analysis for the novel detector calibration method using $^{83}\mathrm{Kr^m}$ is described (§ 6.2.1). The low energy $^{83}\mathrm{Kr^m}$ calibration source has been useful for understanding the fundamental properties of the TPC as well as for the equalization of the energetic response. This first data during commissioning have been also useful to better tune the trigger in latter $^{83}\mathrm{Kr^m}$ data taking as well as to plan an upgrade of the anode coating (§ 6.2.2).

The developed analysis on the $^{83}\mathrm{Kr^m}$ data shows that the objective of $< 1\%$ FWHM energy resolution at the ^{136}Xe $Q_{\beta\beta}$ value assuming a $1/\sqrt{\mathrm{E}}$ dependence is achievable with the correction methods from low energy calibration data. This method is planned to be used for fully characterize the detector and higher calibration sources to study the resolution dependence with energy.

Appendix

"Winds from the east... Mist comin' in... Like something's a brewin', about to begin... Can't put me finger on what lies in store... But I feel what's to 'appen, all 'appened before...!"

Bert from Mary Poppins

Contributions to NEXT–DEMO

In this appendix my contributions to the prototype NEXT–DEMO are discussed.

This demonstrator phase was the proof of concept of NEXT. It studied some aspects to be demonstrated such as the energy resolution [106] and the tracking [116] (see Figure 1). DEMO was at that time the larger electroluminescent gas TPC made and some performance effects as a large TPC were to be understood.

Some of these techniques developed for the prototype have been applied latter in NEW.

Improving the light collection efficiency.

In order to obtain the required $< 1\%$ energy resolution in the NEXT-100 detector maximal amount of photons, produced in the electroluminescence region, need to be seen by the photomultiplier plane. It means a high collection efficiency. However, as explained in Chapter 3 the light produced in xenon is hard to detect. Xenon scintillates in the VUV range, with a peak at $\sim$175 nm. Therefore, near 90% reflection efficiency is required from the walls of the light tube surrounding the fiducial volume of the NEXT detector [114].

Material reflectivity for VUV wavelengths is dramatically poor but as wavelength increases it can be optimized [165, 114, 166, 167, 168]. For the DEMO detector different reflectors were studied: peek and teflon panels, ESR (Vikuiti^{TM} enhanced specular reflector foil) from the company 3M^{TM} and Tetratex (TTX) from the company Donaldson

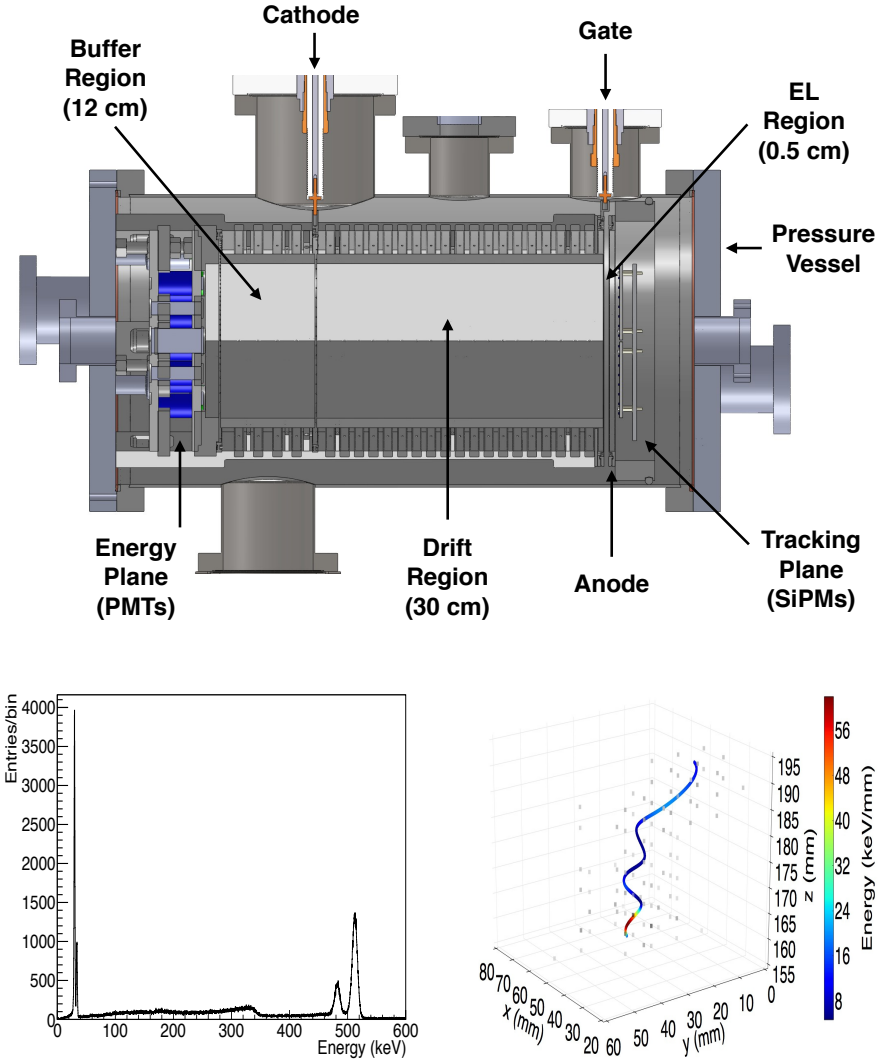

Figure 1: NEXT–DEMO drawing (top), ^{22}Na energy spectrum recorded in DEMO (bottom left) and electron track in DEMO (bottom right).

Membranes. The ESR foil is a multilayer specular reflecting polymer measured to be highly radiopure. Its appearance is that of a polished metal although the material is non conducting. It has a specular reflection coefficient of practically 100% in a large region of the optical spectrum. TTX is an aligned polytetrafluoroethylene (PTFE) fibrous cloth and is nearly a 100% diffuse Lambertian reflector. It is also radiopure (typically less than 1 ppb of natural chains, which, given the very low mass involved, gives a negligible contribution to the radioactive budget) and has low degassing. The studies measured their reflectivity to the VUV light and their suitability in terms of stiffness for a large light tube construction.

Moreover, although the DEMO PMTs had the same QE for light in this range and in the blue (about 25%), the MPPCs had a very low PDE below 200 nm. In addition the PMTs for NEXT-100 will be enclosed in cans coupled to the gas through sapphire windows [114]. UV grade sapphire is extremely expensive, and thus coating the sapphire windows of the PMT enclosures with a wavelength shifter (WLS) appears also as mandatory. Therefore, the use of a WLS also in the light tube was decided to improve the light collection efficiency, following the approach of ArDM Collaboration [169]. The internal light tube surfaces can be coated with 1,1,4,4-Tetraphenyl-1,3-butadiene (TPB), a wavelength shifter that has a 99% efficiency of transforming UV light to blue. Measurements of a reflectance coefficient at 430 nm close to 97% of coated reflectors, for a wide range of coating thicknesses were known [169] (Figure 2). In addition, the light yield measurements showed no relevant aging effects [170].

Then the reflectivity studies for the aforementioned materials, as function of their possibility to be efficiently coated with the already known TPB WLS [171], show a possible improvement on the reflectivity of the light tube [165].

The coating setup consisted in a vacuum chamber enclosing 13 ceramic crucibles used to contain and melt compounds (Figure 3). The evaporator was lend by the ArDM collaboration. Before the TPB evaporation the whole setup was cleaned to remove any traces of other molecules. Vacuum evacuation of the chamber was done through the liquid nitrogen cooled cold trap. The cold trap was used in order to protect the turbo-pump from being contaminated by the TPB. After

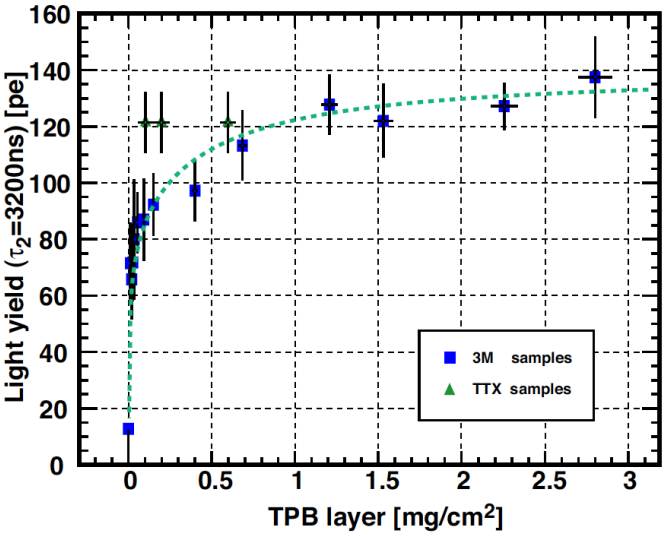

Figure 2: Conversion efficiency as absolute yield in photoelectrons for the various thicknesses of deposited TPB on 3M^{TM} foil compared to a few measurements of TTX foils [169].

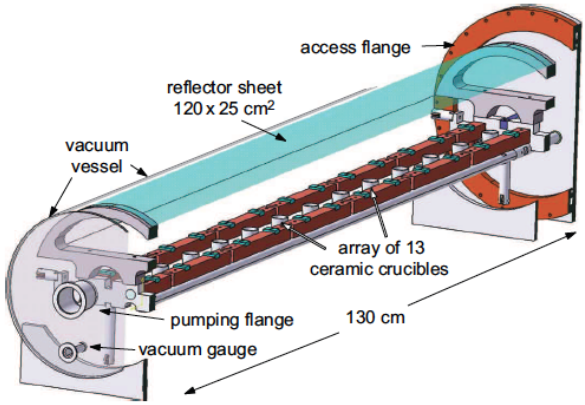

Figure 3: Drawing of the ArDM setup used to deposit layers of TPB onto 3M^{TM} and TTX foils.

Figure 4: The ArDM chamber used for TPB deposition located at IFIC. The chamber is in the background with the vacuum turbo-cube in the foreground. The chamber is being evacuated through a liquid nitrogen cooled cold trap to protect the turbo pump from TPB contamination.

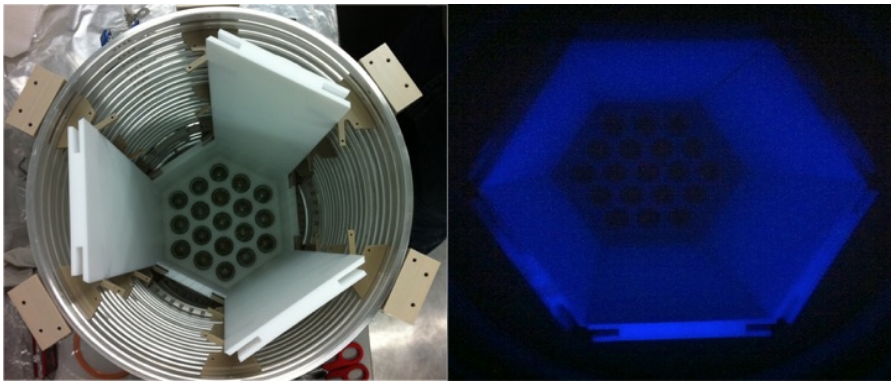

Figure 5: (Left) NextDemo light tube teflon panels assembly inside the field cage rings. (Right) Light tube coated with TPB and illuminated with a UV lamp.

achieving 10^{-4} mbar vacuum the deposition run started. The crucibles were heated by a cartridge with an adjustable current for monitoring the temperature and controlling the evaporation rate to avoid bubbling and sputtering of the TPB onto the exposed substrate. As the light tube cover the inner part of the field cage, the presence of a strong electric field demands non conductive material as the substrate for the wavelength shifter. The measured reflectivity of the ESR + TTX foils was about 97% at 430 nm [165].

At the end the implementation of TPB teflon coated panels in the DEMO detector was decide due to structural needs and performance of the detector conditions. The TPB coating of the teflon panels was done via vacuum evaporation in house. Several test to optimize the process as well as the desired thickness of TPB layer were done. At the end depositions of ~ 0.2 mg/cm^2 were achieved and used in DEMO light tube (see Figure 5). The improvement in collection efficiency with the increase in the reflectivity of the light tube due to the the use of TPB allowed to trigger in S1 with better efficiency. In comparison with ^{22}Na data before light tube coating, 3 times more light was measured with the use of TPB. Furthermore, it was demonstrated that a better collection efficiency undergoes in an improvement in the energy resolution [117].

Sensor calibration optimization with single photon response

The development of the calibration of the PMTs in the DEMO detector is described here as a background for the procedure used afterwards in the NEW detector. When a precise measurement of the energy deposited into any detector is needed, a precise calibration of the instruments used for measuring this deposition is a must. As described in § 6.1, the optical readout used (PMTs) have to be characterized to know the conversion factor of the incoming photons (pes) to the electrical signal amplification and digitization (ADC). To calculate this proportionality constant was used the single photon detection method by LED emission. Using a pulse generator the LED in the chamber were shined for their calibration. The generator was controlled manually and thus allowed to tune the voltage, amplitude and frequency to adjust then to our needs. At the beginning the calibration LEDs were placed in the same plane as PMTs shining towards the tracking plane. The low amount of light collected by reflection and the interference produced lead to the replacement by deploying one LED in the center of tracking plane instead when DEMO was upgraded.

First the default method previously used was the calibration of the SPE region one by one offline. This was extended to calibrate the whole spectrum with a more general function sum of three Gaussian. That was an offline fit that included the pedestal, 1 and 2 photoelectron peaks. It was found that the optimal way to extract the gain from the calibration spectrum was the generalization to a **N** Gaussians correlated fit function.

$$F(x) = N_0(P(0;\mu)G(x,x_p,\sigma_p) + \sum_{n=1}^{N_{max}} P(n;\mu)G(x,nx_1 - x_p,\sqrt{n\sigma_1^2+\sigma_p^2}), \tag{1}$$

Also developed at DEMO phase, the procedure was automatized. The software that measured the signal, included an automatic fitting function that returns the parameters of the fit. In Figure 6 the results of the method developed are shown and its use for monitor the performance of the DEMO PMTs with time [116].

The data taking was done with DATE-DAQ and the preprocessing and calibration modules with the FMWK framework. Later on was translated to ART for its usage in NEW.

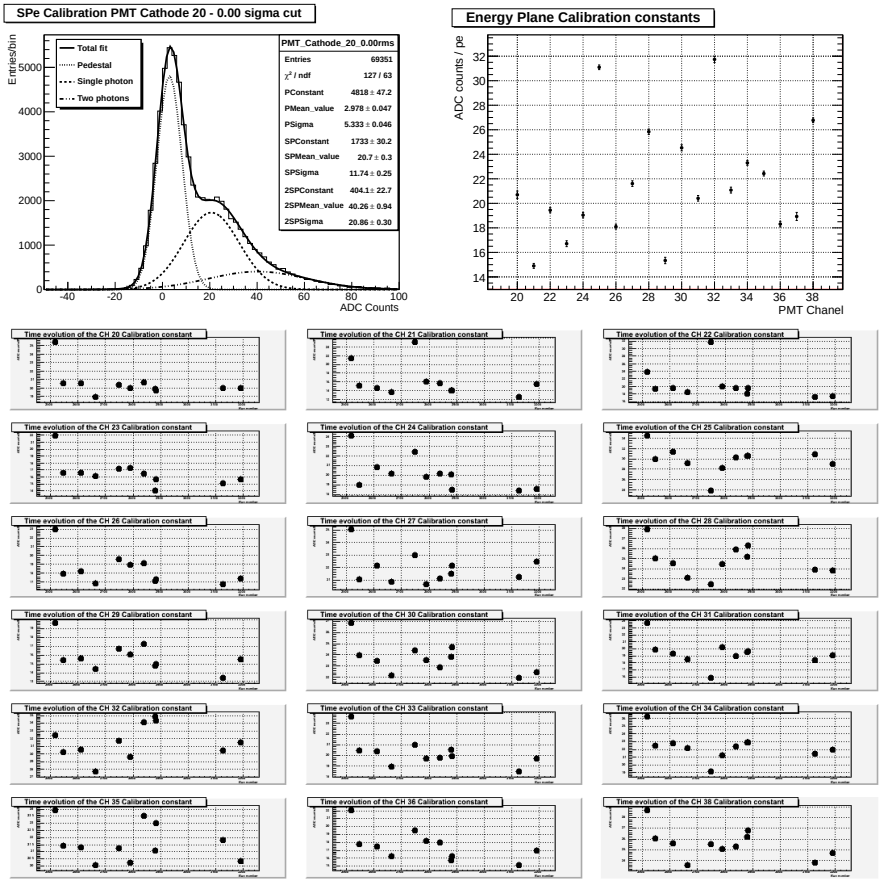

Figure 6: PMT calibration constants and its evolution.

Bibliography

[1] S. L. Glashow, *Partial Symmetries of Weak Interactions,* Nucl. Phys. **22** (1961) 579–588.

[2] S. Weinberg, *A Model of Leptons,* Phys. Rev. Lett. **19** (1967) 1264–1266.

[3] A. Salam., *Weak and electromagnetic interactions - in elementary particle theory: relativistic groups and analyticity,* N. Svartholm, ed p. 367. Almqvist & Wiksell, Proceedings of the eighth Nobel symposium. (1968).

[4] Wikipedia, *Standard model — wikipedia, the free encyclopedia*, 2008. `https://en.wikipedia.org/wiki/Standard_Model`.

[5] F. Reines and C. L. Cowan, *Detection of the free neutrino,* Phys. Rev. **92** (Nov, 1953) 830–831.

[6] *Pauli letter collection, letter to gruppe der radioaktiven bei der gauvereins-tatung zu tübingen.* Lise Meitner, 1930-12-04. CERN Archives. Bldg. 61-S-001 - Safe 3 `http://cds.cern.ch/record/83282/files/meitner_0393.pdf`.

[7] J. N. Bachall, *How the Sun Shines.* Nobelprize.org. Nobel Media AB 2014. Web. 28 Apr 2017. `http://www.nobelprize.org/nobel_prizes/themes/physics/fusion`.

[8] M. Rowan-Robinson, *Night Vision: Exploring the Infrared Universe.* Cambridge University Press, 2013.

[9] W. T. L. Kelvin, *On the age of the sun's heat,* Macmillan's Magazine **5** (1862) 388–393.

[10] L. Badash, *The Age of the Earth Debate.* Scientific American, August 1989.

[11] M. F. L'Annunziata, *Radioactivity. Introduction and History.* Elsevier, 2007.

[12] A. Einstein, *Ist die Trägheit eines Körpers von seinem Energieinhalt abhängig?,* Annalen der Physik **323** (1905) 639–641.

[13] G. Gamow and E. Teller, *Selection rules for the β-disintegration,* Physical Review **49** (1936), no. 12, 895.

[14] H. A. Bethe, *Energy production in stars,* Phys. Rev. **55** (Mar, 1939) 434–456.

[15] B. T. Cleveland, T. Daily, J. Davis, Raymond, J. R. Distel, K. Lande, et al., *Measurement of the solar electron neutrino flux with the Homestake chlorine detector,* Astrophys. J. **496** (1998) 505–526.

[16] B. Pontecorvo, *Report pd-205.* Chalk River Laboratory, 1946.

[17] K. Arisaka et al., *Search for Nucleon Decay Into Charged Lepton + Mesons,* J. Phys. Soc. Jap. **54** (1985) 3213–3216.

[18] Kamiokande-II, K. S. Hirata et al., *Experimental Study of the Atmospheric Neutrino Flux,* Phys. Lett. **B205** (1988) 416. [,447(1988)].

[19] Kamiokande, K. S. Hirata et al., *Observation of b-8 solar neutrinos in the kamiokande-ii detector,* Phys. Rev. Lett. **63** (1989) 16.

[20] J. N. Abdurashitov, E. P. Veretenkin, V. M. Vermul, V. N. Gavrin, S. V. Girin, V. V. Gorbachev, P. P. Gurkina, G. T. Zatsepin, T. V. Ibragimova, A. V. Kalikhov, T. V. Knodel, I. N. Mirmov, N. G. Khairnasov, A. A. Shikhin, V. E. Yants, T. J. Bowles, W. A. Teasdale, J. S. Nico, J. F. Wilkerson, B. T. Cleveland, and S. R. Elliott, *Solar neutrino flux measurements by the soviet-american gallium experiment (sage) for half the*

22-year solar cycle, Journal of Experimental and Theoretical Physics **95** (2002), no. 2, 181–193.

[21] F. Kaether, W. Hampel, G. Heusser, J. Kiko, and T. Kirsten, *Reanalysis of the gallex solar neutrino flux and source experiments,* Physics Letters B **685** (2010), no. 1, 47 – 54.

[22] Super-Kamiokande, Y. Fukuda et al., *Measurement of the solar neutrino energy spectrum using neutrino electron scattering,* Phys. Rev. Lett. **82** (1999) 2430–2434, [hep-ex/9812011].

[23] J. N. Bahcall, *Solar Neutrinos: An Overview.* Springer US, Boston, MA, kursunoglu, behram n. and mintz, stephan l. and perlmutter, arnold ed., 2002.

[24] B. Pontecorvo, *Mesonium and anti-mesonium,* Sov. Phys. JETP **6** (1957) 429. [Zh. Eksp. Teor. Fiz.33,549(1957)].

[25] B. Pontecorvo, *Inverse beta processes and nonconservation of lepton charge,* Sov. Phys. JETP **7** (1958) 172–173. [Zh. Eksp. Teor. Fiz.34,247(1957)].

[26] Z. Maki, M. Nakagawa, and S. Sakata, *Remarks on the unified model of elementary particles,* Progress of Theoretical Physics **28** (1962), no. 5, 870–880.

[27] L. Wolfenstein, *Neutrino oscillations in matter,* Physical Review D **17** (1978), no. 9, 2369.

[28] S. P. Mikheev and A. Y. Smirnov, *Neutrino oscillations in a medium with variable density,* Soviet Physics Uspekhi **29** (1986), no. 12, 1155.

[29] Super-Kamiokande, Y. Fukuda et al., *Evidence for oscillation of atmospheric neutrinos,* Phys. Rev. Lett. **81** (1998) 1562–1567, [hep-ex/9807003].

[30] SNO, Q. R. Ahmad et al., *Measurement of the rate of $\nu_e + d \to p + p + e^-$ interactions produced by ^8B solar neutrinos at the Sudbury Neutrino Observatory,* Phys. Rev. Lett. **87** (2001) 071301, [nucl-ex/0106015].

[31] KamLAND, T. Araki et al., *Measurement of neutrino oscillation with KamLAND: Evidence of spectral distortion,* Phys. Rev. Lett. **94** (2005) 081801, [hep-ex/0406035].

[32] I. Gil-Botella, *Neutrino Physics*, in *Proceedings, 6th CERN - Latin-American School of High-Energy Physics (CLASHEP 2011): Natal, Brazil , March 23 - April 5, 2011*, pp. 157–205, 2013, arXiv:1504.0355.

[33] G. Barenboim, *Neutrinos: Fast & Curious*, in *2016 European School of High-Energy Physics (ESHEP 2016) Skeikampen, Norway, June 15-28, 2016*, 2016, arXiv:1610.0983.

[34] I. Esteban, M. C. Gonzalez-Garcia, M. Maltoni, I. Martinez-Soler, and T. Schwetz, *Updated fit to three neutrino mixing: exploring the accelerator-reactor complementarity,* JHEP **01** (2017) 087, [arXiv:1611.0151].

[35] C. Sutton, *Spaceship Neutrino.* Cambridge University Press, 1992.

[36] P. Hernandez, *Neutrino physics*, in *High-energy physics. Proceedings, 5th CERN-Latin-American School, Recinto Quirama, Colombia, March 15-28, 2009*, 2010, arXiv:1010.4131.

[37] Particle Data Group, C. Patrignani et al., *Review of Particle Physics,* Chin. Phys. **C40** (2016), no. 10, 100001.

[38] M. E. Peskin, D. V. Schroeder, and E. Martinec, *An introduction to quantum field theory.* AIP, 1996.

[39] C. S. Wu, E. Ambler, R. W. Hayward, D. D. Hoppes, and R. P. Hudson, *Experimental test of parity conservation in beta decay,* Phys. Rev. **105** (Feb, 1957) 1413–1415.

[40] M. Goldhaber, L. Grodzins, and A. W. Sunyar, *Helicity of Neutrinos,* Phys. Rev. **109** (1958) 1015–1017.

[41] S. M. Bilenky and C. Giunti, *Neutrinoless Double-Beta Decay: a Probe of Physics Beyond the Standard Model,* Int. J. Mod. Phys. **A30** (2015), no. 04n05, 1530001, [arXiv:1411.4791].

[42] E. Majorana, *Theory of the Symmetry of Electrons and Positrons,* Nuovo Cim. **14** (1937) 171–184.

[43] P. Hernandez, *Neutrino physics,* CERN Yellow Reports **5** (2016) 85.

[44] P. Minkowski, $\mu \to e\gamma$ *at a rate of one out of 109 muon decays?,* Physics Letters B **67** (1977), no. 4, 421 – 428.

[45] T. Yanagida, *Horizontal Symmetry and Masses of Neutrinos,* Prog.Theor.Phys. **64** (1980) 1103.

[46] M. Gell-Mann, P. Ramond, and R. Slansky, *Complex Spinors and Unified Theories,* Conf.Proc. **C790927** (1979) 315–321, [arXiv:1306.4669].

[47] R. Mohapatra and G. Senjanović, *Neutrino mass and spontaneous parity nonconservation,* Phys. Rev. Lett. **44** (Apr, 1980) 912–915.

[48] G. F. Knoll, *Radiation detection and measurement; 4th ed.* Wiley, New York, NY, 2010.

[49] C. Weinheimer, B. Degenddag, A. Bleile, J. Bonn, L. Bornschein, O. Kazachenko, A. Kovalik, and E. W. Otten, *High precision measurement of the tritium β spectrum near its endpoint and upper limit on the neutrino mass,* Phys. Lett. **B460** (1999) 219–226. [Erratum: Phys. Lett.B464,352(1999)].

[50] K. Assamagan et al., *Upper limit of the muon-neutrino mass and charged pion mass from momentum analysis of a surface muon beam,* Phys. Rev. **D53** (1996) 6065–6077.

[51] ALEPH, R. Barate et al., *An Upper limit on the tau-neutrino mass from three-prong and five-prong tau decays,* Eur. Phys. J. **C2** (1998) 395–406.

[52] KATRIN, J. Angrik et al., *KATRIN design report 2004,* 2005.

[53] Planck, P. A. R. Ade et al., *Planck 2013 results. I. Overview of products and scientific results,* Astron. Astrophys. **571** (2014) A1, [arXiv:1303.5062].

[54] A. Yu. Smirnov, *Neutrino 2012: Outlook - theory,* 2012, arXiv:1210.4061. [Nucl. Phys. Proc. Suppl.235-236,431(2013)].

[55] N. Song, R. Boyero Garcia, J. J. Gomez-Cadenas, M. C. Gonzalez-Garcia, A. Peralta Conde, and J. Taron, *Conditions for Statistical Determination of the Neutrino Mass Spectrum in Radiative Emission of Neutrino Pairs in Atoms,* Phys. Rev. **D93** (2016), no. 1, 013020, [arXiv:1510.0042].

[56] M. Goeppert-Mayer, *Double beta-disintegration,* Phys. Rev. **48** (1935) 512–516.

[57] J. J. Gómez-Cadenas, J. Martín-Albo, M. Mezzetto, F. Monrabal, and M. Sorel, *The search for neutrinoless double beta decay,* Riv. Nuovo Cim. **35** (2012) 29–98, [arXiv:1109.5515].

[58] G. B. Gelmini and M. Roncadelli, *Left-Handed Neutrino Mass Scale and Spontaneously Broken Lepton Number,* Phys. Lett. **99B** (1981) 411–415.

[59] J. Schechter and J. W. F. Valle, *Neutrino Decay and Spontaneous Violation of Lepton Number,* Phys. Rev. **D25** (1982) 774.

[60] Y. Chikashige, R. N. Mohapatra, and R. D. Peccei, *Are There Real Goldstone Bosons Associated with Broken Lepton Number?,* Phys. Lett. **B98** (1981) 265–268.

[61] EXO-200, J. B. Albert et al., *Search for Majoron-emitting modes of double-beta decay of ^{136}Xe with EXO-200,* Phys. Rev. **D90** (2014), no. 9, 092004, [arXiv:1409.6829].

[62] KamLAND-Zen, A. Gando et al., *Limits on Majoron-emitting double-beta decays of Xe-136 in the KamLAND-Zen experiment,* Phys. Rev. **C86** (2012) 021601, [arXiv:1205.6372].

[63] NEMO, R. Arnold et al., *Limits on different Majoron decay modes of Mo-100 and Se-82 for neutrinoless double beta decays in the NEMO-3 experiment,* Nucl. Phys. **A765** (2006) 483–494, [hep-ex/0601021].

[64] S. Hemmer, *Double-beta decay with majoron emission in GERDA Phase I,* Eur. Phys. J. Plus **130** (2015), no. 7, 139.

[65] R. Arnold et al., *Search for neutrinoless quadruple-β decay of ^{150}Nd with the NEMO-3 detector,* 2017, arXiv:1705.0884.

[66] J. Schechter and J. W. F. Valle, *Neutrinoless double-beta decay in SU(2)$\times$U(1) theories,* Phys. Rev. **D25** (1982) 2951.

[67] NEMO-3, R. Arnold et al., *Measurement of the double-beta decay half-life and search for the neutrinoless double-beta decay of ^{48}Ca with the NEMO-3 detector,* Phys. Rev. **D93** (2016), no. 11, 112008, [arXiv:1604.0171].

[68] CUORE, C. Alduino et al., *Measurement of the two-neutrino double-beta decay half-life of^{130} Te with the CUORE-0 experiment,* Eur. Phys. J. **C77** (2017), no. 1, 13, [arXiv:1609.0166].

[69] EXO-200, J. B. Albert et al., *Improved measurement of the $2\nu\beta\beta$ half-life of ^{136}Xe with the EXO-200 detector,* Phys. Rev. **C89** (2014), no. 1, 015502, [arXiv:1306.6106].

[70] C. Giunti and C. W. Kim, *Fundamentals of Neutrino Physics and Astrophysics.* OXFORD University Press, 2007.

[71] O. A. Ponkratenko, V. I. Tretyak, and Yu. G. Zdesenko, *The Event generator DECAY4 for simulation of double beta processes and decay of radioactive nuclei,* Phys. Atom. Nucl. **63** (2000) 1282–1287, [nucl-ex/0104018]. [Yad. Fiz.63,1355(2000)].

[72] K. Hall, *In-situ laser tagging of barium ions in liquid xenon for the EXO experiment.* PhD thesis, Colorado State University, 2012.

[73] B. Mong et al., *Spectroscopy of Ba and Ba^+ deposits in solid xenon for barium tagging in nEXO,* Phys. Rev. **A91** (2015), no. 2, 022505, [arXiv:1410.2624].

[74] B. J. P. Jones, A. D. McDonald, and D. R. Nygren, *Single Molecule Fluorescence Imaging as a Technique for Barium*

Tagging in Neutrinoless Double Beta Decay, JINST **11** (2016), no. 12, P12011, [arXiv:1609.0401].

[75] R. Luscher et al., *Search for beta beta decay in xe-136: New results from the gotthard experiment,* Phys. Lett. **B434** (1998) 407.

[76] NEMO, R. Arnold et al., *First results of the search of neutrinoless double beta decay with the NEMO 3 detector,* Phys. Rev. Lett. **95** (2005) 182302, [hep-ex/0507083].

[77] NEXT, P. Ferrario et al., *First proof of topological signature in the high pressure xenon gas TPC with electroluminescence amplification for the NEXT experiment,* JHEP **01** (2016) 104, [arXiv:1507.0590].

[78] N. Abgrall et al., *The Majorana Demonstrator radioassay program,* Nucl. Instrum. Meth. **A828** (2016) 22–36, [arXiv:1601.0377].

[79] CUORE, K. Alfonso et al., *Search for Neutrinoless Double-Beta Decay of ^{130}Te with CUORE-0,* Phys. Rev. Lett. **115** (2015), no. 10, 102502, [arXiv:1504.0245].

[80] J. Ouellet, *The Coldest Cubic Meter in the Known Universe,* 2014, arXiv:1410.1560.

[81] AMoRE, V. Alenkov et al., *Technical Design Report for the AMoRE $0\nu\beta\beta$ Decay Search Experiment,* 2015, arXiv:1512.0595.

[82] T. Bekker, N. Coron, F. Danevich, V. Degoda, A. Giuliani, V. Grigorieva, N. Ivannikova, M. Mancuso, P. de Marcillac, I. Moroz, C. Nones, E. Olivieri, G. Pessina, D. Poda, V. Shlegel, V. Tretyak, and M. Velazquez, *Aboveground test of an advanced li2moo4 scintillating bolometer to search for neutrinoless double beta decay of 100mo,* Astroparticle Physics **72** (2016) 38 – 45.

[83] M. Nebot-Guinot, M. Kaczmarski, and L. Pattavina, *Hands on LUCIFER: from assembly, operation and characterization of*

bolometric detectors, to calibration and definition of the power discrimination, PoS **GSSI14** (2015) 013.

[84] N. Casali, D. Artusa, F. Bellini, M. Biassoni, C. Brofferio, C. Bucci, A. Camacho, S. Capelli, L. Cardani, P. Carniti, L. Cassina, M. Clemenza, O. Cremonesi, A. Cruciani, A. D'Addabbo, I. Dafinei, S. D. Domizio, M. di Vacri, F. Ferroni, L. Gironi, C. Gotti, G. Keppel, M. Maino, M. Martinez, S. Morganti, S. Nagorny, D. Orlandi, L. Pagnanini, M. Pallavicini, V. Palmieri, L. Pattavina, M. Pavan, G. Pessina, V. Pettinacci, S. Pozzi, S. Pirro, E. Previtali, A. Puiu, C. Rusconi, K. Schäffner, C. Tomei, and M. Vignati, *Scintillating bolometric technique for the neutrino-less double beta decay search: The lucifer/cupid-0 experiment,* Nuclear Instruments and Methods in Physics Research Section A: Accelerators, Spectrometers, Detectors and Associated Equipment **845** (2017) 342 – 346. Proceedings of the Vienna Conference on Instrumentation 2016.

[85] KamLAND-Zen, A. Gando et al., *Limit on Neutrinoless $\beta\beta$ Decay of ^{136}Xe from the First Phase of KamLAND-Zen and Comparison with the Positive Claim in ^{76}Ge,* Phys. Rev. Lett. **110** (2013), no. 6, 062502, [arXiv:1211.3863].

[86] KamLAND-Zen, A. Gando et al., *Search for Majorana Neutrinos near the Inverted Mass Hierarchy Region with KamLAND-Zen,* Phys. Rev. Lett. **117** (2016), no. 8, 082503, [arXiv:1605.0288]. [Addendum: Phys. Rev. Lett.117,no.10,109903(2016)].

[87] SNO+, S. Andringa et al., *Current Status and Future Prospects of the SNO+ Experiment,* Adv. High Energy Phys. **2016** (2016) 6194250, [arXiv:1508.0575].

[88] T. Iida et al., *Status and future prospect of ^{48}Ca double beta decay search in CANDLES,* J. Phys. Conf. Ser. **718** (2016), no. 6, 062026.

[89] GERDA, M. Agostini et al., *Results on Neutrinoless Double-β Decay of ^{76}Ge from Phase I of the GERDA Experiment,* Phys. Rev. Lett. **111** (2013), no. 12, 122503, [arXiv:1307.4720].

[90] Majorana, N. Abgrall et al., *The Majorana Demonstrator Neutrinoless Double-Beta Decay Experiment,* Adv. High Energy Phys. **2014** (2014) 365432, [arXiv:1308.1633].

[91] *The majorana neutrinoless double-beta decay experiment.* https://www.npl.washington.edu/majorana/.

[92] J. Ebert et al., *Current Status and Future Perspectives of the COBRA Experiment,* Adv. High Energy Phys. **2013** (2013) 703572.

[93] C. Oldorf, *Operation of CdZnTe Semiconductor Detectors in Liquid Scintillator for the COBRA Experiment.* Dr., Universität Hamburg, 2015. Universität Hamburg, Diss., 2015.

[94] J. Ebert, M. Fritts, D. Gehre, C. Gößling, T. Göpfert, C. Hagner, N. Heidrich, R. Klingenberg, T. Köttig, K. Kröninger, T. Michel, T. Neddermann, C. Nitsch, C. Oldorf, T. Quante, S. Rajek, H. Rebber, O. Reinecke, K. Rohatsch, O. Schulz, A. Sörensen, I. Stekl, J. Tebrügge, R. Temminghoff, R. Theinert, J. Timm, T. Wester, B. Wonsak, S. Zatschler, and K. Zuber, *The {COBRA} demonstrator at the {LNGS} underground laboratory,* Nuclear Instruments and Methods in Physics Research Section A: Accelerators, Spectrometers, Detectors and Associated Equipment **807** (2016) 114 – 120.

[95] SuperNEMO, P. P. Povinec, *Background constrains of the SuperNEMO experiment for neutrinoless double beta-decay searches,* Nucl. Instrum. Meth. **A845** (2017) 398–403.

[96] EXO-200, N. Ackerman et al., *Observation of Two-Neutrino Double-Beta Decay in ^{136}Xe with EXO-200,* Phys. Rev. Lett. **107** (2011) 212501, [arXiv:1108.4193].

[97] EXO-200, J. B. Albert et al., *Search for Majorana neutrinos with the first two years of EXO-200 data,* Nature **510** (2014) 229–234, [arXiv:1402.6956].

[98] EXO-200, : et al., *Searches for Double Beta Decay of ^{134}Xe with EXO-200,* 2017, arXiv:1704.0504.

[99] C. Monteiro et al., *Secondary scintillation yield in pure xenon,* JINST **2** (2007) P05001.

[100] L. M. P. Fernandes et al., *Primary and secondary scintillation measurements in a xenon Gas Proportional Scintillation Counter,* JINST **5** (2010) P09006, [arXiv:1009.2719].

[101] A. Bolotnikov and B. Ramsey, *The spectroscopic properties of high-pressure xenon,* Nucl. Instrum. Meth. **A396** (1997) 360.

[102] A. S. Barabash, *Brief review of double beta decay experiments*, in *Proceedings, 2nd International Conference on Particle Physics and Astrophysics (ICPPA 2016): Moscow, Russia, October 10-14, 2016*, 2017, arXiv:1702.6340.

[103] NEXT, F. Granena et al., *NEXT, a HPGXe TPC for neutrinoless double beta decay searches,* 2009, arXiv:0907.4054.

[104] D. Nygren, *High-pressure xenon gas electroluminescent TPC for $0\nu\beta\beta$ decay search,* Nucl. Instrum. Meth. A **603** (2009) 337–348.

[105] E. D. C. Freitas et al., *Secondary scintillation yield in high-pressure xenon gas for neutrinoless double beta decay (0nu beta beta) search,* Phys. Lett. **B684** (2010) 205–210.

[106] NEXT, V. Alvarez et al., *Near-Intrinsic Energy Resolution for 30 to 662 keV Gamma Rays in a High Pressure Xenon Electroluminescent TPC,* Nucl.Instrum.Meth. **A708** (2013) 101–114, [arXiv:1211.4474].

[107] C. Oliveira et al., *Energy resolution studies for next,* JINST **6** (2011) P05007.

[108] NEXT, V. Alvarez et al., *The NEXT-100 experiment for neutrinoless double beta decay searches (Conceptual Design Report),* 2011, arXiv:1106.3630.

[109] V. Alvarez, I. Bandac, A. Bettini, F. Borges, S. Carcel, et al., *Radiopurity control in the NEXT-100 double beta decay experiment: procedures and initial measurements,* JINST **8** (2013) T01002, [arXiv:1211.3961].

[110] NEXT, J. Martín-Albo et al., *Sensitivity of NEXT-100 to neutrinoless double beta decay,* JHEP **05** (2016) 159, [arXiv:1511.0924].

[111] NEXT, V. Alvarez et al., *Ionization and scintillation response of high-pressure xenon gas to alpha particles,* JINST **8** (2013) P05025, [arXiv:1211.4508].

[112] E. Aprile, A. I. Bolotnikov, A. I. Bolozdynya, and T. Doke, *Noble gas detectors.* Wiley-VCN, 2006.

[113] D. R. Nygren, *The Time Projection Chamber: A New 4 pi Detector for Charged Particles,* eConf **C740805** (1974) 58.

[114] NEXT, V. Álvarez et al., *NEXT-100 Technical Design Report (TDR): Executive Summary,* JINST **7** (2012) T06001, [arXiv:1202.0721].

[115] NEXT Collaboration, V. Álvarez, M. Ball, F. I. G. M. Borges, S. Cárcel, J. M. Carmona, J. Castel, J. M. Catalá, S. Cebrián, A. Cervera, D. Chan, C. A. N. Conde, T. Dafni, T. H. V. T. Dias, J. Díaz, M. Egorov, R. Esteve, P. Evtoukhovitch, L. M. P. Fernandes, P. Ferrario, A. L. Ferreira, E. Ferrer-Ribas, E. D. C. Freitas, A. N. C. Garcia, V. M. Gehman, A. Gil, I. Giomataris, A. Goldschmidt, H. Gómez, J. J. Gómez-Cadenas, K. González, D. González-Díaz, R. M. Gutiérrez, J. Hauptman, J. A. Hernando Morata, D. C. Herrera, V. Herrero, F. J. Iguaz, I. G. Irastorza, V. Kalinnikov, D. Kiang, L. Labarga, I. Liubarsky, J. A. M. Lopes, D. Lorca, M. Losada, G. Luzón, A. Marí, J. Martín-Albo, A. Martínez, T. Miller, A. Moiseenko, F. Monrabal, C. M. B. Monteiro, J. M. Monzó, F. J. Mora, L. M. Moutinho, J. Muñoz Vidal, H. Natal da Luz, G. Navarro, M. Nebot, D. Nygren, C. A. B. Oliveira, R. Palma, J. Pérez, J. L. Pérez Aparicio, J. Renner, L. Ripoll, A. Rodríguez, J. Rodríguez, F. P. Santos, J. M. F. dos Santos, L. Segui, L. Serra, D. Shuman, C. Sofka, M. Sorel, J. F. Toledo, A. Tomás, J. Torrent, Z. Tsamalaidze, D. Vázquez, E. Velicheva, J. F. C. A. Veloso, J. A. Villar, R. C. Webb, T. Weber, J. White, and N. Yahlali, *Design and characterization of the SiPM tracking system of*

NEXT-DEMO, a demonstrator prototype of the NEXT-100 experiment, ArXiv e-prints (June, 2012) [arXiv:1206.6199].

[116] NEXT, V. Álvarez et al., *Operation and first results of the NEXT-DEMO prototype using a silicon photomultiplier tracking array,* JINST **8** (2013) P09011, [arXiv:1306.0471].

[117] NEXT, V. Alvarez et al., *Initial results of NEXT-DEMO, a large-scale prototype of the NEXT-100 experiment,* JINST **8** (2013) P04002, [arXiv:1211.4838].

[118] NEXT, J. Renner et al., *Background rejection in NEXT using deep neural networks,* JINST **12** (2017), no. 01, T01004, [arXiv:1609.0620].

[119] NEXT, A. Simón et al., *Application and performance of an ML-EM algorithm in NEXT,* 2017, arXiv:1705.1027.

[120] K. Lung, K. Arisaka, A. Bargetzi, P. Beltrame, A. Cahill, et al., *Characterization of the Hamamatsu R11410-10 3-Inch Photomultiplier Tube for Liquid Xenon Dark Matter Direct Detection Experiments,* Nucl. Instrum. Meth. **A696** (2012) 32–39, [arXiv:1202.2628].

[121] F. Simpson, R. Jimenez, C. Pena-Garay, and L. Verde, *Strong Evidence for the Normal Neutrino Hierarchy,* 2017, arXiv:1703.0342.

[122] *Hamamatsu webpage.* http://www.hamamatsu.com/eu/en/index.html.

[123] NEXT, D. Lorca et al., *Characterisation of NEXT-DEMO using xenon K_α X-rays,* JINST **9** (2014), no. 10, P10007, [arXiv:1407.3966].

[124] D. Lorca Galindo, *SiPM based tracking for detector calibration in NEXT.* PhD thesis, Valencia U., IFIC, 2015.

[125] *SensL MicroFC- 10035-SMT-GP.* http://bit.ly/1tn1yjh.

[126] J. Rodríguez, M. Querol, J. Díaz, J. Gómez-Cadenas, D. Lorca, V. Álvarez, A. Martínez, and A. Gil, *Mass production automated test system for the next sipm tracking plane*, in *2012 IEEE Nuclear Science Symposium and Medical Imaging Conference Record (NSS/MIC)*, pp. 1106–1108, Oct, 2012.

[127] J. Rodríguez, J. Toledo, R. Esteve, D. Lorca, and F. Monrabal, *The front-end electronics for the 1.8-kchannel SiPM tracking plane in the NEW detector,* JINST **10** (2015), no. 01, C01025.

[128] NEXT, S. Cebrián et al., *Radiopurity assessment of the tracking readout for the NEXT double beta decay experiment,* JINST **10** (2015), no. 05, P05006, [arXiv:1411.1433].

[129] M. Querol, J. Rodríguez, J. Toledo, R. Esteve, V. Álvarez, and V. Herrero, *A programmable, multichannel power supply for SIPMs with temperature compensation loop and Ethernet interface,* JINST **11** (2016), no. 12, C12035.

[130] S. Martoiu, H. Muller, A. Tarazona, and J. Toledo, *Development of the scalable readout system for micro-pattern gas detectors and other applications,* Journal of Instrumentation **8** (2013), no. 03, C03015.

[131] RD51 Collaboration, M. Chefdeville, *RD51, a world-wide collaboration for the development of micro pattern gaseous detectors,* J. Phys. Conf. Ser. **309** (2011) 012017.

[132] J. Toledo, H. Muller, R. Esteve, J. Monzo, A. Tarazona, et al., *The Front-End Concentrator card for the RD51 Scalable Readout System,* JINST **6** (2011) C11028.

[133] R. Esteve, J. Toledo, J. Rodríguez, M. Querol, and V. Álvarez, *Readout and data acquisition in the next-new detector based on srs-atca,* Journal of Instrumentation **11** (2016), no. 01, C01008.

[134] R. Esteve, J. Toledo, F. Monrabal, D. Lorca, L. Serra, A. Marí, J. J. Gómez-Cadenas, I. Liubarsky, and F. Mora, *The trigger system in the next-demo detector,* Journal of Instrumentation **7** (2012), no. 12, C12001.

[135] *SERA GmbH.* `http://www.sera-web.com`.

[136] NEXT, L. Serra et al., *An improved measurement of electron-ion recombination in high-pressure xenon gas,* JINST **10** (2015), no. 03, P03025, [`arXiv:1412.3573`].

[137] A.Ianni, *Canfranc underground laboratory.* Private communication from workshop, 2016.

[138] OPERA, M. Guler et al., *OPERA: An appearance experiment to search for nu/mu ¡–¿ nu/tau oscillations in the CNGS beam. Experimental proposal,* 2000.

[139] S. Agostinelli et al., *Geant4: A simulation toolkit,* Nucl. Instrum. Meth. **A506** (2003) 250.

[140] J. Martín-Albo, *The NEXT experiment for neutrinoless double beta decay searches.* PhD thesis, Valencia U., IFIC, 2015.

[141] R. Brun and F. Rademakers, *Root — an object oriented data analysis framework,* Nuclear Instruments and Methods in Physics Research Section A: Accelerators, Spectrometers, Detectors and Associated Equipment **389** (1997), no. 1, 81 – 86. https://root.cern.ch.

[142] D. Jordan et al., *Measurement of the neutron background at the Canfranc Underground Laboratory LSC,* Astropart. Phys. **42** (2013) 1–6.

[143] *LSC Radiopurity Service.* `http://www.lsc-canfranc.es/en/for-users/lsc-services/radiopurity.html`.

[144] S. Cebrián, J. Pérez, I. Bandac, L. Labarga, V. Álvarez, C. Azevedo, J. Benlloch-Rodríguez, F. Borges, A. Botas, S. Cárcel, J. Carrión, C. Conde, J. Díaz, M. Diesburg, J. Escada, R. Esteve, R. Felkai, L. Fernandes, P. Ferrario, A. Ferreira, E. Freitas, A. Goldschmidt, J. Gómez-Cadenas, D. González-Díaz, R. Gutiérrez, J. Hauptman, C. Henriques, A. Hernandez, J. H. Morata, V. Herrero, B. Jones, A. Laing, P. Lebrun, I. Liubarsky, N. López-March, M. Losada,

J. Martín-Albo, G. Martínez-Lema, A. Martínez, A. McDonald, F. Monrabal, C. Monteiro, F. Mora, L. Moutinho, J. M. Vidal, M. Musti, M. Nebot-Guinot, P. Novella, D. Nygren, B. Palmeiro, A. Para, M. Querol, J. Renner, L. Ripoll, J. Rodríguez, L. Rogers, F. Santos, J. dos Santos, A. Simón, C. Sofka, M. Sorel, T. Stiegler, J. Toledo, J. Torrent, Z. Tsamalaidze, J. Veloso, J. Villar, R. Webb, J. White, and N. Yahlali, *Radiopurity assessment of the energy readout for the next double beta decay experiment,* Journal of Instrumentation **12** (2017), no. 08, T08003.

[145] E. Aprile et al., *Material screening and selection for XENON100,* Astropart. Phys. **35** (2011) 43–49, [arXiv:1103.5831].

[146] D. S. Akerib et al., *An Ultra-Low Background PMT for Liquid Xenon Detectors,* Nucl. Instrum. Meth. **A703** (2013) 1–6, [arXiv:1205.2272].

[147] PandaX, X. Cao et al., *PandaX: A Liquid Xenon Dark Matter Experiment at CJPL,* Sci. China Phys. Mech. Astron. **57** (2014) 1476–1494, [arXiv:1405.2882].

[148] V. Álvarez et al., *Radiopurity control in the NEXT-100 double beta decay experiment,* AIP Conf. Proc. **1549** (2013) 46–49.

[149] NEXT, T. Dafni et al., *Results of the material screening program of the NEXT experiment,* Nucl. Part. Phys. Proc. **273-275** (2016) 2666–2668, [arXiv:1411.1222].

[150] S. Cebrián et al., *Radon and material radiopurity assessment for the NEXT double beta decay experiment,* AIP Conf. Proc. **1672** (2015) 060002, [arXiv:1505.0705].

[151] National Nuclear Data Center, *NuDat 2 database.* Available online at http://www.nndc.bnl.gov/nudat2/.

[152] Wikipedia, *Natural decay chain — wikipedia, the free encyclopedia.* https://en.wikipedia.org/wiki/Decay_chain.

[153] D. S. Leonard et al., *Systematic study of trace radioactive impurities in candidate construction materials for EXO-200,*

Nucl. Instrum. Meth. **A591** (2008) 490–509, [arXiv:0709.4524].

[154] I. Bandac, S. Borjabad, A. Ianni, R. Nuñez-Lagos, C. Pérez, S. Rodríguez, and J. Villar, *Ultra-low background and environmental measurements at laboratorio subterráneo de canfranc (lsc),* Applied Radiation and Isotopes **126** (2017) 127 – 129. Proceedings of the 7th International Conference on Radionuclide Metrology – Low-Level Radioactivity Measurement Techniques.

[155] EXO-200, J. B. Albert et al., *Cosmogenic Backgrounds to $0\nu\beta\beta$ in EXO-200,* JCAP **1604** (2016), no. 04, 029, [arXiv:1512.0683].

[156] XENON100, E. Aprile et al., *Online^{222} Rn removal by cryogenic distillation in the XENON100 experiment,* Eur. Phys. J. **C77** (2017), no. 6, 358, [arXiv:1702.0694].

[157] A. C. Ezeribe, W. Lynch, R. R. M. G. J. Mckeand, A. Scarff, and N. J. C. Spooner, *Demonstration of radon removal from SF_6 using molecular sieves for dark matter searches,* 2017, arXiv:1707.0777.

[158] M. Nebot-Guinot et al., *Shielding struct lead castle radiopurity impact.* Internal report.

[159] M. Auger et al., *A Novel Cosmic Ray Tagger System for Liquid Argon TPC Neutrino Detectors,* 2016, arXiv:1612.0461.

[160] M. Sorel et al., *The NEXT experiment for $\beta\beta0\nu$ searches at LSC. Background Model.* . A status report: April 2016.

[161] NEXT, V. Alvarez et al., *In-situ calibration of a PMT inside a scintillation detector by means of primary scintillation detection,* 2012, arXiv:1211.4409.

[162] L. W. Kastens, S. B. Cahn, A. Manzur, and D. N. McKinsey, *Calibration of a Liquid Xenon Detector with Kr-83m,* Phys. Rev. **C80** (2009) 045809, [arXiv:0905.1766].

[163] *The art event processing framework.* `http://art.fnal.gov`.

[164] F. Carena, W. Carena, S. Chapeland, V. C. Barroso, F. Costa, E. Dénes, R. Divià, U. Fuchs, A. Grigore, T. Kiss, G. Simonetti, C. Soós, A. Telesca, P. V. Vyvre, and B. von Haller, *The alice data acquisition system,* Nuclear Instruments and Methods in Physics Research Section A: Accelerators, Spectrometers, Detectors and Associated Equipment **741** (2014) 130 – 162.

[165] M. Nebot-Guinot, *Development of wavelength shifter coated reflectors for the next experiment*, Master's thesis, Valencia U., IFIC, Dec. 2011.

[166] C. A. B. de Oliveira, *Monte Carlo studies of electroluminiscence in gaseous detectors.* PhD thesis, Universidade de Aveiro, 2011.

[167] V. Gehman, S. Seibert, K. Rielage, A. Hime, Y. Sun, et al., *Fluorescence Efficiency and Visible Re-emission Spectrum of Tetraphenyl Butadiene Films at Extreme Ultraviolet Wavelengths,* Nucl. Instrum. Meth. **A654** (2011) 116–121, [`arXiv:1104.3259`].

[168] R. Jerry, L. Winslow, L. Bugel, and J. M. Conrad, *A Study of the Fluorescence Response of Tetraphenyl-butadiene,* ArXiv e-prints (Jan., 2010) [`arXiv:1001.4214`].

[169] The ArDM, V. Boccone et al., *Development of wavelength shifter coated reflectors for the ArDM argon dark matter detector,* JINST **4** (2009) P06001, [`arXiv:0904.0246`].

[170] N. Yahlali, J. Garcia, J. Díaz, A. Soriano, and L. Fernandes, *Ageing studies of tpb in noble gas detectors for dark matter and neutrinoless decay searches,* Spectrochimica Acta Part A: Molecular and Biomolecular Spectroscopy **172** (2017) 109 – 114. Special Issue: Colloquium Spectroscopicum Internationale XXXIX.

[171] V. Álvarez, J. Agramunt, M. Ball, M. Batallé, J. Bayarri, F. I. G. Borges, H. Bolink, H. Brine, S. Cárcel, J. M. Carmona, J. Castel, J. M. Catalá, S. Cebrián, A. Cervera, D. Chan, C. A. N. Conde,

T. Dafni, T. H. V. T. Dias, J. Díaz, R. Esteve, P. Evtoukhovitch, J. Ferrando, L. M. P. Fernandes, P. Ferrario, A. L. Ferreira, E. Ferrer-Ribas, E. D. C. Freitas, S. A. García, A. Gil, I. Giomataris, A. Goldschmidt, E. Gómez, H. Gómez, J. J. Gómez-Cadenas, K. González, R. M. Gutiérrez, J. Hauptman, J. A. Hernando-Morata, D. C. Herrera, V. Herrero, F. J. Iguaz, I. G. Irastorza, V. Kalinnikov, L. Labarga, I. Liubarsky, J. A. M. Lopes, D. Lorca, M. Losada, G. Luzón, A. Marí, J. Martin-Albo, A. M. Méndez, T. Miller, A. Moisenko, F. Monrabal, C. M. B. Monteiro, J. M. Monzó, F. J. Mora, J. Muñoz Vidal, H. Natal da Luz, G. Navarro, M. Nebot, D. Nygren, C. A. B. Oliveira, R. Palma, J. L. Pérez Aparicio, J. Pérez, E. Radicioni, M. Quinto, J. Renner, L. Ripoll, A. Rodriguez, J. Rodriguez, F. P. Santos, J. M. F. dos Santos, L. Seguí, L. Serra, D. Shuman, C. Sofka, M. Sorel, A. Soriano, H. Spieler, J. F. Toledo, J. Torrent Collell, A. Tomás, Z. Tsamalaidze, D. Vázquez, E. Velicheva, J. F. C. A. Veloso, J. A. Villar, R. Webb, T. Weber, J. T. White, and N. Yahlali, *SiPMs coated with TPB: coating protocol and characterization for NEXT,* Journal of Instrumentation **7** (Feb., 2012) 2010, [arXiv:1201.2018].

Out of the night that covers me,
Black as the pit from pole to pole,
I thank whatever gods may be
For my unconquerable soul.
In the fell clutch of circumstance
I have not winced nor cried aloud.
Under the bludgeonings of chance
My head is bloody, but unbowed.
Beyond this place of wrath and tears
Looms but the horror of the shade,
And yet the menace of the years
Finds and shall find me unafraid.
It matters not how strait the gate,
How charged with punishments the scroll,
I am the master of my fate:
I am the captain of my soul.

Invictus, William Ernest Henley